Molecular imaging of tumor characteristics to support targeted cancer therapies

Scheltinga, Antonius Gerhardus Titus Terwisscha van

Molecular imaging of tumor characteristics to support targeted cancer therapies:

a preclinical focus on HER2, HER3, c-Met, IGF-1R and VEGF-A imaging

Anton Terwisscha van Scheltinga

Molecular imaging of tumor characteristics
to support targeted cancer therapies:

a preclinical focus on HER2, HER3, c-Met, IGF-1R and VEGF-A imaging

Anton Terwisscha van Scheltinga

Terwisscha van Scheltinga, A.G.T.

Molecular imaging of tumor characteristics to support targeted cancer therapies:

a preclinical focus on HER2, HER3, c-Met, IGF-1R and VEGF-A imaging

Thesis, University of Groningen, The Netherlands

Cover design: Regina Terwisscha van Scheltinga
Cover photo: Julia van Valen
Printed by: Ipskamp Drukkers, Enschede, The Netherlands

STELLINGEN

behorende bij het proefschrift

**Molecular imaging of tumor characteristics
to support targeted cancer therapies:**
a preclinical focus on HER2, HER3, c-Met, IGF-1R and VEGF-A imaging

1. De receptoren HER3 en c-Met kunnen afgebeeld worden met behulp van ^{89}Zr-PET beeldvorming. *(dit proefschrift)*

2. Met ^{89}Zr-bevacizumab PET kan een reductie van tumor VEGF-A spiegels worden gevisualiseerd kort na het starten van behandeling met mTOR of Hsp90 remmers. *(dit proefschrift)*

3. Met behulp van fluorescent gelabelde antilichamen gericht tegen HER2 en VEGF-A kunnen sub-millimeter grote tumorlaesies zichtbaar worden gemaakt. *(dit proefschrift)*

4. Moleculaire beeldvorming met ^{89}Zr-PET kan in het vroeg klinisch geneesmiddelen onderzoek ondersteunen bij het selecteren van de juiste dosering en bij het selecteren van aanwezigheid van de juiste moleculaire tumoreigenschap.

5. Met moleculaire beeldvorming met ^{89}Zr-PET kan de heterogeniteit tussen tumorlaesies in een patiënt in beeld gebracht worden.

6. Naast monoclonale antilichamen en tyrosine kinase remmers is er binnen de 'targeted therapies' in de oncologie nog ruimte voor een nieuwe geneesmiddelgroep die de eiwit interacties binnenin de tumorcel kunnen blokkeren, zoals de 'synthetic biologicals'. (Verdine et al. Methods in Enzymology 2012)

7. Samenwerking met de farmaceutische industrie biedt wetenschappelijk unieke mogelijkheden maar kan de wetenschappelijke vrijheid, snelheid en creativiteit beperken.

8. Aseptisch werken en 'Good Cell Culture Practice' kan uitsluitend met 2 steriele handschoenen.

9. Geen tijd hebben betekent ergens prioriteit aan geven.

10. Afzien en genieten gaan vaak samen.

11. Om innerlijke rust te vinden, moet je afmaken waaraan je begonnen bent.

12. Wielrennen met tegenwind in het Noord-Nederlandse landschap is de manier om tegenslagen in het onderzoek te verwerken.

13. Weten hoe de hazen lopen is altijd van belang.

Anton Terwisscha van Scheltinga
Groningen, 13 mei 2013
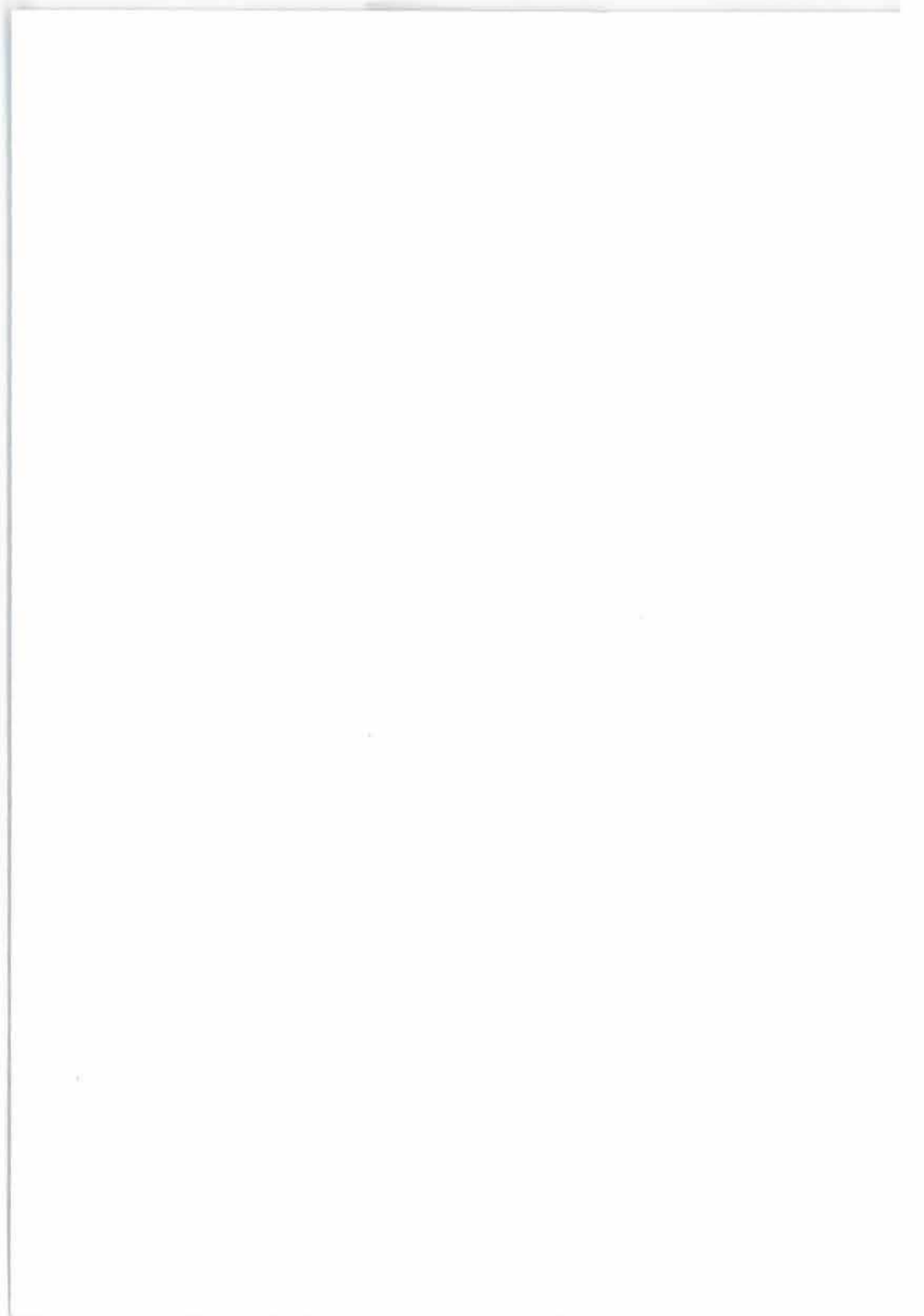
rijksuniversiteit groningen

Molecular imaging of tumor characteristics
to support targeted cancer therapies:
a preclinical focus on HER2, HER3, c-Met, IGF-1R and VEGF-A imaging

Proefschrift

ter verkrijging van het doctoraat in de
Medische Wetenschappen
aan de Rijksuniversiteit Groningen
op gezag van de
Rector Magnificus, dr. E. Sterken,
in het openbaar te verdedigen op
maandag 13 mei 2013
om 14.30 uur

door

Antonius Gerhardus Titus Terwisscha van Scheltinga

geboren op 15 januari 1985
te Leeuwarden

Promotores: Prof. dr. E.G.E. de Vries

Prof. dr. J.G.W. Kosterink

Copromotores: Dr. M.N. Lub-de Hooge

Dr. C.P. Schröder

Beoordelingscommissie: Prof. dr. O.C. Boerman

Prof. dr. P.H. Elsinga

Prof. dr. J.A. Gietema

CONTENTS

Paranimfen

Maarten van Valen

Remy Verheijen

CHAPTER 1

General introduction

BACKGROUND

Cancer is a disease in which cells have acquired the capacity to divide without control. They are able to invade other tissues and can metastasize to other parts of the body. Cancer is not one entity, but consists of several tumor types. Within each tumor type increasingly subgroups can be defined based on molecular characteristics. Therapeutic approaches consist besides local treatment by surgery and radiotherapy, of drugs administered systemically. Together these approaches form the basis of anti-cancer treatment.

Anticancer drugs consist of chemotherapeutic drugs and targeted agents. Chemotherapeutic drugs directly or indirectly aim to induce DNA damage resulting in cell cycle arrest and apoptosis. Per tumor type, different specific combinations of cytostatic agents are being combined. Unfortunately resistance against the chemotherapeutic agents often occurs, which leads to treatment failure.

Drug resistance of the tumor to several unrelated classes of natural products, including anthracyclines, taxanes and vinca alkaloids, is often referred to as multidrug resistance (MDR). (1) MDR can be caused by several mechanisms including increased expression of the ATP-binding cassette transporters (ABC-transporters) and drug efflux pumps like P-glycoprotein (P-gp) and multidrug resistance protein (MRP1). Initially it was thought that overcoming MDR, the problem of intrinsic and acquired resistance against chemotherapeutic agents could be resolved. This could however not be confirmed in randomized controlled clinical trials where P-gp inhibitors were combined with chemotherapeutic agents. (1) Based on new insights in cancer biology, targeted treatments have been developed which possibly can circumvent MDR and enhance anti-tumor effects, with or without chemotherapy.

In the past decades tumor biology research identified new molecular tumor characteristics, also defined as the hallmarks of cancer. (2) These hallmarks include among others sustaining proliferative signaling, evading growth suppressors, inducing angiogenesis and activating invasion and metastasis. Understanding of these hallmarks increasingly affect the development of new drugs. (3-4)

One of the successful targeted therapies is the current treatment for human epidermal growth factor receptor (HER) 2 positive breast cancer. The HER transmembrane receptor tyrosine kinase family consists of four members: epidermal growth factor receptor (EGFR), HER2, HER3 and HER4. Members of this family play a critical role in tumor cell survival, proliferation, maturation, metastasis and angiogenesis via diverse cellular pathways. (5) HER2 is a potent pro-oncogenic factor which is overexpressed in 20-30% of breast cancer patients. Overexpression is also seen in subgroups of gastric, ovarian and colon cancer patients. Trastuzumab, the monoclonal antibody targeting the HER2, can successfully inhibit the activation of HER2 and thereby inhibit tumor growth. (5)

Other examples of growth factor receptors that can be potentially inhibited are the tyrosine kinase receptors HER3, insulin-like growth factor receptor 1 (IGF-1R) and mesenchymal-epithelial transition factor (c-Met).

1

HER family members are inactive as monomers, but can be activated by homo- or heterodimerization after ligand binding. HER3 is the only member in the HER family lacking intrinsic tyrosine kinase activity and therefore has been underestimated for its role in cancer until recently. (5) It can only be activated after the formation of heterodimers. The most active signaling complexes, HER1/HER3 and HER2/HER3 heterodimers are the most potent dimers in this family. Increasingly the prominent role of HER3 is recognized in tumor growth and maintenance as well as the fact that it is highly expressed in many solid tumors. This makes HER3 an interesting target to inhibit HER family signaling.

The IGF-1R is a transmembrane molecule with tyrosine kinase activity which binds to its ligand IGF-1 with high affinity. IGF-1R is important for tumor growth and survival, and plays a major role in the multistep metastatic process, where it regulates migration, invasion and angiogenesis. Inhibition if this target showed in several early phase clinical trials promising results. However, initial Phase III results in unselected patients have been disappointing. (6)

c-Met is of interest as drug target as genetic and biochemical data showed that the growth and motility factor hepatocyte growth factor (HGF), also called scatter factor and its receptor, c-Met, have a causal role in essential hallmarks of cancer. c-Met overexpression at the tumor cell membrane and its ligand HGF in the surrounding stroma occurs in many tumor types. This provides a strong rationale for targeting both for antitumor effect. Currently antibodies against this receptor and ligand and tyrosine kinase inhibitors against c-Met are tested with promising results. (6-7)

Angiogenesis, the development of new blood vessels, is important in all solid tumors for the supply of nutrients and oxygen. An important factor in angiogenesis is the vascular endothelial growth factor (VEGF). It is released by tumor cells in the tumor surrounding and induces tumor neovascularization. Overexpression of VEGF occurs in many human tumor types and is therefore a rational target. (8) Over the last years, several antiangiogenic drugs have been approved for clinical use.

Besides inhibiting receptors at the tumor cell surface and soluble targets in the tumor surrounding, drugs can also affect downstream factors. One example of this is the mammalian target of rapamycin (mTOR) which controls translation of several oncogenic proteins, including several factors in angiogenesis. (9) In addition of these examples of individual targets for cancer therapy, there is an interesting target which enables to inhibit multiple oncogenic proteins simultaneously. By inhibiting the heat shock protein-90 (Hsp90) as molecular chaperone, the conformation, activation, stability and functionality of over hundred client proteins is inhibited. (10)

Many novel molecular targets for anticancer treatment have been discovered, resulting in development of numerous targeted anticancer drugs, including therapeutic antibodies. Molecular imaging using radiolabeled monoclonal antibodies can identify noninvasively the presence of specific targets against which the antibody is raised. Moreover it provides whole body information about tumor uptake and organ distribution of the

antibodies. Besides visualization of drug distribution, these radiolabeled antibodies can be used to monitor tumor status during treatment effects, thereby using the receptor or ligands as biomarker. Depending on the type of radioisotope labeled to the antibody imaging can be performed with planar scintigraphy and single photon emission computed tomography (SPECT) or positron emission tomography (PET). This approach can potentially serve in the clinic for patient selection, tumor staging, as (early) predictive biomarker for tumor response and in research for dug development. (11)

ImmunoPET is defined as the tracking and quantification of radiolabeled antibodies with PET *in vivo*. Currently a suitable radioisotope for immunoPET-imaging is available, zirconium-89 ([89]Zr). [89]Zr has been labeled to various antibodies and tested successfully preclinical and clinically. Besides nuclear imaging, also fluorescent labeled antibodies can be visualized using optical imaging approaches. Potential local measurement of drug targets will become available in the near future which can be visualized using fluorescent labeled antibodies by using newly developed optical imaging platforms such as intraoperative camera, multispectral optoacoustic tomography and fluorescent endoscopy.

The aim of this thesis is to develop and apply new tracers for molecular imaging in oncology with [89]Zr-labeled radiopharmaceuticals for PET imaging and fluorescent labeled antibodies for optical imaging.

OUTLINE OF THE THESIS

In chapter 2 an overview is presented of the possibilities to monitor MDR non-invasively in patients. Several radiopharmaceuticals and clinical studies in which these tracers have been evaluated are discussed. Combination of chemotherapeutic agents involved in MDR together with targeted therapies are becoming available for clinical use and much combinations are under investigation. The concept of molecular imaging can also be used to visualize these new agents. Therefore, we also discuss the imaging opportunities of HER2 and VEGF to illustrate the new opportunities for molecular imaging.

In chapters 3 and 4 the development of a new radiopharmaceutical is described, including the preclinical evaluation by performing PET imaging with these tracers in human tumor bearing mice.

Chapter 3 describes the development and preclinical validation of PET imaging with the [89]Zr-labeled HER3 antibody GE-huMAb-HER3. Biodistribution, dose-dependency of organ distribution and specific tumor uptake is assessed in human tumor bearing mice. MicroPET imaging is performed with [89]Zr-GE-huMAb-HER3 in different xenografts with varying HER3 expression. The imaging results are correlated with *ex vivo* biodistribution results.

Anticalins are a novel class of biopharmaceuticals, which are high affinity scaffold proteins based on human lipocalins. (12) The anticalin PRS-110 targets with high affinity the oncogene c-Met. PRS-110 is labeled

radioactively with [89]Zr. In chapter 4 the study is described where c-Met expression is visualized and the biodistribution of [89]Zr-PRS-110 in human tumor bearing mice is studied. PRS-110 is also labeled with the fluorescent dye IRDye 800CW to study the distribution within the tumor *ex vivo*.

Chapters 5 and 6 describe the application of radiolabeled antibodies to monitor tumor status during treatment effects.

Several targeted therapies are being explored for their potential to inhibit angiogenesis in ovarian cancer. mTOR controls the translation of several oncogenic proteins, including several factors involved in angiogenesis. (9) Inhibiting mTOR results in repression of translation of VEGF-A. Monitoring reductions in tumor VEGF-A expression, as an early read-out for antitumor efficacy, could potentially provide an early response prediction which could benefit patient selection. In chapter 5 we monitor tumor VEGF-A levels with PET imaging before and during treatment with the mTOR inhibitor everolimus in a human ovarian cancer xenograft mouse model. Tumor VEGF-A levels are measured before and after 2 weeks of continuous everolimus treatment using [89]Zr-bevacizumab. *In vivo* imaging results are correlated with *ex vivo* biodistribution data and VEGF-A protein levels. Immunohistochemistry is performed to assess vascular density, tumor viability and activation of downstream mTOR target protein S6.

Another drug effect that can potentially be guided by molecular imaging is Hsp90 inhibition. The Hsp90 inhibitor NVP-AUY922 downregulates the expression of many oncogenic proteins including IGF-1R and hypoxia inducible factor 1α (HIF-1α) resulting in decreased VEGF-A excretion. (10) Triple negative breast cancer is biologically characterized by heterogeneous presence of molecular pathways. (13) We therefore aimed in chapter 6 to visualize dual therapeutic effects in triple negative breast cancer that can be influenced by Hsp90 inhibition with NVP-AUY922 *in vitro* and *in vivo*, namely IGF-1R expression and VEGF-A levels. Antibodies targeting IGF-1R and VEGF-A are labeled with [89]Zr. In human breast cancer MCF-7 and MDA-MB-231 cell lines NVP-AUY922 effects on cellular IGF-1R expression and VEGF-A secretion is determined. Mice bearing human triple negative breast cancer receive NVP-AUY922 for 21 days. PET scans with [89]Zr-MAB391 and [89]Zr-bevacizumab for visualization of IGF-1R and VEGF-A are performed before and after treatment. *Ex vivo* biodistribution and correlative tissue analyses are executed.

Fluorescence imaging is currently attracting much interest as a method for intraoperative tumor detection. (14) This technique can be further improved by tumor-specific detection. In chapter 7 we applied antibody-based tumor detection to intraoperative optical imaging, using preclinical *in vivo* mouse models. Bevacizumab targeting VEGF and trastuzumab targeting HER2 are labeled with the near-infrared fluorescence dye IRDye 800CW. Tumor uptake of the fluorescent tracers and their [89]Zr-labeled radioactive counterparts for PET is determined in human xenograft–bearing athymic mice during 1 week after tracer injection, followed by *ex vivo* biodistribution and pathologic examination. Intraoperative imaging of fluorescent VEGF- or HER2-positive tumor lesions is also performed in subcutaneous tumors and in intraperitoneal dissemination tumor models.

A summary of the obtained results in this thesis, a general discussion and prospects for future studies focusing on molecular imaging are described in

REFERENCES

1. Szakacs G, Paterson JK, Ludwig JA, Booth-Genthe C, Gottesman MM. Targeting multidrug resistance in cancer. Nat Rev Drug Discov. 2006;5:219-34.

2. Hanahan D, Weinberg RA. Hallmarks of cancer: the next generation. Cell. 2011;144:646-74.

3. de Bono JS, Ashworth A. Translating cancer research into targeted therapeutics. Nature. 2010;467:543-9.

4. Schilsky RL. Personalized medicine in oncology: the future is now. Nat Rev Drug Discov. 2010;9:363-6.

5. Baselga J, Swain SM. Novel anticancer targets: revisiting ERBB2 and discovering ERBB3. Nat Rev Cancer. 2009;9:463-75.

6. Pollak M. The insulin and insulin-like growth factor receptor family in neoplasia: an update. Nat Rev Cancer. 2012;12:159-69.

7. Gherardi E, Birchmeier W, Birchmeier C, Vande Woude G. Targeting MET in cancer: rationale and progress. Nat Rev Cancer. 2012;12:89-103.

8. Kerbel RS. Tumor angiogenesis. N Engl J Med. 2008;358:2039-49.

9. Ma XM, Blenis J. Molecular mechanisms of mTOR-mediated translational control. Nat Rev Mol Cell Biol. 2009;10:307-18.

10. Trepel J, Mollapour M, Giaccone G, Neckers L. Targeting the dynamic HSP90 complex in cancer. Nat Rev Cancer. 2010;10:537-49.

11. Terwisscha van Scheltinga AG, Lamberts LE, de Jong JR, Brouwers AH, Lub-de Hooge MN, de Vries EG. Molecular imaging of tumors with radioactive labeled antibodies from laboratory to the clinic. Am Assoc Cancer Res Educ Book 2012:227-232.

12. Gebauer M, Skerra A. Anticalins small engineered binding proteins based on the lipocalin scaffold. Methods Enzymol. 2012;503:157-88.

13. Carey L, Winer E, Viale G, Cameron D, Gianni L. Triple-negative breast cancer: disease entity or title of convenience? Nat Rev Clin Oncol. 2010;7:683-92.

14. Frangioni JV. New technologies for human cancer imaging. J Clin Oncol. 2008;26:4012-21.

CHAPTER 2

SPECT and PET imaging of multidrug resistance

Anton G.T. Terwisscha van Scheltinga[1,2], Wouter B. Nagengast[1],
Thijs H. Oude Munnink[1], Geke A.P. Hospers[1], Adrienne H. Brouwers[3],
Carolien P. Schröder[1], Marjolijn N. Lub-de Hooge[2,3,]
Elisabeth G.E. de Vries[1]

[1]Department of Medical Oncology, [2]Department of Hospital and Clinical Pharmacy, [3]Department of Nuclear Medicine and Molecular Imaging, University of Groningen, University Medical Center Groningen, Groningen, The Netherlands.

ABSTRACT

Multidrug resistance (MDR) is the resistance of tumor cells to several structurally unrelated classes of chemotherapeutic drugs from natural origin, including anthracyclines, taxanes and vinca alkaloids. Several mechanisms can attribute to MDR, including the expression of adenosine triphosphate binding cassette transporters (ABC transporters). These transporters, including P-glycoprotein (P-gp) and multidrug resistance protein (MRP), function as drug efflux pumps. To improve the understanding of their *in vivo* function, nuclear medicine imaging techniques have been developed to visualize the activity of these pumps. Several specific radionuclides have been used to this end, namely both gamma photon for e.g. single photon emission computed tomography (SPECT) and positron emitting for positron emitting tomography (PET) utilisation. The methods and possibilities to visualize these pumps in the tumor, the blood brain barrier and other locations will be discussed. The clinical relevance of these pumps in oncology appeared to be limited so far, as the addition of blockers of these pumps to chemotherapy did not improve cancer patient outcome. It has recently been shown that new targeted antitumor agents like poly (adenosine diphosphate (ADP) – ribose) polymerase (PARP) inhibitors are also substrates for P-gp. This finding may increase the interest for visualization of drug efflux pumps for future use in oncology. Also in other fields of clinical research, this interest remains, for instance in medication refractory epilepsy and Alzheimer's disease.

It is also becoming clear that MDR can be circumvented by the newer non-chemotherapeutic targeted agents. In that respect, also visualization of the targets of these new agents is relevant. These targets include the human epidermal growth factor receptor 2 (HER2) and angiogenic factors like vascular endothelial growth factor (VEGF). Molecular imaging allows not only visualization of these targets in preclinical models and cancer patients, but also the quantification of target modulation by specific drugs.

In conclusion, molecular imaging techniques can be used for evaluation of several aspects involved in MDR, including drug efflux pumps.

INTRODUCTION

Multidrug resistance (MDR) is the occurrence of resistance to structurally unrelated classes of chemotherapeutic drugs from natural origin, including anthracyclines, taxanes and vinca alkaloids. It can be present as intrinsic resistance of tumor cells or due to acquired resistance obtained during the course of chemotherapy treatment. MDR is due to several mechanisms including the expression of adenosine triphosphate (ATP)-binding cassette transporters (ABC transporters) which function as drug efflux pumps. These pumps include P-glycoprotein (P-gp) and multidrug resistance protein (MRP). P-gp and MRP both belong to ABC transporters superfamily. (1) The transporter gene ABCB1 (or MDR1) encodes P-gp, MRP1 and 2 are encoded by ABCC1 and 2. Another member of the ABC transporters is the breast cancer resistance protein (BCRP), which is encoded by ABCG2. Resistance can occur because increased drug efflux lowers the intracellular drug concentration. P-gp and MRP are also expressed in normal tissues, like intestine, liver, kidney, placenta, blood-testis barrier and the blood-brain-barrier (BBB), (2) and there is increasing knowledge available on their normal function and the role they play in various other non-cancerous disorders, such as medication refractory epilepsy and Alzheimer's disease. (3-4) The methods and possibilities to visualize these pumps in the tumor and brain have been developed, but the specific MDR tracers have not obtained a place in clinical practice yet. Recently it has been shown that new targeted antitumor agents like poly(adenosine diphosphate (ADP) – ribose) polymerase (PARP) inhibitors are also substrates for P-gp. (5-6) This finding may increase the interest for visualization of drug efflux pumps for future use in oncology. The radionuclides may also still be of value in the future for diseases outside oncology and in drug development.

It is increasingly becoming clear that the classical chemotherapeutic drugs have reached their maximum effect. The newly developed so-called targeted agents at least partly seem to offer benefit to patients. The opportunity to use novel imaging modalities and tracers to obtain insight in relevant pathways in tumor cells and their microenvironment is of major interest. Potentially this opens a strategy to apply personalized medicine with a relevant treatment selected for the individual patient.

In this chapter we will give an overview on imaging classical MDR mechanism in oncology and the use of imaging of these transporters in other tissues and diseases. We also show current knowledge on imaging cancer drug targets, like human epidermal growth factor receptor 2 (HER2) and vascular endothelial growth factor (VEGF) which can be used to guide therapies and thus potentially circumvent MDR in oncology.

Imaging of the efflux pumps

Especially gamma photon for e.g. single photon emission computed tomography (SPECT) and positron emitting for positron emitting tomography (PET) have been used to obtain insight in the role of P-gp and MRP in MDR.

MDR detection in tumor

Methoxyisobutyl isonitrile (MIBI/sestamibi) labeled with Technetium-99m (^{99m}Tc) is a gamma photon emitting tracer that is a substrate for P-gp as well as MRP. This radionuclide has been used as an *in vivo* marker of P-gp function in pre- and clinical studies including studies with P-gp pump modulators. (1) Tumor uptake of ^{99m}Tc-sestamibi is inversely related to the density of P-gp expression in breast and lung cancer patients. (7) During neoadjuvant therapy with epirubicin in breast cancer patients ^{99m}Tc-sestamibi tumor clearance rate (cut off ≤ 204 min) was tested as a predictive marker for response. (8) Of 17 patients with rapid tumor clearance of the tracer, 15 (88%) patients showed still macroscopic evidence of residual tumor. Only eight out of 22 (36%) patients with prolonged tracer uptake had pathologic evidence of residual tumor or showed only scattered and/or small clusters of tumor cells in a dense hyalinized stromal tissue in the resected tumor. This suggests that an increased P-gp and or MRP function is correlated to a lack of tumor response. However, the limited size of the study precluded firm conclusions on relationship between tracer uptake and treatment outcome. P-gp and MRP expression by the tumor were not determined, which makes it difficult to dissect whether the clearance rate was P-gp or MRP dependent. In parathyroid tumors P-gp and MRP1 expression determined with immunohistochemistry did not correlate with ^{99m}Tc-sestamibi uptake. (9)

Several other ^{99m}Tc-labeled tracers which are substrate for P-gp, such as ^{99m}Tc-tetrofosmin and ^{99m}Tc-Q complexes, have been evaluated in the clinic. In patients with hepatocellular carcinoma, ^{99m}Tc-tetrofosmin imaging displayed a very low sensitivity for the detection of this tumor. (10) This might well be due to rapid efflux of the tracer as hepatocellular carcinomas are considered to express high levels of P-gp and MRP1,2. Another study in this tumor type showed negative ^{99m}Tc-sestamibi scans in most patients (68 out of 78 patients) which correlated with positive P-gp expression in their tumor. (11) In patients with parathyroid adenomas ^{99m}Tc-tetrofosmin imaging showed tracer uptake, in those that were both P-gp and MRP negative by immunohistochemistry, while those with positive P-gp and/or MRP staining could not be detected with ^{99m}Tc-tetrofosmin imaging indicating a good correlation between imaging data and *ex vivo* analysis. (12)

Multiple studies analyzed the capacity of these scans to predict tumor response. In 20 patients with non-small cell lung cancer (NSCLC), a low baseline uptake of ^{99m}Tc-tetrofosmin was correlated with a poor response to paclitaxel based chemotherapy. The authors suggested that this was due to high MDR and/or P-gp expression. (13) Similar results were seen in patients with small cell lung cancer (SCLC) with ^{99m}Tc-tetrofosmin imaging prior to cisplatin and etoposide based chemotherapy. (14) All 16 patients with a negative scan prior to chemotherapy had a poor tumor response. However, also four out of 23 patients with a positive ^{99m}Tc-tetrofosmin image had a poor response. Furthermore, in patients with a negative ^{99m}Tc-tetrofosmin scan there was a poor correlation between tracer uptake and P-gp expression by the tumor. Six out of 16 patients without tracer uptake in the tumor had no P-gp expression immunohistochemically in their tumor. (14) These findings indicate that other factors apart from those involved in MDR contribute to tumor tracer uptake and the clearance of ^{99m}Tc-tetrofosmin. ^{99m}Tc-sestamibi imaging correlated with P-gp tumor expression in 30 NSCLC (stage IIIb and IV) patients. (15) All patients with a positive ^{99m}Tc-sestamibi

scan had negative P-gp expression and vice versa. The 15 patients with a complete or partial tumor response assessed three months after completion of the paclitaxel based chemotherapy had a positive 99mTc-sestamibi scan and negative P-gp staining. In the 15 non-responders five positive and 10 negative 99mTc-sestamibi scans prior to therapy were observed. Comparable with the 99mTc-tetrofosmin imaging, 99mTc-sestamibi imaging also yields false positive imaging. (14-15)

In 82 chemotherapy naive breast cancer patients, P-gp and MRP expression was measured with visual and quantitative indices of double-phase 99mTc-sestamibi scintimammography, quantifying an early and late tumor uptake. (16) Early (defined as 10 min post-injection of the tracer) and delayed (defined as 3 hour post-injection) tumor to normal tissue ratios (T/N ratio) were assessed by comparing the initial uptake of 99mTc-sestamibi and the wash-out rate of tracer out of the tumor. It was hypothesized that the wash-out rate was affected by the presence of P-gp or MRP. Both the early and delayed T/N ratio of the P-gp-negative and MRP-negative group was higher than of the P-gp-positive and MRP-positive group, without differences in wash-out rate according to P-gp and MRP expression as determined by immunohistochemistry. (16)

Apart from gamma photon radionuclides, also several PET tracers have been developed to analyze P-gp function, including 11C-verapamil, (17-18) 11C-colchicine, (19) 11C-daunorubicin, (17) 11C-carvedilol, (20) 18F-paclitaxel (21) and 18F-MPPF. (22) We analyzed the kinetics of 11C-verapamil administered as bolus in five cancer patients. One hour after injection, 11C-verapamil uptake in lungs, heart and tumor was respectively 43.0%, 1.3% and 0.9% of the injected verapamil dose. Half-lives of 11C-verapamil in these tissues were 46.2 min, 73.8 min and 23.7 min, respectively. (23) 11C-verapamil was mainly extracted by the lungs and efflux of 11C-verapamil, out of solid tumor tissue is relatively fast.

MRP function has been less extensively investigated with imaging methods. Leukotrienes (LT) are specific substrates for MRP, which makes N-11C-acetyl-LTE$_4$ an interesting PET tracer. (24) In MRP2 mutated GY/ TR⁻ rats, in which the MRP2 protein is defective due to MRP2 mutations, visualization of MRP-mediated transport was demonstrated. After injection of N-11C-acetyl-LTE$_4$, rapid elimination from the blood and transient accumulation of the 11C-tracer in the liver takes place in normal rats. GY/TR⁻ mutant rats showed delayed elimination of radioactivity from the blood, a delayed increase in hepatic N-11C-acetyl-LTE$_4$ and negligible amounts of radioactivity in the intestine when compared to normal rats. (24) This tracer permits the study of MRP transport function abnormalities *in vivo*, e.g. in Dubin-Johnson patients, who are MRP2 gene deficient.

The substrate specificity of MRP1 is similar to that of MRP2. Most substrates for the efflux pumps are conjugated to, or co-transported with, glutathione, glucuronide or sulfate. (25) We studied MRP2 in a different way, by analyzing the transporter specificity of the cholescintigraphic agents 99mTc-HIDA and 99mTc-sestamibi, which are used clinically for myocardial perfusion measurements. Secondly, we aimed to block MRP and P-gp transport to discriminate between the two transporters, which mediate the 99mTc-radionuclide pharmacokinetics *in vivo*. (25) We showed *in vitro* transporter specificity by measuring the accumulation of

radioactivity in the human SCLC cell lines GLC4, GLC4/ADR150x (MRP1-overexpressing/P-gp-negative) and GLC4/P-gp (P-gp-overexpressing, due to MDR1 transfection). ^{99m}Tc-HIDA accumulation was 5.8-fold lower in GLC4/ADR150x cells than in GLC4 or GLC4/P-gp cells. In GLC4/ADR150x, with high MRP expression the MRP1,2 inhibitor MK571 (50 µM) raised the cellular ^{99m}Tc-HIDA content 3.4-fold, while the MK571 had no measurable effect in GLC4 and GLC4/P-gp cells with low MRP expression. ^{99m}Tc-sestamibi accumulated less in GLC4/P-gp and GLC4/ADR150x cells than in GLC4 cells. *In vivo*, bile secretion of ^{99m}Tc-HIDA was impaired in GY/TR⁻ compared to control rats and not affected by glutathione. Hepatic secretion of ^{99m}Tc-HIDA was over 5-fold lower in GY/TR⁻ rats than in control rats. Bile secretion of ^{99m}Tc-sestamibi was similar in both rat strains and impaired by glutathione depletion in control rats only, indicating compensatory activity of additional transporter(s) in GY/TR- rats. ^{99m}Tc-HIDA is transported only by MRP1,2, while ^{99m}Tc-sestamibi is transported by P-gp as well as MRP1,2. The results indicate that hepatic P-gp and MRP1,2 function can be assessed *in vivo* by sequential use of both radiopharmaceuticals. (25)

To overcome MDR, many clinical trials have been performed by inhibiting the transporter, which yielded little success. The first generation P-gp competitive substrates were verapamil and cyclosporin. They showed the ability to inhibit the transporter but caused severe side-effects due to the doses needed for optimal inhibition. (26) Second generation inhibitors, like valspodar, were more potent and selective, but also caused toxicity and interactions with other drugs necessitating the need of dose-reduction of anticancer drugs by simultaneous administration. (26) The current third generation P-gp inhibitors are more P-gp specific. Tariquidar and zosuquidar are tested in clinical trials. (27-28) An approximately 5-fold higher expression of MDR1, leads to doxorubicin resistance in BRCA1-related breast cancer mouse models. (29) Tariquidar could completely reverse this resistant phenotype. The reasons of absence of success of P-gp inhibitors in clinical trials in cancer patients have been nicely summarized by Kannan *et al*. (30) They consider as most important factors responsible for this 1) the poor selectivity of P-gp inhibitors, 2) the alteration of pharmacokinetics by these inhibitors of chemotherapeutic agents, thereby causing toxicity and 3) a poor study design (dosing regimens and patient selection). Next to that, many studies were performed in cancer types whose major mode of resistance may not be (solely) P-gp mediated. (30)

Clinical trials with ^{99m}Tc-sestamibi have been performed with tariquidar and valspodar. (31 32) ^{99m}Tc-sestamibi scans in a phase I trial of tariquidar in combination with vinorelbine in 26 patients with metastatic cancers showed increased tumor uptake after P-gp inhibition in 13 of 17 patients with visible tumor masses by ^{99m}Tc-sestamibi. (31) Nine patients with metastatic renal carcinoma and one patient with adrenocortical cancer underwent three ^{99m}Tc-sestamibi scans namely a baseline scan, one after vinblastine treatment and one after inhibition with valspodar. In two patients the tumor was only visible on the scan after valspodar treatment, in other patients de uptake of ^{99m}Tc-sestamibi was enhanced after P-gp inhibition. (32)

A novel approach in oncology is the use of targeted agents. Several of these agents are also substrate for the drug efflux pumps such as erlotinib which is transported efficiently by P-gp and BCRP *in vitro*, imatinib

is transported by P-gp and BCRP. (33-34) PARP inhibitors, like olaparib, are substrates of P-gp. (5-6) PARP is important in the repair of single-strand DNA breaks. Inhibition of PARP induces DNA double-strand breaks which lead to DNA lesions. The BRCA mutation carriers, with a defect of homologous-recombination DNA-repair in the tumor, are highly sensitive for PARP inhibition, resulting in increased genomic instability. Several early clinical studies have been conducted with PARP inhibitors in BRCA mutation carriers which showed antitumor activity. (5) As with a lot of anticancer agents, resistance can occur against PARP inhibitors. Upregulation of P-gp is the most frequently observed mechanism of acquired resistance in animal models to the PARP-inhibitor olaparib. Upregulation of P-gp could effectively be blocked by a P-gp inhibitor, tariquidar, in a genetically engineered mouse model. (6) Imaging of the efflux pump P-gp might potentially give additional information about resistance development.

Apart from functional imaging, static whole body P-gp expression can also be assessed with the Indium-111 (^{111}In) labeled 15D3 monoclonal anti-P-gp. (35) In Nude BALB/c mice with subcutaneously growing human uterine sarcoma cell tumors derived of either high or low P-gp expression were used. The tracer uptake was higher in the high compared to low P-gp expressing tumors.

All the above examples illustrate that *in vivo* imaging of the function of ABC transporters involved in MDR in tumors is possible. There are however two nearly related reasons why functional imaging of the efflux pump play no role in current clinical practice: 1) adding blockers of the efflux pumps to chemotherapeutic drugs did not improve outcome for cancer patients and 2) the scan results are likely not dependent of expression of efflux pumps only. Despite these considerations, the use of these imaging modalities could be useful for new drugs which are substrate of the efflux pumps, like PARP inhibitors.

MDR detection in the brain

The BBB protects the brain against the entry of several drugs including cytotoxic, anti-epileptics and anti-HIV drugs. The BBB is formed by capillary endothelial cells that are connected by continuous tight intercellular junctions. The P-gp and MRP1,2 efflux pumps are also localized at the BBB. The capability of substances to enter the brain depends on molecular size, lipid solubility and the presence of a specific carrier-mediated transport system. Enhanced levels in the brain in P-gp knock-out mice versus wild-type mice were found for a variety of drugs e.g. ivermectin (antihelmintic drug), (36) verapamil (antiarrhythmicum), (37) digoxin (cardiac glycoside) (38) and nelfinavir (HIV protease inhibitor). (39) In P-gp knock-out mice, ^{99m}Tc-sestamibi uptake in the brain was only 4-fold higher. (40) Other radiotracers however showed higher uptake in P-gp knockout mice indicating that ^{99m}Tc-sestamibi is excreted by the cell by other mechanisms than only P-gp, like the MRP transporter. (41-43) Therefore, ^{99m}Tc-sestamibi is not an optimal substrate radioligand.

Strategies to analyze the role of P-gp in the BBB have been done with cyclosporin, as is shown in studies with rodents. (41, 44-45) P-gp transport in BBB has been visualized with ^{11}C-verapamil. Impressive increased tracer levels were found in brains (1280%) after inhibition of P-gp with cyclosporin. (44) The P-gp role in the

human BBB, was also analyzed with ^{11}C-verapamil and cyclosporin. (46) ^{11}C-verapamil was administered to healthy volunteers (six women and six men) as an iv infusion before and after at least one hour after infusion of cyclosporin (2.5 mg/kg/h). The brain uptake of ^{11}C-radioactivity was increased by 88% +/- 20% in the presence of cyclosporin without affecting ^{11}C-verapamil metabolism or plasma protein binding. The corresponding increases in ^{11}C-verapamil uptake in the brain white and gray matter were comparable. (46) Muzi *et al*. extended the noncompartmental analysis and applied compartmental modeling. (47) They concluded that a one-tissue-compartment model can be used to measure ^{11}C-verapamil transport. By using a short scan time (10 min) interference by labeled metabolites and tracer retention can be avoided in contrast to a two-tissue-compartment model. A one-tissue-compartment model provides an accurate estimation of P-gp activity at the BBB.

Another radiotracer which has been developed to measure the function of P-gp at the BBB is ^{11}C-N-Desmethyl-Loperamide (^{11}C-dLop). (43) Loperamide, used in the clinic to treat diarrhea, is an opiate without effects in de central nervous system. P-gp blocks its entry to the brain. First ^{11}C-loperamide was developed, but its injection led to accumulation of significant concentrations of radiometabolites, including ^{11}C-dLop also a substrate of P-gp, in the brain. (42) An injection of ^{11}C-dLop reduced radiometabolites in the brain. (43) ^{11}C-dLop has been measured in mice and monkeys to measure P-gp function. The radioligands showed a high brain uptake after the inactivation of P-gp by either genetic knockout or pharmacologic inhibition. (43, 48) ^{11}C-dLop has been tested in humans. Four healthy volunteers underwent a brain PET scan and eight subjects a whole body PET scan to measure radiation exposure, which was 7.8 ± 0.6 µSv/MBq. Low uptake of ^{11}C-dLop in the brain confirmed that it is a substrate for the transporter and negligible amounts of brain penetrating radiometabolites were generated. (49) ^{11}C-dLop can possibly be used as radiotracer to study the function of P-gp at the level of the blood–brain barrier.

Besides pharmacologic modulation of P-gp by specific substrates such as cyclosporin, also radiotherapy might influence P-gp function. Mima *et al*. exposed rat brain hemispheres to 25 Gy. (50) Five days after irradiation P-gp expression, measured with immunohistochemistry and Western blotting, was lower in the irradiated hemisphere compared to the non-irradiated hemisphere. We irradiated the right brain hemisphere of rats with single fractions of radiotherapy to elucidate whether radiation therapy reduced P-gp expression and function in the brain, as measured with the P-gp substrate ^{11}C-carvedilol. (51) The right hemispheres received single doses of 2-25 Gy followed by 10 mg/kg of the P-gp substrate cyclosporin iv, with once 15 Gy followed by cyclosporin, or with fractionated irradiation (4 x 5 Gy) followed by cyclosporin five days later. Irradiation increased ^{11}C-carvedilol uptake dose-dependently, to a maximum of 20% above non-irradiated hemisphere. Cyclosporin increased ^{11}C-carvedilol uptake dose-dependently in both hemispheres, but more in the irradiated hemisphere. Fractionated irradiation resulted in a lost P-gp expression 10 days after start of irradiation, which coincided with increased ^{11}C-carvedilol uptake. P-gp expression decreased between day 15 and 20 after single dose irradiation, and increased again thereafter. (51) These studies both indicate that radiotherapy influences both P-gp expression and P-gp function.

Summarizing, potential application of functional analyses of efflux pump function at the BBB lies in the analysis of brain uptake of drugs and interference of drugs at the brain level.

New indications for MDR detection

Besides various tumor tissues and the BBB, several normal tissues (such as the intestine, liver, kidney, placenta and blood-testis barrier) express the transporters P-gp and MRP. The transporters exert there a protective role and facilitate the elimination of toxic compounds, by excreting substrates into the urine, the bile and the faeces. (52) P-gp expression varies among organs; these varying densities of P-gp influences the inhibitor dose necessary to enhance a substrate signal in a specific organ. (53) Given the extensive expression of P-gp in human body, P-gp imaging could provide additional information about several disorders and physiological mechanisms.

P-gp is increasingly suspected to play a role in medication-refractory epilepsy which is interesting for imaging. One pilot imaging study has been performed in seven patients with ^{11}C-verapamil. (3) No significant differences were found between epileptogenic and the non-epileptogenic brain regions.

Another P-gp radioligand is ^{125}I-amyloid-β_{40}. Brain accumulation of amyloid-β, an insoluble fibrous protein, in the brain occurs during Alzheimer's disease. A role for P-gp in brain deposition of amyloid-β was suggested in a preclinical study. (4) P-gp knock-out mice were compared to wild-type mice with regard to ^{125}I-amyloid-β_{40} deposition, this was higher in P-gp knock-out mice. Inhibition of P-gp increased amyloid-β deposition, indicating a potential function of P-gp to transport amyloid-β out of the brain. Therefore P-gp could be a diagnostic target for Alzheimer's disease. (4)

Parkinson's disease is a neurodegenerative disease which results in a movement disorder. A decreased P-gp expression could contribute to its pathogenesis through lower efflux of toxins out of the brain. The first study with ^{11}C-verapamil in Parkinson's disease patients showed a decreased P-gp function in the midbrain where the dopamine neurons, which degenerate in Parkinson's disease, are located. (54) In other studies performed by Bartels *et al.* (55-56) there was no involvement of P-gp in the development of neurotoxic events leading to Parkinson's disease. In ten early stage Parkinson's disease patients and eight healthy control subjects BBB P-gp function was measured using ^{11}C-verapamil. (55) Decreased P-gp function was only seen in late event neurodegenerative disorders. (56)

The biological and clinical role of drug transporters at the intestinal barrier has been described by Oostendorp *et al*. Oral administration of cancer drugs is in development and the availability of oral anti-cancer drugs is increasing. (57) ABC transporters have an important role in the pharmacokinetics of a broad range of drugs. ABC transporters excrete drugs, xenobiotics and metabolites from the intestine, in an active ATP dependent manner, and can pump against concentration gradients. The transporters prevent drug absorption into the blood or lymph circulation and protect the body against acute and chronic toxicity of toxins. (58-59) An example is the absorption of erlotinib, a small-molecule, orally active, selective, and reversible epidermal

growth factor receptor (EGFR) 1 tyrosine kinase inhibitor (TKI). Absence of P-gp significantly increased the oral bioavailability of erlotinib preclinical. (33) Preclinical and clinical modulations of the activity of intestinal transporters, to increase the systemic exposure of orally administered drugs, have been performed. Cyclosporin has been used as an inhibitor of P-gp to increase the bioavailability of paclitaxel and docetaxel. (60-61) Elacridar, a third generation P-gp inhibitor, increased the systemic exposure of oral topotecan in patients. (62-63) The ABC transporters can have a profound effect on the absorption, variability and disposition of a wide range of orally administered drugs. Imaging of the efflux pumps could provide additional information to predict the intestinal absorption of drugs.

In vivo imaging of the function of ABC transporters could give further insight in their role in the different tissues. The knowledge and experiences of MDR imaging in tumors could be of use in the imaging of other tissues than tumor.

Imaging of molecular targets for molecular targeted drugs that could sensitize tumor cells to MDR related chemotherapeutic drugs.

Several new anticancer agents have entered the clinic. Many of these agents are specifically designed to target receptors, intracellular proteins or ligands which are over expressed by tumor cells. Well known examples are the monoclonal antibodies trastuzumab and bevacizumab, both improving treatment outcome when combined with MDR related chemotherapeutic drugs. Trastuzumab binds to the HER2 receptor, bevacizumab binds to VEGF-A. Combining trastuzumab with paclitaxel or docetaxel leads to increased progression free survival and overall survival in metastatic breast cancer. (64-65) Combining bevacizumab with paclitaxel or docetaxel also increases progression free survival in metastatic breast cancer. (66-67) Visualizing the specific molecular drug targets in the tumor could guide therapy for the individual patient. HER2 imaging and VEGF imaging are discussed as examples of this new imaging approach. Furthermore, several other tumor characteristics are candidate for development of tumor specific tracers, which are also specified.

HER2 imaging

HER2 is a member of the ErbB tyrosine kinase receptor family and is composed of an extracellular domain, a transmembrane segment and an intracellular protein tyrosine kinase domain. (68) It is encoded by the HER2/neu proto-oncogene and is involved in cellular growth, survival, proliferation and maturation in metastases and angiogenesis, and has anti-apoptotic effects. HER2 overexpression occurs in 20-30% of all breast cancers and in around 20% of gastric cancers. (69-71) Trastuzumab is a recombinant IgG1 monoclonal antibody targeting the extracellular domain of HER2 and is used in the treatment of patients with HER2 overexpressing breast cancer. Trastuzumab potentiates the antitumor effect of the MDR drugs, the anthracylcines and taxanes, and reduces resistance as a consequence. In the clinic, combination with anthracyclines is not possible due to induced cardiotoxicity. HER2 tumor expression can vary during treatment and can differ across metastatic lesions within a patient. (72)

Selecting a suitable HER2 targeting ligand is the first step to HER2 imaging. Full length monoclonal antibodies, Fab-fragments, F(ab')$_2$-fragments, diabodies, minibodies, affibodies, scFv-Fc and peptides are available as HER2 targeting ligands. (73) For radiolabeling these ligands, the physical half-life of the radio isotope should suit the biological half-life of the ligand to allow imaging at the time-point of optimal tumor-to-nontumor ratio. Full-length monoclonal antibodies are mostly radiolabeled with long-lived isotopes while the smaller HER2 ligands, which have a more rapid clearance, are radiolabeled with shorter-lived isotopes. Full-length HER2 monoclonal antibodies have been labeled with ^{131}I, ^{111}In and ^{99m}Tc for HER2 SPECT/gamma camera imaging and with ^{124}I, ^{86}Y, ^{76}Br and ^{89}Zr for HER2 PET. (73) The smaller HER2 targeting antibody fragments, proteins and peptides have been labeled with ^{111}In, ^{131}I and ^{99m}Tc for HER2 SPECT/gamma camera imaging and with ^{18}F, ^{68}Ga, ^{64}Cu, ^{124}I and ^{76}Br for HER2 PET. (73)
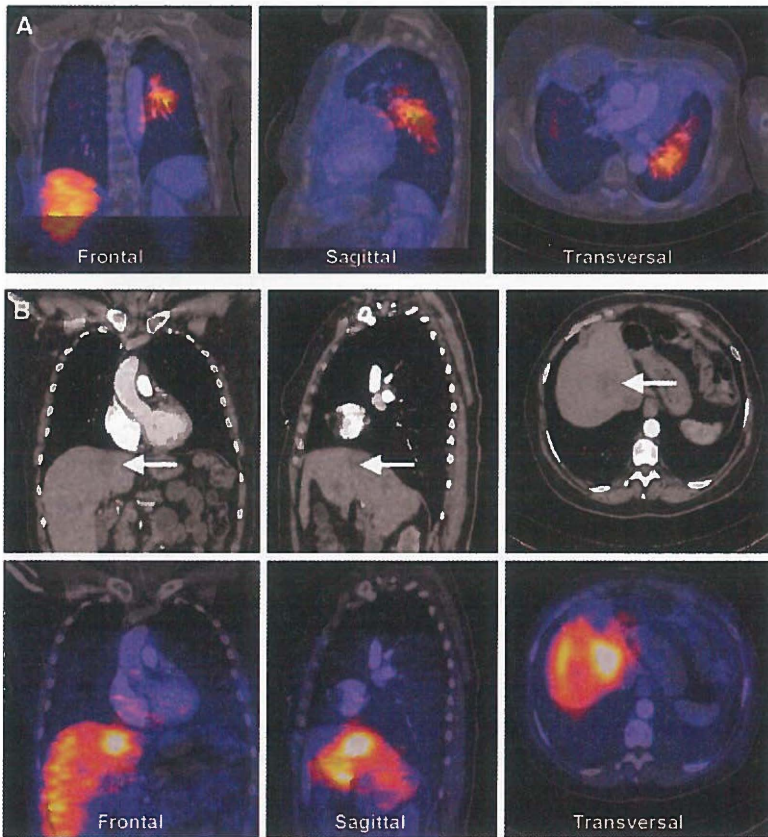
Figure 1 | (A) Fused computed tomography (CT) with indium-111–diethylenetriamine penta-acetic acid anhydride (^{111}In-DTPA) –trastuzumab single-photon emission tomography (SPECT) image (96 hours after tracer injection). (B) CT images (top) of a patient with a large liver metastasis. Fusion with ^{111}In-DTPA-trastuzumab SPECT (bottom) shows correspondence of liver metastases and SPECT hot spot. Reprinted from The Journal of Clinical Oncology with permission of the American Society of Clinical Oncology. (75)

We developed ^{111}In-labeled trastuzumab and imaged HER2 in patients with HER2 positive metastatic breast cancer (Fig. 1). (74-75) This SPECT tracer was able to visualize previously unidentified lesions in 13 out of 15 patients. Since PET imaging provides a higher spatial resolution, a better signal-to-noise ratio and is potentially more quantitative than SPECT, we have developed Zirconium-89 ([89]Zr) labeled trastuzumab and evaluated it for clinical HER2 PET imaging in metastatic breast cancer patients (Fig. 2). (76) [89]Zr-trastuzumab imaging shows excellent tumor tracer uptake and can be used to detect HER2 positive breast cancer metastases and to quantify [89]Zr-trastuzumab uptake. [89]Zr-trastuzumab PET-imaging detected known tumor lesions in the liver, lung, bone and brain as well as unknown brain and bone lesions. (77)
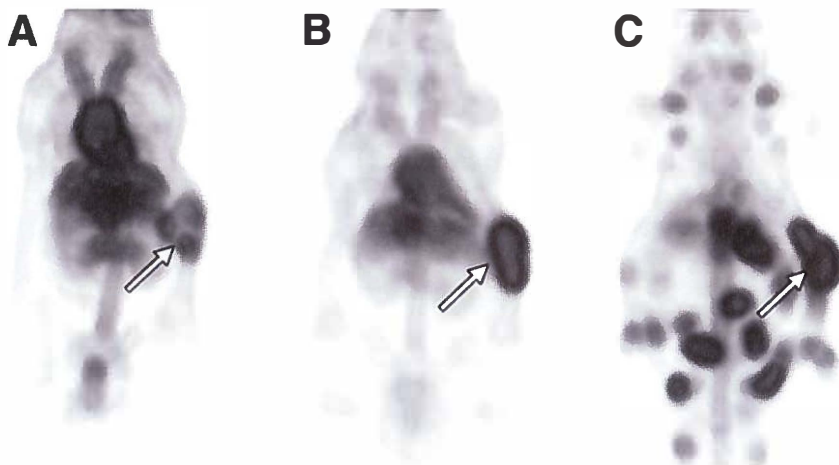
Figure 2 I Examples of noninvasive small-animal PET images (dorsal presentation). [89]Zr-trastuzumab uptake in human SKOV-3 xenografts in 3 mice at 6 h (A), day 1 (B), and day 6 (C, metastasized tumor) after injection is shown. Primary tumors are indicated by arrows. Reprinted from the Journal of Nuclear Medicine with permission of the Society of Nuclear Medicine. (76)

Treatment effect on HER2 expression could potentially also be analyzed with these techniques. Heat shock protein 90 (HSP90). HSP90 is a molecular chaperone protein which is involved in the conformation, activation, functionality, and stability of over a hundred client proteins. Client proteins of HSP90 include the key regulator of VEGF expression, namely hypoxia inducible factor (HIF-1α), and also HER2, hormone receptors and others. (78) The rapid but transient HER2 downregulation by a HSP90 inhibitor has been shown in several preclinical reports, both *in vitro* and *in vivo*. (79-82) The effect of 17-allylamino-17-demethoxygeldanamycin (17-AAG), a HSP90 inhibitor, on HER2 has been studied by HER2 imaging with a ^{68}Ga labeled F(ab')$_2$ fragment of trastuzumab (DCHF) in a preclinical model. Tumor uptake of ^{68}Ga-DCHF was reduced by 50% after treatment with 17-AAG, compared to baseline ^{68}Ga-DCHF tumor uptake. (83) With [18]FDG-PET there was no significant difference in tumor uptake between 17-AAG treated and control mice in the 3 weeks post treatment. (84) The early response to HSP90 inhibition with 17-dimethylaminoethylamino-17-demethoxygeldanamycin (17-DMAG) was successfully monitored preclinically by quantitative PET using

[64]Cu-trastuzumab. (85) We showed a 41% decrease of [89]Zr-trastuzumab uptake by the new HSP90 inhibitor NVP-AUY922 in a tumor xenograft (Fig. 3). (86) HER2 PET provides a tool to image and quantify the reduction in HER2 expression in the tumor following HSP90 inhibition non-invasively. Since the [89]Zr-trastuzumab PET tracer has been already used clinically, this technique can potentially easily be used to determine the early molecular effects of HSP90 inhibitors in patients. (86)
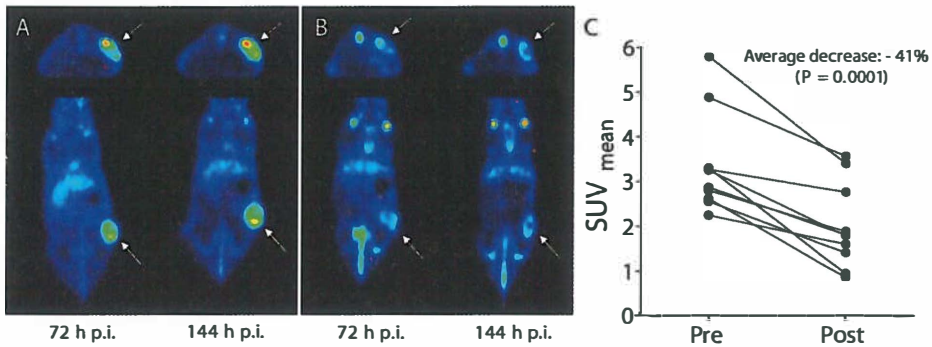
Figure 3 | Transversal and coronal PET images of a representative mouse scanned with [89]Zr-trastuzumab before (A) and after (B) treatment with NVP-AUY922. Arrows indicate tumor. PET quantification of [89]Zr-trastuzumab tumor uptake at 144 h post injection is shown in C. Reprinted from the European Journal of Cancer with permission of Elsevier. (86)

The clinical success of trastuzumab is limited by resistance for this drug, which can among others be due to alterations in receptor-antibody interaction. HER2 imaging could therefore potentially be used to elucidate altered receptor-antibody interaction in trastuzumab resistant tumors. (87) A number of other mechanisms in trastuzumab resistance are increased signaling of the HER receptor family, altered signaling pathway, and insuline-like growth factor 1 receptor (IGF-1R) overexpression. (87) IGF-1R imaging with an [89]Zr-labeled IGF-1R antibody could therefore potentially be used for imaging a new drug target when trastuzumab resistance has occurred.

VEGF level imaging
Increased forming of new blood vessels, usually called angiogenesis, is important for the growth of tumors. One of the most important factors involved in angiogenesis is VEGF. In tumor cells there is an unproportional upregulation of VEGF production which leads to locally high VEGF levels. HIF-1α is one of the cellular key regulators of the transcription of VEGF and is also involved in chemotherapeutic drug resistance, for example, by increased transcription of the MDR1 gene, resulting in increased P-gp expression. (88-89)

Bevacizumab is a humanized monoclonal antibody which neutralizes all isoforms of VEGF-A. In patients with metastatic breast carcinoma, addition of bevacizumab to the MDR associated taxanes leads to an increased response rate and increased progression free survival, and thus decreasing drug resistance. (66-67) Apart from this antibody several TKIs, which block the signal transduction of VEGF receptors on endothelial and tumor cells, are now available.

There are several novel anti-angiogenic approaches currently tested in the clinic. HSP90 inhibitors are evaluated for reduction of angiogenesis through for instance HIF-1α inhibition which results in a reduction of VEGF secretion and other HIF-1α activated genes. (79, 90-91) Another example is the mammalian target of rapamycin (mTOR) pathway plays a key role in regulating cancer cell proliferation, tumor growth and angiogenesis through altering HIF-1α and VEGF expression by its upstream pathways such as phosphoinositide 3-kinases (PI3Ks), AKT and extracellular signal-regulated kinases (ERKs). (92) Furthermore, the mTOR pathway is involved in specific drug resistance mechanisms. For example, upstream PI3K activation leads to MRP1 expression and subsequent chemoresistance in advanced prostate cancer cells. (93) These examples illustrate the close and complex interaction between classic chemotherapeutic MDR, angiogenesis and tumor progression. Therefore, new anti-angiogenic therapies, such as HSP90 and mTOR inhibition, may facilitate to overcome resistance to classic chemotherapeutics and targeted therapies.

To select patients who could benefit from VEGF targeted therapies, and to follow up new treatment regimes, imaging of VEGF using specific tracers, is of great interest. Furthermore, VEGF imaging could give insight in drug resistance for trastuzumab. For example, acquired resistance in a breast cancer xenograft model for trastuzumab was associated with increased expression of VEGF. (94)

Several radiolabeled anti-VEGF antibodies and Fab-fragments have been used for the development of VEGF imaging: VG76e, HumMV833, bevacizumab and ranibizumab. (95-97) Radiolabeled bevacizumab showed specific tumor uptake in a human ovarian xenograft model. (97) MicroPET imaging using [89]Zr-bevacizumab showed clear tumor localization 72 h post injection with maximal uptake 168 h post injection. (97) Uptake could be quantified non-invasively, allowing follow-up of VEGF secretion during therapy. Comparable results were seen using [89]Zr- and Fluor-18 (^{18}F) labeled ranibizumab, a Fab-fragment binding to all VEGF-A isoforms. Although, due to fast distribution and clearance of the Fab-fragment images could be obtained earlier; already 3 h post injection of the tracer, absolute tumor uptake is lower compared to bevacizumab. (98) We showed that [89]Zr-ranibizumab was able to monitor locoregional changes in tracer uptake during sunitinib treatment, a VEGF-receptor TKI. [89]Zr-ranibizumab revealed an inhomogeneous change in tumor uptake with a rebound phenomenon after stopping sunitinib treatment, resulting in 69.5% increased tracer uptake which corresponded with rapid tumor growth and an increase of plasma human VEGF levels. (99)

[125]I- and [124]I-labeled VG76e is an IgG1 mouse monoclonal anti-VEGF antibody which recognizes the 121, 165 and 189 isoforms of human VEGF-A. (95) It showed specific tumor targeting in a human fibrosarcoma xenograft mice model. [124]I-HuMV833, a humanized monoclonal IgG4$_k$ antibody that binds VEGF$_{121}$ and VEGF$_{165}$, was administered for PET-imaging studies in patients with various progressive solid tumors. (96) Tumor uptake of [124]I-HuMV833 was highly variable between and within patients.

SPECT imaging using ^{111}In labeled bevacizumab revealed tumor lesions in both recurrent melanoma and metastatic colon cancer patients. (100) A study to determine the expression of VEGF-A in liver metastases in 12 patients with colorectal cancer showed no correlation between the antibody accumulation and VEGF-A

expression. Liver metastases were shown in 9 patients and ^{111}In labeled bevacizumab uptake varied considerably. (101)

Angiogenesis can also be visualized by targeting the $\alpha_v\beta_3$ integrin receptor with Arg–Gly–Asp (RGD) tripeptide. (102-103) Clinical trials have been performed with ^{18}F-AH111585 and ^{18}F-Galacto-RGD. Uptake of ^{18}F-AH111585 in 7 metastatic breast cancer patients visualized all 18 lesions shown on CT, the uptake in tumor was either homogeneous or appeared within the tumor rim. (102) In 16 patients with primary or metastatic breast cancer, imaging with ^{18}F-Galacto-RGD identified all invasive carcinomas, known lymph-node metastases were only seen in 3 of 8 patients. (103)

Other Targets for molecular cancer imaging

There are several tumor characteristics candidate for development of tumor specific tracers. (104) Cetuximab is an antibody directed against EGFR, and is used in the clinic for different forms of cancer. Several tracers have been developed for EGFR imaging, such as radiolabeled EGFR TKIs and the EGFR ligand epidermal growth factor or EGFR antibodies. (105) Another target for molecular imaging is transforming growth factor beta (TGF-β). The crucial role of TGF-β in the metastasizing process becomes more and more elucidated. (106) TGF-β and TGF-βR targeting therapies are currently in clinical trials. Imaging TGF-β could help to select patients for and to monitor TGF-β targeting therapies. IGF-1R is a transmembrane receptor tyrosine kinase receptor which is important receptor in tumor growth. If its ligand, insulin-like growth factor 1 binds to the receptor, it induces cell proliferation and inhibition of apoptosis. IGF-1R plays also a role in differentiation, malignant transformation and cell-cell adhesion. Overexpression of IGF-1R has been shown in numerous solid tumors. (107) IGF-1R is for instance implicated in resistance to HER2 targeting. (108) Drugs directed against the IGF-1R are underway, just like the tracers for imaging this receptor are in development. (109-110) A phase II study with the IGF-1R antibody CP-751,871 in combination with paclitaxel and carboplatin has been conducted in NSCLC patients with promising results. (111) IGF-1R overexpression seems to be involved in the process of MDR. The therapeutic effect of chemotherapy could be predicted by the level of co-expression of IGF-1R and MRP1 in gastric carcinoma. (112) In conclusion, several tumor characteristics are used or candidate for development of tumor specific tracers. Visualization is relevant because it is becoming clear that MDR can potentially be circumvented by the newer non-chemotherapeutic targeted agents.

CONCLUSION

The ability of tumors to develop MDR remains an important problem in the treatment of cancers.

To study ways to overcome MDR, tracers have been developed for *in vivo* imaging of the function of ABC transporters involved in MDR in tumors and BBB. The clinical impact of MDR imaging is currently small.

However, these tracers and imaging modalities can have a role in the development of P-gp inhibitors. Drug distribution can be followed and patients can be selected for P-gp inhibitor treatment. The use of blockers to improve effects of chemotherapeutic drugs in cancer turned out not to improve outcome for these patients. MDR imaging results are likely not dependent of expression of efflux pumps only which explains the limited role in clinic. However, the developed imaging modalities may be of use in new drug development, e.g. PARP inhibitors, or in other tissues like the intestines.

To increase the efficacy of chemotherapy, new targeted agents have to be added. At this moment, blockade of specific growth factor receptors and intracellular targets have increased the efficacy of classic chemotherapy in several cancer types. However, not all patients do benefit of these targeted therapies. Tracer development and (pre-)clinical trials directed at the MDR efflux transporter have lead to knowledge and experience which currently can be used to develop new tracers and imaging modalities which represent changes in the tumor microenvironment and relevant pathways in tumor cells. Potentially this opens a strategy to apply personalized medicine with a relevant treatment selected for the individual patient. There are several tumor characteristics candidate for development of tumor specific tracers. Imaging drug targets, as mentioned, like HER2 and VEGF, can be used to direct drugs at and increase the effect of MDR related chemotherapeutic drugs. A more patient tailored therapy can be obtained by using these tracers for patient selection. The new developed tracers can also play an important role as biomarker in drug development.

Disclosure of potential conflicts of interest
None to disclose.

REFERENCES

1. Hendrikse NH, Franssen EJ, van der Graaf WT, Vaalburg W, de Vries EG. Visualization of multidrug resistance in vivo. Eur J Nucl Med. 1999;26:283-93.

2. Gottesman MM, Fojo T, Bates SE. Multidrug resistance in cancer: role of ATP-dependent transporters. Nat Rev Cancer. 2002;2:48-58.

3. Langer O, Bauer M, Hammers A, Karch R, Pataraia E, Koepp MJ, et al. Pharmacoresistance in epilepsy: a pilot PET study with the P-glycoprotein substrate R-[(11)C]verapamil. Epilepsia. 2007;48:1774-84.

4. Cirrito JR, Deane R, Fagan AM, Spinner ML, Parsadanian M, Finn MB, et al. P-glycoprotein deficiency at the blood-brain barrier increases amyloid-beta deposition in an Alzheimer disease mouse model. J Clin Invest. 2005;115:3285-90.

5. Fong PC, Boss DS, Yap TA, Tutt A, Wu P, Mergui-Roelvink M, et al. Inhibition of poly(ADP-ribose) polymerase in tumors from BRCA mutation carriers. N Engl J Med. 2009;361:123-34.

6. Rottenberg S, Jaspers JE, Kersbergen A, van der Burg E, Nygren AO, Zander SA, et al. High sensitivity of BRCA1-deficient mammary tumors to the PARP inhibitor AZD2281 alone and in combination with platinum drugs. Proc Natl Acad Sci U S A. 2008;105:17079-84.

7. Kostakoglu L, Elahi N, Kiratli P, Ruacan S, Sayek I, Baltali E, et al. Clinical validation of the influence of P-glycoprotein on technetium-99m-sestamibi uptake in malignant tumors. J Nucl Med. 1997;38:1003-8.

8. Ciarmiello A, Del Vecchio S, Silvestro P, Potena MI, Carriero MV, Thomas R, et al. Tumor clearance of technetium 99m-sestamibi as a predictor of response to neoadjuvant chemotherapy for locally advanced breast cancer. J Clin Oncol. 1998;16:1677-83.

9. Jorna FH, Hollema H, Hendrikse HN, Bart J, Brouwers AH, Plukker JT. P-gp and MRP1 expression in parathyroid tumors related to histology, weight and 99 mTc-sestamibi imaging results. Exp Clin Endocrinol Diabetes. 2009;117:406-12.

10. Ho YJ, Jeng LB, Yang MD, Kao CH, Lin CC, Lee CC. A trial of single photon emission computed tomography of the liver with technetium-99m tetrofosmin to detect hepatocellular carcinoma. Anticancer Res. 2003;23:1743-6.

11. Wang H, Chen XP, Qiu FZ. Correlation of expression of multidrug resistance protein and messenger RNA with 99mTc-methoxyisobutyl isonitrile (MIBI) imaging in patients with hepatocellular carcinoma. World J Gastroenterol. 2004;10:1281-5.

12. Shiau YC, Tsai SC, Wang JJ, Ho ST, Kao A. Detecting parathyroid adenoma using technetium-99m tetrofosmin: comparison with P-glycoprotein and multidrug resistance related protein expression--a preliminary report. Nucl Med Biol. 2002;29:339-44.

13. Kao CH, Hsieh JF, Tsai SC, Ho YJ, Changlai SP, Lee JK. Paclitaxel-Based chemotherapy for non-small cell lung cancer: predicting the response with 99mTc-tetrofosmin chest imaging. J Nucl Med. 2001;42:17-20.

14. Yeh JJ, Hsu WH, Huang WT, Wang JJ, Ho ST, Kao A. Technetium-99m tetrofosmin SPECT predicts chemotherapy response in small cell lung cancer. Tumour Biol. 2003;24:151-5.

15. Hsu WH, Yen RF, Kao CH, Shiun SC, Hsu NY, Lin CC, et al. Predicting chemotherapy response to paclitaxel-based therapy in advanced non-small-cell lung cancer (stage IIIb or IV) with a higher T stage (> T2). Technetium-99m methoxyisobutylisonitrile chest single photon emission computed tomography and P-glycoprotein express ion. Oncology. 2002;63:173-9.

16. Kim IJ, Bae YT, Kim SJ, Kim YK, Kim DS, Lee JS. Determination and prediction of P-glycoprotein and multidrug-resistance-related protein expression in breast cancer with double-phase technetium-99m sestamibi scintimammography. Visual and quantitative analyses. Oncology. 2006;70:403-10.

17. Elsinga PH, Franssen EJ, Hendrikse NH, Fluks L, Weemaes AM, van der Graaf WT, et al. Carbon-11-labeled daunorubicin and verapamil for probing P-glycoprotein in tumors with PET. J Nucl Med. 1996;37:1571-5.

18. Luurtsema G, Molthoff CF, Windhorst AD, Smit JW, Keizer H, Boellaard R, et al. (R)- and (S)-[11C]verapamil as PET-tracers for measuring P-glycoprotein function: in vitro and in vivo evaluation. Nucl Med Biol. 2003;30:747-51.

19. Levchenko A, Mehta BM, Lee JB, Humm JL, Augensen F, Squire O, et al. Evaluation of 11C-colchicine for PET imaging of multiple drug resistance. J Nucl Med. 2000;41:493-501.

20. Bart J, Dijkers EC, Wegman TD, de Vries EG, van der Graaf WT, Groen HJ, et al. New positron emission tomography tracer [(11)C]carvedilol reveals P-glycoprotein modulation kinetics. Br J Pharmacol. 2005;145:1045-51.

21. Kurdziel KA, Kiesewetter DO, Carson RE, Eckelman WC, Herscovitch P. Biodistribution, radiation dose estimates, and in vivo Pgp modulation studies of 18F-paclitaxel in nonhuman primates. J Nucl Med. 2003;44:1330-9.

22. Passchier J, van Waarde A, Doze P, Elsinga PH, Vaalburg W. Influence of P-glycoprotein on brain uptake of [18F] MPPF in rats. Eur J Pharmacol. 2000;407:273-80.

23. Hendrikse NH, de Vries EG, Franssen EJ, Vaalburg W, van der Graaf WT. In vivo measurement of [11C]verapamil kinetics in human tissues. Eur J Clin Pharmacol. 2001;56:827-9.

24. Guhlmann A, Krauss K, Oberdorfer F, Siegel T, Scheuber PH, Muller J, et al. Noninvasive assessment of hepatobiliary and renal elimination of cysteinyl leukotrienes by positron emission tomography. Hepatology. 1995;21:1568-75.

25. Hendrikse NH, Kuipers F, Meijer C, Havinga R, Bijleveld CM, van der Graaf WT, et al. In vivo imaging of hepatobiliary transport function mediated by multidrug resistance associated protein and P-glycoprotein. Cancer Chemother Pharmacol. 2004;54:131-8.

26. Szakacs G, Paterson JK, Ludwig JA, Booth-Genthe C, Gottesman MM. Targeting multidrug resistance in cancer. Nat Rev Drug Discov. 2006;5:219-34.

27. Abraham J, Edgerly M, Wilson R, Chen C, Rutt A, Bakke S, et al. A phase I study of the P-glycoprotein antagonist tariquidar in combination with vinorelbine. Clin Cancer Res. 2009;15:3574-82.

28. Ruff P, Vorobiof DA, Jordaan JP, Demetriou GS, Moodley SD, Nosworthy AL, et al. A randomized, placebo-controlled, double-blind phase 2 study of docetaxel compared to docetaxel plus zosuquidar (LY335979) in women with metastatic or locally recurrent breast cancer who have received one prior chemotherapy regimen. Cancer Chemother Pharmacol. 2009;64:763-8.

29. Pajic M, Iyer JK, Kersbergen A, van der Burg E, Nygren AO, Jonkers J, et al. Moderate increase in Mdr1a/1b expression causes in vivo resistance to doxorubicin in a mouse model for hereditary breast cancer. Cancer Res. 2009;69:6396-404.

30. Kannan P, John C, Zoghbi SS, Halldin C, Gottesman MM, Innis RB, et al. Imaging the Function of P-Glycoprotein With Radiotracers: Pharmacokinetics and In Vivo Applications. Clin Pharmacol Ther. 2009;86:368-77.

31. Agrawal M, Abraham J, Balis FM, Edgerly M, Stein WD, Bates S, et al. Increased 99mTc-sestamibi accumulation in normal liver and drug-resistant tumors after the administration of the glycoprotein inhibitor, XR9576. Clin Cancer Res. 2003;9:650-6.

32. Chen CC, Meadows B, Regis J, Kalafsky G, Fojo T, Carrasquillo JA, et al. Detection of in vivo P-glycoprotein inhibition by PSC 833 using Tc-99m sestamibi. Clin Cancer Res. 1997;3:545-52.

33. Marchetti S, de Vries NA, Buckle T, Bolijn MJ, van Eijndhoven MA, Beijnen JH, et al. Effect of the ATP-binding cassette drug transporters ABCB1, ABCG2, and ABCC2 on erlotinib hydrochloride (Tarceva) disposition in in vitro and in vivo pharmacokinetic studies employing Bcrp1-/-/Mdr1a/1b-/- (triple-knockout) and wild-type mice. Mol Cancer Ther. 2008;7:2280-7.

34. Oostendorp RL, Buckle T, Beijnen JH, van Tellingen O, Schellens JH. The effect of P-gp (Mdr1a/1b), BCRP (Bcrp1) and P-gp/BCRP inhibitors on the in vivo absorption, distribution, metabolism and excretion of imatinib. Invest New Drugs. 2009;27:31-40.

35. van Eerd JE, de Geus-Oei LF, Oyen WJ, Corstens FH, Boerman OC. Scintigraphic imaging of P-glycoprotein expression with a radiolabelled antibody. Eur J Nucl Med Mol Imaging. 2006;33:1266-72.

36. Schinkel AH, Smit JJ, van Tellingen O, Beijnen JH, Wagenaar E, van Deemter L, et al. Disruption of the mouse mdr1a P-glycoprotein gene leads to a deficiency in the blood-brain barrier and to increased sensitivity to drugs. Cell. 1994;77:491-502.

37. Doran A, Obach RS, Smith BJ, Hosea NA, Becker S, Callegari E, et al. The impact of P-glycoprotein on the disposition of drugs targeted for indications of the central nervous system: evaluation using the MDR1A/1B knockout mouse model. Drug Metab Dispos. 2005;33:165-74.

38. Mayer U, Wagenaar E, Beijnen JH, Smit JW, Meijer DK, van Asperen J, et al. Substantial excretion of digoxin via the intestinal mucosa and prevention of long-term digoxin accumulation in the brain by the mdr 1a P-glycoprotein. Br J Pharmacol. 1996;119:1038-44.

39. Choo EF, Leake B, Wandel C, Imamura H, Wood AJ, Wilkinson GR, et al. Pharmacological inhibition of P-glycoprotein transport enhances the distribution of HIV-1 protease inhibitors into brain and testes. Drug Metab Dispos. 2000;28:655-60.

40. Piwnica-Worms D, Kesarwala AH, Pichler A, Prior JL, Sharma V. Single photon emission computed tomography and positron emission tomography imaging of multi-drug resistant P-glycoprotein--monitoring a transport activity important in cancer, blood-brain barrier function and Alzheimer's disease. Neuroimaging Clin N Am. 2006;16:575-89.

41. Hendrikse NH, Schinkel AH, de Vries EG, Fluks E, Van der Graaf WT, Willemsen AT, et al. Complete in vivo reversal of P-glycoprotein pump function in the blood-brain barrier visualized with positron emission tomography. Br J Pharmacol. 1998;124:1413-8.

42. Zoghbi SS, Liow JS, Yasuno F, Hong J, Tuan E, Lazarova N, et al. 11C-Loperamide and its N-desmethyl radiometabolite are avid substrates for brain permeability-glycoprotein efflux. J Nucl Med. 2008;49:649-56.

43. Lazarova N, Zoghbi SS, Hong J, Seneca N, Tuan E, Gladding RL, et al. Synthesis and evaluation of [N-methyl-11C]N-desmethyl-loperamide as a new and improved PET radiotracer for imaging P-gp function. J Med Chem. 2008;51:6034-43.

44. Hendrikse NH, de Vries EG, Eriks-Fluks L, van der Graaf WT, Hospers GA, Willemsen AT, et al. A new in vivo method to study P-glycoprotein transport in tumors and the blood-brain barrier. Cancer Res. 1999;59:2411-6.

45. Syvanen S, Blomquist G, Sprycha M, Hoglund AU, Roman M, Eriksson O, et al. Duration and degree of cyclosporin induced P-glycoprotein inhibition in the rat blood-brain barrier can be studied with PET. Neuroimage. 2006;32:1134-41.

46. Sasongko L, Link JM, Muzi M, Mankoff DA, Yang X, Collier AC, et al. Imaging P-glycoprotein transport activity at the human blood-brain barrier with positron emission tomography. Clin Pharmacol Ther. 2005;77:503-14.

47. Muzi M, Mankoff DA, Link JM, Shoner S, Collier AC, Sasongko L, et al. Imaging of Cyclosporine Inhibition of P-Glycoprotein Activity Using 11C-Verapamil in the Brain: Studies of Healthy Humans. J Nucl Med. 2009;50:1267-75.

48. Liow JS, Kreisl W, Zoghbi SS, Lazarova N, Seneca N, Gladding RL, et al. P-glycoprotein function at the blood-brain barrier imaged using 11C-N-desmethyl-loperamide in monkeys. J Nucl Med. 2009;50:108-15.

49. Seneca N, Zoghbi SS, Liow JS, Kreisl W, Herscovitch P, Jenko K, et al. Human brain imaging and radiation dosimetry of 11C-N-desmethyl-loperamide, a PET radiotracer to measure the function of P-glycoprotein. J Nucl Med. 2009;50:807-13.

2

50. Mima T, Toyonaga S, Mori K, Taniguchi T, Ogawa Y. Early decrease of P-glycoprotein in the endothelium of the rat brain capillaries after moderate dose of irradiation. Neurol Res. 1999;21:209-15.

51. Bart J, Nagengast WB, Coppes RP, Wegman TD, van der Graaf WT, Groen HJ, et al. Irradiation of rat brain reduces P-glycoprotein expression and function. Br J Cancer. 2007;97:322-6.

52. Marchetti S, Mazzanti R, Beijnen JH, Schellens JH. Concise review: Clinical relevance of drug drug and herb drug interactions mediated by the ABC transporter ABCB1 (MDR1, P-glycoprotein). Oncologist. 2007;12:927-41.

53. Choo EF, Kurnik D, Muszkat M, Ohkubo T, Shay SD, Higginbotham JN, et al. Differential in vivo sensitivity to inhibition of P-glycoprotein located in lymphocytes, testes, and the blood-brain barrier. J Pharmacol Exp Ther. 2006;317:1012-8.

54. Kortekaas R, Leenders KL, van Oostrom JC, Vaalburg W, Bart J, Willemsen AT, et al. Blood-brain barrier dysfunction in parkinsonian midbrain in vivo. Ann Neurol. 2005;57:176-9.

55. Bartels AL, van Berckel BN, Lubberink M, Luurtsema G, Lammertsma AA, Leenders KL. Blood-brain barrier P-glycoprotein function is not impaired in early Parkinson's disease. Parkinsonism Relat Disord. 2008;14:505-8.

56. Bartels AL, Willemsen AT, Kortekaas R, de Jong BM, de Vries R, de Klerk O, et al. Decreased blood-brain barrier P-glycoprotein function in the progression of Parkinson's disease, PSP and MSA. J Neural Transm. 2008;115:1001-9.

57. Oostendorp RL, Beijnen JH, Schellens JH. The biological and clinical role of drug transporters at the intestinal barrier. Cancer Treat Rev. 2009;35:137-47.

58. Schinkel AH, Jonker JW. Mammalian drug efflux transporters of the ATP binding cassette (ABC) family: an overview. Adv Drug Deliv Rev. 2003;55:3-29.

59. Ambudkar SV, Dey S, Hrycyna CA, Ramachandra M, Pastan I, Gottesman MM. Biochemical, cellular, and pharmacological aspects of the multidrug transporter. Annu Rev Pharmacol Toxicol. 1999;39:361-98.

60. Meerum Terwogt JM, Malingre MM, Beijnen JH, ten Bokkel Huinink WW, Rosing H, Koopman FJ, et al. Coadministration of oral cyclosporin A enables oral therapy with paclitaxel. Clin Cancer Res. 1999;5:3379-84.

61. Malingre MM, Richel DJ, Beijnen JH, Rosing H, Koopman FJ, Ten Bokkel Huinink WW, et al. Coadministration of cyclosporine strongly enhances the oral bioavailability of docetaxel. J Clin Oncol. 2001;19:1160-6.

62. Kruijtzer CM, Beijnen JH, Rosing H, ten Bokkel Huinink WW, Schot M, Jewell RC, et al. Increased oral bioavailability of topotecan in combination with the breast cancer resistance protein and P-glycoprotein inhibitor GF120918. J Clin Oncol. 2002;20:2943-50.

63. Kuppens IE, Witteveen EO, Jewell RC, Radema SA, Paul EM, Mangum SG, et al. A phase I, randomized, open-label, parallel-cohort, dose-finding study of elacridar (GF120918) and oral topotecan in cancer patients. Clin Cancer Res. 2007;13:3276-85.

64. Slamon DJ, Leyland-Jones B, Shak S, Fuchs H, Paton V, Bajamonde A, et al. Use of chemotherapy plus a monoclonal antibody against HER2 for metastatic breast cancer that overexpresses HER2. N Engl J Med. 2001;344:783-92.

65. Marty M, Cognetti F, Maraninchi D, Snyder R, Mauriac L, Tubiana-Hulin M, et al. Randomized phase II trial of the efficacy and safety of trastuzumab combined with docetaxel in patients with human epidermal growth factor receptor 2-positive metastatic breast cancer administered as first-line treatment: the M77001 study group. J Clin Oncol. 2005;23:4265-74.

66. Miller K, Wang M, Gralow J, Dickler M, Cobleigh M, Perez EA, et al. Paclitaxel plus bevacizumab versus paclitaxel alone for metastatic breast cancer. N Engl J Med. 2007;357:2666-76.

67. Miles D, A. Chan, G. Romieu, L. Y. Dirix, J. Cortes, X. Pivot, et al. Randomized, double-blind, placebo-controlled, phase III study of bevacizumab with docetaxel or docetaxel with placebo as first-line therapy for patients with locally recurrent or metastatic breast cancer (mBC): AVADO. J Clin Oncol. 2008;26:abstract LBA1011.

68.   Gross ME, Shazer RL, Agus DB. Targeting the HER-kinase axis in cancer. Semin Oncol. 2004;31:9-20.

69.   Moasser MM. The oncogene HER2: its signaling and transforming functions and its role in human cancer pathogenesis. Oncogene. 2007;26:6469-87.

70.   Bang Y, Chung H, Xu J, Lordick F, Sawaki A, Lipatov O, et al. Pathological features of advanced gastric cancer (GC): Relationship to human epidermal growth factor receptor 2 (HER2) positivity in the global screening programme of the ToGA trial. J Clin Oncol. 2009;27:abstract 4556

71.   Van Cutsem E, Kang Y, Chung H, Shen L, Sawaki A, Lordick F, et al. Efficacy results from the ToGA trial: A phase III study of trastuzumab added to standard chemotherapy (CT) in first-line human epidermal growth factor receptor 2 (HER2)-positive advanced gastric cancer (GC). J Clin Oncol. 2009;27:abstract LBA4509.

72.   Zidan J, Dashkovsky I, Stayerman C, Basher W, Cozacov C, Hadary A. Comparison of HER-2 overexpression in primary breast cancer and metastatic sites and its effect on biological targeting therapy of metastatic disease. Br J Cancer. 2005;93:552-6.

73.   Dijkers EC, de Vries EG, Kosterink JG, Brouwers AH, Lub-de Hooge MN. Immunoscintigraphy as potential tool in the clinical evaluation of HER2/neu targeted therapy. Curr Pharm Des. 2008;14:3348-62.

74.   Lub-de Hooge MN, Kosterink JG, Perik PJ, Nijnuis H, Tran L, Bart J, et al. Preclinical characterisation of 111In-DTPA-trastuzumab. Br J Pharmacol. 2004;143:99-106.

75.   Perik PJ, Lub-De Hooge MN, Gietema JA, van der Graaf WT, de Korte MA, Jonkman S, et al. Indium-111-labeled trastuzumab scintigraphy in patients with human epidermal growth factor receptor 2-positive metastatic breast cancer. J Clin Oncol. 2006;24:2276-82.

76.   Dijkers EC, Kosterink JG, Rademaker AP, Perk LR, van Dongen GA, Bart J, et al. Development and characterization of clinical-grade 89Zr-trastuzumab for HER2/neu immunoPET imaging. J Nucl Med. 2009;50:974-81.

77.   Dijkers EC, Oude Munnink TH, Kosterink JG, Brouwers AH, Jager PJ, de Jong JR, et al. HER2 PET imaging with 89Zr-trastuzumab in metastatic breast cancer patients. Clin Pharmacol Ther. In press.

78.   Neckers L. Heat shock protein 90: the cancer chaperone. J Biosci. 2007;32:517-30.

79.   Eccles SA, Massey A, Raynaud FI, Sharp SY, Box G, Valenti M, et al. NVP-AUY922: a novel heat shock protein 90 inhibitor active against xenograft tumor growth, angiogenesis, and metastasis. Cancer Res. 2008;68:2850-60.

80.   Jensen MR, Schoepfer J, Radimerski T, Massey A, Guy CT, Brueggen J, et al. NVP-AUY922: a small molecule HSP90 inhibitor with potent antitumor activity in preclinical breast cancer models. Breast Cancer Res. 2008;10:R33.

81.   Solit DB, Zheng FF, Drobnjak M, Munster PN, Higgins B, Verbel D, et al. 17-Allylamino-17-demethoxygeldanamycin induces the degradation of androgen receptor and HER-2/neu and inhibits the growth of prostate cancer xenografts. Clin Cancer Res. 2002;8:986-93.

82.   Zsebik B, Citri A, Isola J, Yarden Y, Szollosi J, Vereb G. Hsp90 inhibitor 17-AAG reduces ErbB2 levels and inhibits proliferation of the trastuzumab resistant breast tumor cell line JIMT-1. Immunol Lett. 2006;104:146-55.

83.   Smith-Jones PM, Solit DB, Akhurst T, Afroze F, Rosen N, Larson SM. Imaging the pharmacodynamics of HER2 degradation in response to Hsp90 inhibitors. Nat Biotechnol. 2004;22:701-6.

84.   Smith-Jones PM, Solit D, Afroze F, Rosen N, Larson SM. Early tumor response to Hsp90 therapy using HER2 PET: comparison with 18F-FDG PET. J Nucl Med. 2006;47:793-6.

85.   Niu G, Li Z, Cao Q, Chen X. Monitoring therapeutic response of human ovarian cancer to 17-DMAG by noninvasive PET imaging with (64)Cu-DOTA-trastuzumab. Eur J Nucl Med Mol Imaging. 2009;36:1510-9.

86.   Oude Munnink TH, Korte MA, Nagengast WB, Timmer-Bosscha H, Schroder CP, Jong JR, et al. (89)Zr-trastuzumab PET visualises HER2 downregulation by the HSP90 inhibitor NVP-AUY922 in a human tumour xenograft. Eur J Cancer. 2010;46:678-84.

87. Nahta R, Yu D, Hung MC, Hortobagyi GN, Esteva FJ. Mechanisms of disease: understanding resistance to HER2-targeted therapy in human breast cancer. Nat Clin Pract Oncol. 2006;3:269-80.

88. Comerford KM, Wallace TJ, Karhausen J, Louis NA, Montalto MC, Colgan SP. Hypoxia-inducible factor-1-dependent regulation of the multidrug resistance (MDR1) gene. Cancer Res. 2002;62:3387-94.

89. Liu L, Ning X, Sun L, Zhang H, Shi Y, Guo C, et al. Hypoxia-inducible factor-1 alpha contributes to hypoxia-induced chemoresistance in gastric cancer. Cancer Sci. 2008;99:121-8.

90. Lang SA, Klein D, Moser C, Gaumann A, Glockzin G, Dahlke MH, et al. Inhibition of heat shock protein 90 impairs epidermal growth factor-mediated signaling in gastric cancer cells and reduces tumor growth and vascularization in vivo. Mol Cancer Ther. 2007;6:1123-32.

91. Lang SA, Moser C, Gaumann A, Klein D, Glockzin G, Popp FC, et al. Targeting heat shock protein 90 in pancreatic cancer impairs insulin-like growth factor-I receptor signaling, disrupts an interleukin-6/signal-transducer and activator of transcription 3/hypoxia-inducible factor-1alpha autocrine loop, and reduces orthotopic tumor growth. Clin Cancer Res. 2007;13:6459-68.

92. Jiang BH, Liu LZ. Role of mTOR in anticancer drug resistance: perspectives for improved drug treatment. Drug Resist Updat. 2008;11:63-76.

93. Lee JT, Jr., Steelman LS, McCubrey JA. Phosphatidylinositol 3'-kinase activation leads to multidrug resistance protein-1 expression and subsequent chemoresistance in advanced prostate cancer cells. Cancer Res. 2004;64:8397-404.

94. du Manoir JM, Francia G, Man S, Mossoba M, Medin JA, Viloria-Petit A, et al. Strategies for delaying or treating in vivo acquired resistance to trastuzumab in human breast cancer xenografts. Clin Cancer Res. 2006;12:904-16.

95. Collingridge DR, Carroll VA, Glaser M, Aboagye EO, Osman S, Hutchinson OC, et al. The development of [(124)I] iodinated-VG76e: a novel tracer for imaging vascular endothelial growth factor in vivo using positron emission tomography. Cancer Res. 2002;62:5912-9.

96. Jayson GC, Zweit J, Jackson A, Mulatero C, Julyan P, Ranson M, et al. Molecular imaging and biological evaluation of HuMV833 anti-VEGF antibody: implications for trial design of antiangiogenic antibodies. J Natl Cancer Inst. 2002;94:1484-93.

97. Nagengast WB, de Vries EG, Hospers GA, Mulder NH, de Jong JR, Hollema H, et al. In vivo VEGF imaging with radiolabeled bevacizumab in a human ovarian tumor xenograft. J Nucl Med. 2007;48:1313-9.

98. Nagengast W, De Vries E, Warnders F-J, Hospers G, Mulder N, de Jong J, et al. In vivo VEGF imaging with an anti-VEGF Fab-fragment in a human ovarian tumor xenograft model using MicroPET and MicroCT. AACR meeting abstracts. 2008;# 3161.

99. Nagengast WB, Lub-de Hooge MN, Gietema JA, Oosting SF, F W, de Korte MA, et al. 89Zr-ranibizumab VEGF microPET imaging during sunitinib treatment visualizes changes with low tracer uptake in the center of the tumor and high uptake at the rim with a rebound tumor uptake after end of treatment. AACR meeting abstracts. 2009;# 5014.

100. Nagengast WB, Lub-de Hooge MN, Hospers GA, Brouwers AH, Hoekstra HJ, Elsinga PH, et al. Towards clinical VEGF imaging using the anti-VEGF antibody bevacizumab and Fab-fragment ranibizumab. J Clin Oncol. 2008;26:abstract 3547.

101. Scheer MG, Stollman TH, Boerman OC, Verrijp K, Sweep FC, Leenders WP, et al. Imaging liver metastases of colorectal cancer patients with radiolabelled bevacizumab: Lack of correlation with VEGF-A expression. Eur J Cancer. 2008;44:1835-40.

102. Kenny LM, Coombes RC, Oulie I, Contractor KB, Miller M, Spinks TJ, et al. Phase I trial of the positron-emitting Arg-Gly-Asp (RGD) peptide radioligand 18F-AH111585 in breast cancer patients. J Nucl Med. 2008;49:879-86.

2

103. Beer AJ, Niemeyer M, Carlsen J, Sarbia M, Nahrig J, Watzlowik P, et al. Patterns of alphavbeta3 expression in primary and metastatic human breast cancer as shown by 18F-Galacto-RGD PET. J Nucl Med. 2008;49:255-9.

104. Oude Munnink TH, Nagengast WB, Brouwers AH, Schroder CP, Hospers GA, Lub-de Hooge MN, et al. Molecular imaging of breast cancer. The Breast. 2009; suppl 3:S66-73.

105. Cai W, Niu G, Chen X. Multimodality imaging of the HER-kinase axis in cancer. Eur J Nucl Med Mol Imaging. 2008;35:186-208.

106. Massague J. TGFbeta in Cancer. Cell. 2008;134:215-30.

107. Hartog H, Wesseling J, Boezen HM, van der Graaf WT. The insulin-like growth factor 1 receptor in cancer: old focus, new future. Eur J Cancer. 2007;43:1895-904.

108. Jin Q, Esteva FJ. Cross-talk between the ErbB/HER family and the type I insulin-like growth factor receptor signaling pathway in breast cancer. J Mammary Gland Biol Neoplasia. 2008;13:485-98.

109. Law JH, Habibi G, Hu K, Masoudi H, Wang MY, Stratford AL, et al. Phosphorylated insulin-like growth factor-i/insulin receptor is present in all breast cancer subtypes and is related to poor survival. Cancer Res. 2008;68:10238-46.

110. Cornelissen B, McLarty K, Kersemans V, Reilly RM. The level of insulin growth factor-1 receptor expression is directly correlated with the tumor uptake of (111)In-IGF-1(E3R) in vivo and the clonogenic survival of breast cancer cells exposed in vitro to trastuzumab (Herceptin). Nucl Med Biol. 2008;35:645-53.

111. Karp DD, Paz-Ares LG, Novello S, Haluska P, Garland L, Cardenal F, et al. Phase II study of the anti-insulin-like growth factor type 1 receptor antibody CP-751,871 in combination with paclitaxel and carboplatin in previously untreated, locally advanced, or metastatic non-small-cell lung cancer. J Clin Oncol. 2009;27:2516-22.

112. Ge J, Chen Z, Wu S, Chen J, Li X, Li J, et al. Expression levels of insulin-like growth factor-1 and multidrug resistance-associated protein-1 indicate poor prognosis in patients with gastric cancer. Digestion. 2009;80:148-58.

CHAPTER 3

ImmunoPET and biodistribution with human epidermal growth factor receptor 3 targeting antibody [89]Zr-GE-huMAb-HER3

Anton G.T. Terwisscha van Scheltinga[1,2], Marjolijn N. Lub-de Hooge[2,3], Keelara Abiraj[4], Carolien P. Schröder[1], Linda Pot[1], Birgit Bossenmaier[5], Marlene Pickl[5], Thomas Friess[5], Jos G.W. Kosterink[2], Elisabeth G.E. de Vries[1]

Preliminary report

[1]Department of Medical Oncology, [2]Department of Hospital and Clinical Pharmacy, [3]Department of Nuclear Medicine and Molecular Imaging, University of Groningen, University Medical Center Groningen, Groningen, The Netherlands. [4]F. Hoffmann-La Roche AG, pRED, Pharma Research & Early Development, Translational Research Sciences, Basel, Switzerland. [5]Roche Diagnostics GmbH, pRED, Pharma Research & Early Development, Penzberg, Germany.

ABSTRACT

The humanized monoclonal antibody with high affinity for the human epidermal growth factor receptor (HER) 3, GE-huMAb-HER3, is a glycoengineered, IgG1 class antibody. By labeling GE-huMAb-HER3 with zirconium-89 ([89]Zr) we aimed to visualize *in vivo* HER3 expression and study the biodistribution of this antibody in human tumor bearing mice.

Methods:
Biodistribution of [89]Zr-GE-huMAb-HER3 was studied in subcutaneously xenografted FaDu tumor cells (HER3 positive). Dose-dependency of [89]Zr-GE-huMAb-HER3 organ distribution and specific tumor uptake was assessed by administering doses ranging from 0.05 to 10 mg/kg GE-huMAb-HER3 to SCID/Beige mice. Biodistribution was analyzed at 24 and 144 h after injection. MicroPET imaging was performed at 1, 3 and 6 days after injection of 1.0 mg/kg [89]Zr-GE-huMAb-HER3 in the FaDu, H441, QG-56 and Calu-1 xenografts with varying HER3 expression.

Results:
Biodistribution analyses showed a dose- and time-dependent [89]Zr-GE-huMAb-HER3 tumor uptake in subcutaneous FaDu tumors. The highest tumor uptake of [89]Zr-GE-huMAb-HER3 was observed in the 0.05 mg/kg dose group with 27.5 %ID/g at 144 h after tracer injection. MicroPET imaging revealed specific tumor uptake of [89]Zr-GE-huMAb-HER3 in FaDu and H441 models with an increase in tumor uptake over time. Biodistribution data was consistent with the microPET findings, showing *ex vivo* tumor uptake of [89]Zr-GE-huMAb-HER3 of 13.9, 19.0, 9.2 and 7.6 %ID/g in FaDu, H441, QG56 and Calu-1 xenografts respectively, which correlated with HER3 expression levels.

Conclusion:
[89]Zr-GE-huMAb-HER3 specifically accumulates in HER3 expressing tumors. PET imaging with this tracer provides real-time non-invasive information GE-huMAb-HER3 distribution and tumor accumulation and about tumor HER3 expression levels.

INTRODUCTION

The human epidermal growth factor receptor (HER) transmembrane receptor tyrosine kinase family consists of four members: epidermal growth factor receptor (EGFR), HER2, HER3 and HER4. Members of this family play a critical role in tumor cell survival, proliferation, maturation, metastasis and angiogenesis via diverse cellular pathways. (1)

A number of targeted therapies consisting of antibodies and tyrosine kinase inhibitors against the HER family members EGFR and HER2 are currently used in daily clinical practice. The EGFR targeting monoclonal antibodies cetuximab and panitumumab are used in KRAS wild-type metastatic colorectal cancer and cetuximab in patients with squamous cell cancer of the head and neck. (2) Trastuzumab, the monoclonal antibody targeting HER2, is administered to patients with HER2 positive breast cancer in the adjuvant and metastatic setting and for metastatic gastric cancer. (3-4) Tyrosine kinase inhibtors (TKI) targeting EGFR and HER2 are used in the clinic in respectively lung and breast cancer. (2-3) Unfortunately many patients do not respond on EGFR and HER2 targeted therapies or develop resistance during treatment. (2, 5) Therefore, several pharmaceutical companies are working on the development of different or improved EGFR and HER2 targeting agents. (2-3, 6) Moreover, combination therapies with other growth factor receptor targeting drugs are searched for. Based on novel insights, an antibody against HER3 is an interesting option. (7)

HER family members are inactive in monomers, but can be activated by homo- or heterodimerization after ligand binding. (3) HER3 is the only member in the HER family lacking intrinsic tyrosine kinase activity and therefore has been underestimated for its role in cancer until recently. (7) It can only be activated after the formation of heterodimers, which are the most active signaling complexes with HER1/HER3 and HER2/HER3 heterodimers as the most potent dimers in this family. (7) Given this prominent role of HER3 in tumor growth and maintenance and the fact that it is overexpressed in many solid tumors makes it is an interesting target to inhibit HER family signaling. (8)

One example of such a drug is the humanized monoclonal antibody with high affinity for HER3, GE-huMAb-HER3, which is a glycoengineered IgG1 class antibody. GE-huMAb-HER3 binds to the extracellular domain of HER3 (domain I) with high affinity. GE-huMAb-HER3 inhibits HER3 and AKT phosphorylation and induces HER3 internalization in tumor cells. (9) Moreover glycoengineering translates into enhanced *in vitro* ADCC activity of GE-huMAb-HER3 via FcγRIIIA binding on human immune effector cells. (10) GE-huMAb-HER3 is currently in phase 1 clinical testing. For monoclonal antibodies in cancer patients in the absence of or with only limited toxicity it can be difficult to determine the right dose for the individual patient needed for antitumor efficacy. Molecular imaging might support decision making during clinical development and clinical practice. It has also potential as a tool for patient selection for therapy, by showing the presence of the target and uptake of the drug before initiating therapy.

Molecular imaging can visualize the biodistribution of monoclonal antibodies by using these drugs as a tracer after labeling it with zirconium-89 ([89]Zr; $t_{1/2}$ = 78.4 h). (11) We developed the PET radiopharmaceuticals [89]Zr labeled bevacizumab to image vascular endothelial growth factor (VEGF) and [89]Zr-trastuzumab to image HER2 in tumors and tested them successfully preclinical and clinically. (12-15)

In order to visualize *in vivo* HER3 expression and study the biodistribution of this antibody we performed the *in vivo* evaluation of [89]Zr-GE-huMAb-HER3 in human tumor bearing mice.

MATERIALS AND METHODS

Cell lines

Cell lines with various HER3 expression were used. The human head and neck squamous cell carcinoma (HNSCC) FaDu cell line and human non-small cell lung cancer (NSCLC) cell line H441 are high expressing HER3, QG-56, a human NSCLC cell line with medium and Calu-1 human NSCLC cell line without HER3 expression were used. These cell lines were chosen based on HER3 expression and antitumor effect of GE-huMAb-HER3 treatment. Responsiveness of the subcutaneous (sc) xenografted tumor cell lines in mice to GE-huMAb-HER3 treatment was determined by tumor growth inhibition studies. (9) FaDu and QG-56 are both responsive *in vivo* to treatment with GE-huMAb-HER3 and H441 and Calu-1 are non-responder cell lines to treatment with GE-huMAb-HER3. FaDu, QG-56 and H441 cells were cultured in DMEM (Invitrogen), supplemented with 10% fetal calf serum (FCS) (Bodinco BV) and, 2 mM L-glutamine (Invitrogen), Calu-1 in RPMI 1640 (Invitrogen) supplemented with 10% FCS and 2 mM L-glutamine. All cell lines were grown at 37°C in a fully humidified atmosphere containing 5% CO_2.

Synthesis and quality control of conjugated and radiolabeled [89]Zr-GE-huMAb-HER3

GE-huMAb-HER3 (2.7 mg/mL; Roche) was allowed to react with a 5-fold molar excess of a tetrafluorophenol-N-succinyldesferal-Fe active ester (TFP-N-SucDf-Fe; VU University Medical Center) as described earlier. (16) The conjugate was radiolabeled with clinical-grade [89]Zr-oxalate (IBA Molecular) to obtain a radiochemical purity of at least 95%. Quality control was performed as described previously. (12-13)

Immunoreactive fraction of the radiolabeled compound was determined by a competition assay performed on HER3 extracellular domain (ECD; Roche) coated well-plates. HER3 ECD was diluted in sodium phosphate buffer (PBS; 140 mmol/L NaCl, 9 mmol/L Na_2HPO_4, 1.3 mmol/L NaH_2PO_4; UMCG) resulting in a concentration of 5 µg/mL. The solution was adjusted to pH 9.2–9.5 with 50 mmol/L Na_2CO_3 and 50 µL was added to the wells, incubated overnight at 4°C, and then blocked with 1% human serum albumin (HSA; Sanquin) in PBS. After blocking, the plates were washed with 0.1% polysorbate 80 (Sigma-Aldrich) in PBS. [89]Zr-GE-huMAb-HER3 and GE-huMAb-HER3 were mixed and diluted in PBS to result in a fixed concentration of 500 ng/mL

(3.33 nM) ^{89}Zr-GE-huMAb-HER3 and varying concentrations of unlabeled GE-huMAb-HER3, ranging from 3.33 pM to 3.33 µM. These samples were added to the wells, and incubated for 2 h. Subsequently, the samples were collected from the wells in 2 wash steps. Both the ^{89}Zr-GE-huMAb-HER3 bound to the HER3 ECD-coated wells and the collected samples containing unbound ^{89}Zr-GE-huMAb-HER3 were measured by a calibrated well-type γ-counter. The percentage of HER3 binding was calculated as the fraction of radioactivity bound to HER3 ECD-coated wells divided by the total amount of radioactivity added. At equal doses of labeled and unlabeled GE-huMAb-HER3, a binding of 35.5% of radiolabeled GE-huMAb-HER3 was found, which indicates an immunoreactivity of $70.9 \pm 5.8\%$.

IgG conjugation and indium-111 labeling

Human IgG served as an aspecific control in the experiments. Human IgG (Sanquin) conjugation with the bifunctional conjugating agent 2-(4-isothiocyanatobenzyl)-diethylenetriaminepentaacetic acid (p-SCN-Bn-DTPA, Macrocyclics) was performed as described by Ruegg et al. (17). Conjugated human IgG was radiolabeled with indium-111 (^{111}In) chloride (Covidien).

Animal experiments

For sc tumor inoculation, cells were harvested by trypsinization and suspended in PBS. In vivo imaging and ex vivo experiments were conducted using female Fox Chase SCID Beige Mouse (CB17.Cg-Prkdc^{scid}Lyst ^{bg}/Crl) obtained from Charles River (Germany). Mice were sc injected with 5 x 10^6 FaDu, 4 x 10^6 QG-56, 4 x 10^6 H441 or 5 x 10^6 Calu-1 cells in 0.1 mL in PBS. Tumor growth was followed with caliper measurements. The tracer injection was performed for FaDu 2 weeks after tumor cell inoculation, for QG-56 and H441 3 weeks after inoculation and for Calu-1 10 weeks after inoculation.

A dose escalation biodistribution study with ^{89}Zr-GE-huMAb-HER3 (1 MBq) was performed in sc FaDu tumor bearing mice to evaluate dose dependent tumor uptake of the antibody. Five dose groups of 0.05, 0.3, 1.0, 3.0 and 10.0 mg/kg antibody were included. Each dose was administered to 2 groups (n = 4-6) of animals via intravenous (iv) tail vein injection. In case of doses above 0.3 mg/kg, cold antibody (GE-huMAb-HER3) was added to reach the desired antibody dose. Biodistribution analyses were performed at 24 and 144 h after injection.

To assess HER3 specific uptake in different tumor models with differential HER3 expression and to assess the time dependent organ distribution of ^{89}Zr-GE-huMAb-HER3, microPET imaging was performed in sc xenografted mice (n = 4-6). Mice bearing FaDu, H441, QG-56 and Calu-1 tumors, were scanned at 1, 3 and 6 days after injection of 1.0 mg/kg ^{89}Zr-GE-huMAb-HER3 (5 MBq). After the last scan, mice were sacrificed for biodistribution analysis.

To discriminate between specific and non-specific tumor uptake and biodistribution, ^{111}In-IgG (1 MBq) was co-injected with all ^{89}Zr-GE-huMAb-HER3 administrations. A ratio between ^{89}Zr and ^{111}In tumor values was

calculated for all dose groups at 24 and 144 h after injection in the dose-escalation biodistribution study performed using the FaDu tumor model. To compare specific tumor uptake of [89]Zr-GE-huMAb-HER3 in different tumor models, tumor : blood ratios were calculated. This enabled comparison of tumor uptake with the amount of antibody present in blood which is able to bind specific or non-specifically in tumor tissue.

Animals were imaged using a microPET Focus 220 rodent scanner (CTI Siemens). After image reconstruction, *in vivo* quantification was performed with AMIDE Medical Image Data Examiner software (version 0.9.1, Stanford University). (18) The data is presented as the mean standard uptake value (SUVmean), which is calculated by dividing the mean region of interest (ROI) activity by the injected dose (corrected for decay) per gram body weight. Animals were sacrificed at the time of biodistribution, organs and tissues were excised and weighed. Samples and primed standards were counted for radioactivity in a calibrated well-type LKB-1282-Compu-gamma system (LKB Wallac) and corrected for physical decay. *Ex vivo* tissue activity is expressed as percentage of the injected dose per gram tissue (%ID/g). Half of the harvested tumors were paraffin embedded and serum and the other half of the tumors were stored in the -80 °C for further analysis. The animal experiments were approved by the animal experiments committee of the University of Groningen.

Statistical analysis

Data are presented as mean ± standard deviation (SD). Statistical analyses were performed using Mann-Whitney test (GraphPad 5.00). A P-value ≤ 0.05 was considered significant.

RESULTS

Dose-escalation biodistribution study

The dose-escalation biodistribution study in sc FaDu tumor bearing mice showed preferential HER3 driven tumor uptake of [89]Zr-GE-huMAb-HER3 as compared to ^{111}In-IgG. The highest tumor uptake was seen at the 0.05 mg/kg dose group, 144 h after injection (Fig. 1A). At 144 h after injection %ID/g tumor uptake decreased significantly with increasing doses of GE-huMAb-HER3 from 27.5 ± 3.5 %ID/g at 0.05 mg/kg to 10.1 ± 0.6 %ID/g at 10 mg/kg (P < 0.01). This pattern was also seen in the biodistribution analysis after 24 h, although to a lesser extent. In Fig. 1B tumor uptake of [89]Zr-GE-huMAb-HER3 is corrected for non-specific ^{111}In-IgG uptake. There was specific uptake of [89]Zr-GE-huMAb-HER3 in the 0.05 mg/kg dose group already at 24 h (P < 0.01), based on the ratio between [89]Zr and ^{111}In tumor values. Between 24 and 144 h after injection there was a further increase in specific uptake of [89]Zr-GE-huMAb-HER3 as illustrated by the increasing ratio between [89]Zr and ^{111}In tumor uptake. There were significant differences between [89]Zr and ^{111}In tumor uptake for all dose groups at 144 h after injection.
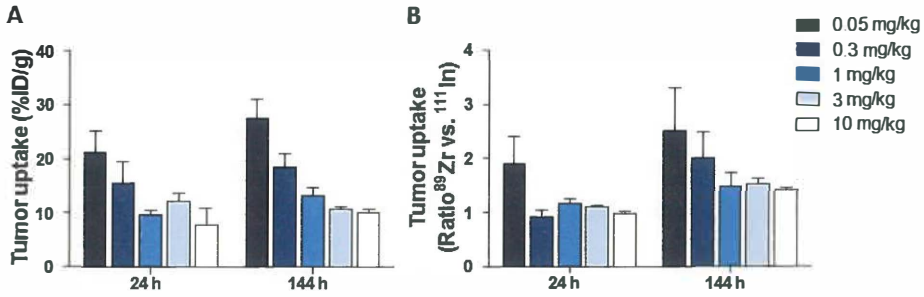
Figure 1 | Tumor uptake at 24 and 144 h after tracer injection as measured with *ex vivo* analysis showed dose and time dependent tumor uptake of 89Zr-GE-huMAb-HER3 in FaDu tumors (A). Specific tumor uptake was determined by correcting 89Zr-GE-huMAb-HER3 uptake for non-specific 111In-IgG uptake (B).
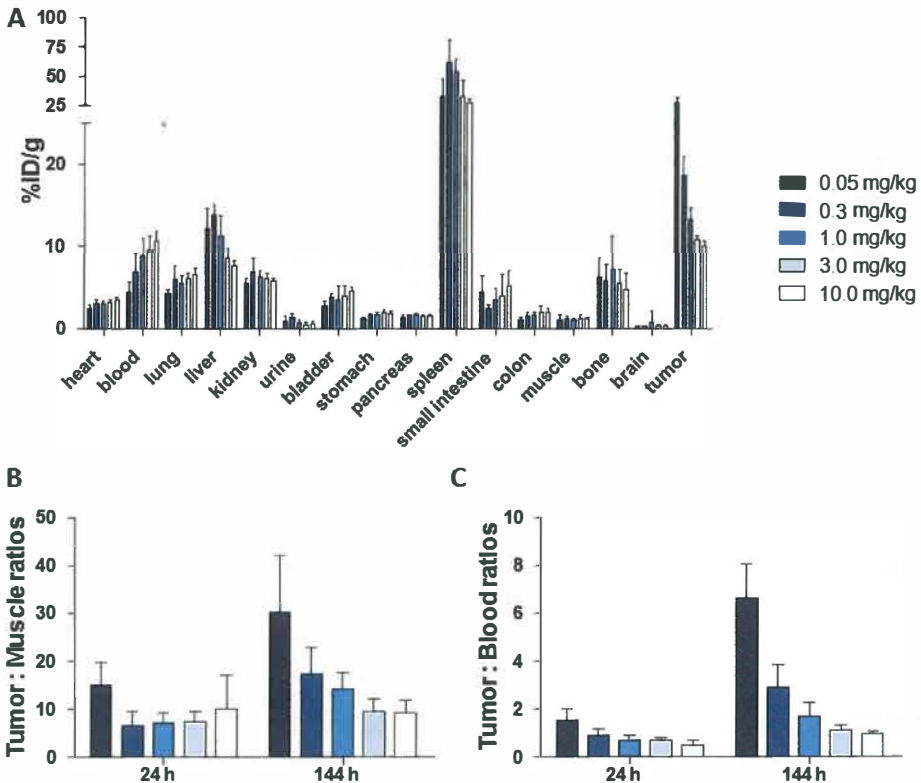
Figure 2 | Biodistribution of 89Zr-GE-huMAb-HER3 at 144 h as determined by *ex vivo* analysis (A). Tumor : muscle ratios (B) and tumor : blood ratios (C) were calculated for the different doses used in the dose-escalation biodistribution study at 24 and 144 h after tracer injection.

Biodistribution experiments with [89]Zr-GE-huMAb-HER3 revealed a normal antibody organ distribution except for the exceptionally high spleen uptake found for all doses used (Fig. 2A), which occurred already 24 h after injection. ^{111}In-IgG uptake in the spleen was also found to be high, however to a lesser extent than for [89]Zr-GE-huMAb-HER3 in all dose groups. In the 0.05 mg/kg group the tumor : blood ratio was 6.6 (Fig. 2B), the tumor : muscle ratio was 30.3 (Fig. 2C). With increasing doses both these ratios decreased at 24 and 144 h after injection displaying the dose dependent tracer distribution.

Tumor weight measurements at the end of the experiment (144 h after tracer injection) revealed a smaller tumor volume for the highest dose groups compared to the lower dose groups, indicating dose dependent tumor inhibitory drug effects. Tumor weights were 0.44 ± 0.17 g, 0.54 ± 0.14 g, 0.41 ± 0.18 g, 0.28 ± 0.17 g and 0.26 ± 0.05 g for the different doses respectively ranging from 0.05 to 10 mg/kg. The single antibody administration used in this study already influenced tumor size and thereby also tumor uptake measured of [89]Zr-GE-huMAb-HER3.
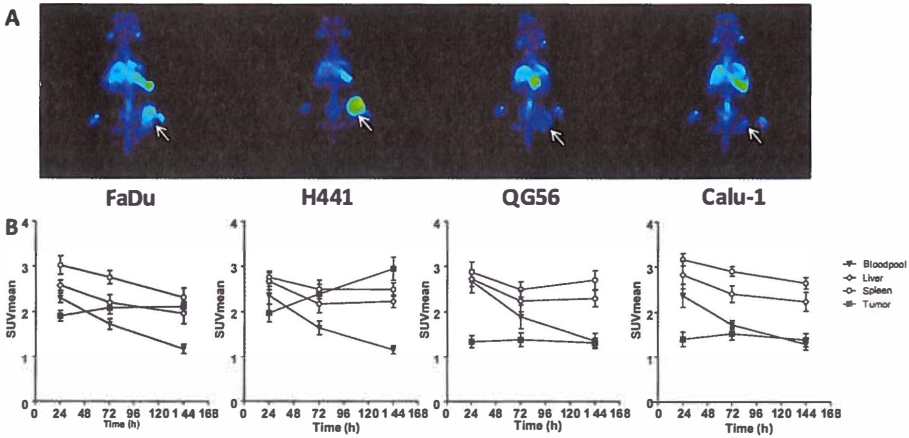
Figure 3 | [89]Zr-GE-huMAb-HER3 microPET imaging of FaDu, H441, QG56 and Calu-1 bearing mice. Maximal intensity projection images are shown for all tumor models at 144 h after tracer injection (A). MicroPET data quantification was performed for blood pool, spleen, liver and tumor uptake at 24, 72 and 144 after tracer injection in all mice (B).

MicroPET imaging in different tumor models and biodistribution

MicroPET scan analysis revealed at day 1 after injection of 1.0 mg/kg [89]Zr-GE-huMAb-HER3 high blood pool, spleen and liver activity which could be visualized in all mice bearing xenografted tumors of FaDu, H441, QG-56 and Calu-1. Quantification of PET data showed that the non-specific uptake in these organs decreased over time based on the scans performed at day 3 and 6 after injection of 1.0 mg/kg [89]Zr-GE-huMAb-HER3 (Fig. 3). Specific HER3 driven uptake was seen in FaDu and H441 tumors with increasing tumor uptake over time. QG-56 and Calu-1 tumors did show tumor uptake on microPET scans, however minimal differences in tumor uptake were seen over time post-tracer injection. An average tumor SUVmean

of 2.1, 2.9, 1.3 and 1.4 was quantified based on microPET scans on day 6 after injection in FaDu, H441, QG-56 and Calu-1 respectively (Fig. 3).

After the last scan, mice were sacrificed for biodistribution analysis. Biodistribution data were fully consistent with the microPET findings, showing *ex vivo* tumor uptake of 89Zr-GE-huMAb-HER3 of 13.9, 19.0, 9.2 and 7.6 %ID/g in FaDu, H441, QG56 and Calu-1 xenografts respectively (Fig. 4A). 111In-IgG tumor uptake in these models was 9.1 (FaDu), 16.5 (H441), 6.7 (QG56) and 8.3 (Calu-1). Tumor : blood ratios of 89Zr-GE-huMAb-HER3 compared to 111In-IgG distribution revealed significant differences in HER3 expressing tumors, indicating specific tumor uptake in these models (Fig. 4B). The HER3 negative Calu-1 did not show a significant ($p = 0.065$) difference between tumor : blood ratios of 89Zr-GE-huMAb-HER3 versus 111In-IgG indicating non-specific tumor uptake in this model.

3
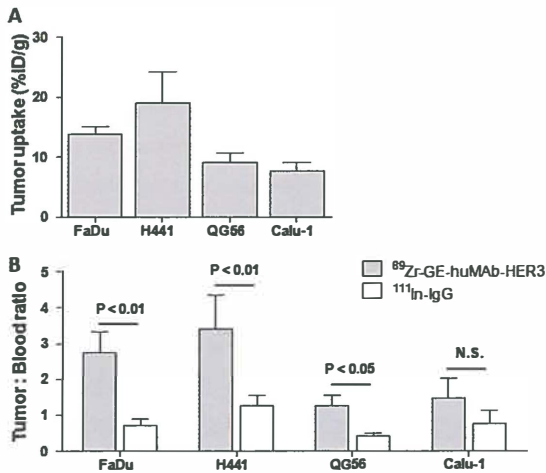
Figure 4 | *Ex vivo* tumor uptake of 89Zr-GE-huMAb-HER3 in FaDu, H441, QG56 and Calu-1 tumors (A). To compare specific tumor uptake between tumor models, tumor : blood ratios are provided for 89Zr-GE-huMAb-HER3 and 111In-IgG (B).

Tumor weight at the end of the experiment were for FaDu tumors 0.176 ± 0.077 g, H441 tumors 0.183 ± 0.060 g, QG56 tumors 0.162 ± 0.113 g and Calu-1 tumors 0.057 ± 0.043 g. *Ex vivo* tumor weights showed a correlation of 0.984 (R^2) with tumor ROIs volumes used for microPET quantification. *Ex vivo* 89Zr-GE-huMAb-HER3 tumor uptake showed a correlation of 0.812 (R^2) with tumor uptake on microPET quantification.

DISCUSSION

This study describes the *in vivo* study with an imaging probe for HER3 expression measurement. It shows specific HER3 driven tumor uptake of [89]Zr-GE-huMAb-HER3 in a dose-escalation biodistribution study at different time points. Tumor uptake of the radiolabeled antibody in preclinical xenograft models is related to HER3 expression levels.

This indicates that [89]Zr-GE-huMAb-HER3 can be used for non-invasive assessment of the HER3 expression levels in tumor lesions and provide real-time information about GE-huMAb-HER3 distribution and tumor uptake. AMG-888, another antibody targeting HER3, was labeled with cupper-64 (^{64}Cu) for PET imaging. In the human pancreatic cancer xenograft model microPET imaging showed higher tracer uptake when compared to the animals administered a blocking dose. Biodistribution studies in tumor bearing mice show uptake and retention in BxPC3 tumors at 24 and 48 hrs post injection. (19) We used the radionuclide [89]Zr for PET imaging of a HER3 targeting antibody, allowing us to image up to 144 h after tracer injection and to visualize optimal tumor targeting of the antibody. In the absence of other *in vivo* studies for HER3 it is of interest to compare our findings with results obtained with radiolabeled antibodies against the HER family members HER2 and EGFR. [89]Zr labeled trastuzumab and cetuximab both showed specific uptake in a panel xenograft tumor models. (13, 20) With radiolabeled trastuzumab, a comparative preclinical biodistribution study was performed with 100 µg [89]Zr-trastuzumab in SKOV3 (HER2 overexpressing) and GLC4 (HER2 negative), tumor uptake was respectively 33.4 and 7.1 %ID/g. (13) This tracer proved also applicable in patients with even higher [89]Zr-trastuzumab tumor to background ratios in HER2 positive lesions than in human tumor bearing animals. (13) HER2 is amplified in 15-25% of breast cancer patients. Although no amplification has been shown for HER3 in tumors, we could visualize with [89]Zr-GE-huMAb-HER3 that tracer tumor uptake is correlated with high HER3 expression levels of the tumors. In FaDu tumors a 27.5 %ID/g at 0.05 mg/kg was obtained 144 h after tracer injection, showing comparable tumor uptake as obtained with trastuzumab in a HER2 positive human ovarian cancer tumor model. [89]Zr-labeled cetuximab showed disparity between tumor uptake assessed with PET imaging and *in vivo* EGFR expression in human epidermoid, breast, glioblastoma and colorectal carcinoma tumors. (20) Therefore, the authors concluded that [89]Zr-cetuximab represents antibody uptake instead of quantification of EGFR expression levels. For ^{64}Cu labeled cetuximab and panitimumab in HNSCC xenograft models the findings were similar. (21-23) Comparison of biodistribution data between [89]Zr-GE-huMAb-HER3 and other antibodies is hampered given the mouse strain we used. In these Fox Chase SCID Beige Mice there is a disproportional high influence of spleen uptake of [89]Zr-GE-huMAb-HER3. Biodistribution experiments revealed high spleen uptake for GE-huMAb-HER3 as well as for non-specific IgG. This can probably be explained due to acting of the spleen as a "sink" for antibodies, for GE-huMAb-HER3 even more pronounced than for IgG. This is not related to specific HER3 driven uptake in the spleen, as the uptake decreased over time, on the microPET scans in various different tumor models. High spleen uptake of 82.4±15.3 %ID/g 24 h after administration of ^{111}In-labeled mesothelin targeting antibody was observed in C.B-17 SCID mice. (24) The mouse strain (SCID mice) used

for these experiments, may have affected this relatively high antibody uptake, as far lower IgG uptake in spleen is found in other strains. (12-13)

Tumor uptake of antibodies is influenced by many factors like vascular density and permeability, as well as tumor structure and extracellular matrix. We found a correlation between HER3 expression and tumor uptake, based on tumor : blood ratios. Tumor uptake is, as is to be expected, not necessarily correlated with tumor response. This is illustrated in the HER3 overexpressing H441 xenografts, which showed highest [89]Zr-GE-huMAb-HER3 uptake but were non-responsive to GE-huMAb-HER3. H441 is dependent on other pathways than those involved in HER3 signaling.

Although presence of a receptor does not preclude resistance in clinical practice, establishing the presence or absence of a growth factor receptor (mostly by means of tumor staining or molecular imaging) is clearly of tremendous importance. In breast cancer for instance, the absence of the estrogen receptor or HER2 predicts lack of anti-ER or -HER2 treatment effect (far better than presence of these receptors predicts a good effect of treatment directed at them) and this negative predictive value drives treatment decisions. (25-26) Therefore, establishing HER3 presence (for instance by means of molecular imaging) may well have in impact on treatment decisions in the future.

Based on these promising preclinical results, clinical testing of [89]Zr-GE-huMAb-HER3 is warranted. In a phase 1 setting the [89]Zr-GE-huMAb-HER3 PET imaging will be included and provide insight in GE-huMAb-HER3 behavior in cancer patients. Molecular imaging can likely contribute to dose-finding of this new antibody as one of the goals will be to determine which dose is necessary to saturate the target, leading to a rational dosing scheme.

REFERENCES

1. Citri A, Yarden Y. EGF-ERBB signalling: towards the systems level. Nat Rev Mol Cell Biol. 2006;7:505-16.

2. Wheeler DL, Dunn EF, Harari PM. Understanding resistance to EGFR inhibitors-impact on future treatment strategies. Nat Rev Clin Oncol. 2010;7:493-507.

3. Baselga J, Swain SM. Novel anticancer targets: revisiting ERBB2 and discovering ERBB3. Nat Rev Cancer. 2009;9:463-75.

4. Fornaro L, Lucchesi M, Caparello C, Vasile E, Caponi S, Ginocchi L, et al. Anti-HER agents in gastric cancer: from bench to bedside. Nat Rev Gastroenterol Hepatol. 2011;8:369-83.

5. Garrett JT, Arteaga CL. Resistance to HER2-directed antibodies and tyrosine kinase inhibitors: mechanisms and clinical implications. Cancer Biol Ther. 2011;11:793-800.

6. Capelan M, Pugliano L, De Azambuja E, Bozovic I, Saini KS, Sotiriou C, et al. Pertuzumab: new hope for patients with HER2-positive breast cancer. Ann Oncol. 2012.

7. Amin DN, Campbell MR, Moasser MM. The role of HER3, the unpretentious member of the HER family, in cancer biology and cancer therapeutics. Semin Cell Dev Biol. 2010;21:944-50.

8. Campbell MR, Amin D, Moasser MM. HER3 comes of age: new insights into its functions and role in signaling, tumor biology, and cancer therapy. Clin Cancer Res. 2010;16:1373-83.

9. Bossenmaier B, Friess T, Gerdes C, Kolm I, Dimoudis N, Lifke V, et al. GE-huMab-HER3, a novel humanized, glycoengineered HER3 antibody with enhanced ADCC and superior preclinical in vitro and in vivo efficacy. Proc AACR Annual meeting 2012; abstract #3079.

10. Paz-Ares LG, Gomez-Roca C, Delord JP, Cervantes A, Markman B, Corral J, et al. Phase I pharmacokinetic and pharmacodynamic dose-escalation study of RG7160 (GA201), the first glycoengineered monoclonal antibody against the epidermal growth factor receptor, in patients with advanced solid tumors. J Clin Oncol. 2011;29:3783-90.

11. van Dongen GA, Vosjan MJ. Immuno-positron emission tomography: shedding light on clinical antibody therapy. Cancer Biother Radiopharm. 2010;25:375-85.

12. Nagengast WB, de Vries EG, Hospers GA, Mulder NH, de Jong JR, Hollema H, et al. In vivo VEGF imaging with radiolabeled bevacizumab in a human ovarian tumor xenograft. J Nucl Med. 2007;48:1313-9.

13. Dijkers EC, Kosterink JG, Rademaker AP, Perk LR, van Dongen GA, Bart J, et al. Development and characterization of clinical-grade [89]Zr-trastuzumab for HER2/neu immunoPET imaging. J Nucl Med. 2009;50:974-81.

14. Oosting SF, Nagengast WB, Oude Munnink TH, Lub- de Hooge MN, Brouwers AH, Glaudemans AWJM, et al. [89]Zr-bevacizumab PET imaging in renal cell carcinoma patients: feasibility of tumor VEGF quantification EORTC-NCI-AACR meeting abstracts 2010, #221.

15. Dijkers EC, Oude Munnink TH, Kosterink JG, Brouwers AH, Jager PL, de Jong JR, et al. Biodistribution of [89]Zr-trastuzumab and PET imaging of HER2-positive lesions in patients with metastatic breast cancer. Clin Pharmacol Ther. 2010;87:586-92.

16. Verel I, Visser GW, Boellaard R, Stigter-van Walsum M, Snow GB, van Dongen GA. [89]Zr immuno-PET: comprehensive procedures for the production of [89]Zr-labeled monoclonal antibodies. J Nucl Med. 2003;44:1271-81.

17. Ruegg CL, Anderson-Berg WT, Brechbiel MW, Mirzadeh S, Gansow OA, Strand M. Improved in vivo stability and tumor targeting of bismuth-labeled antibody. Cancer Res. 1990;50:4221-6.

18. Loening AM, Gambhir SS. AMIDE: a free software tool for multimodality medical image analysis. Mol Imaging. 2003;2:131-7.

19. Sharp TL, Glaus C, Fettig N, Hewig A, Ogbagabriel S, Freeman D, et al. Pharmacological evaluation of ^{64}Cu-DOTA-AMG888 (U3-1287) in control and tumor bearing mice using biodistribution and microPET imaging. Proc World Molecular Imaging Congresse 2011; abstract #T206.

20. Aerts HJ, Dubois L, Perk L, Vermaelen P, van Dongen GA, Wouters BG, et al. Disparity between in vivo EGFR expression and [89]Zr-labeled cetuximab uptake assessed with PET. J Nucl Med. 2009;50:123-31.

21. Niu G, Li Z, Xie J, Le QT, Chen X. PET of EGFR antibody distribution in head and neck squamous cell carcinoma models. J Nucl Med. 2009;50:1116-23.

22. Ping Li W, Meyer LA, Capretto DA, Sherman CD, Anderson CJ. Receptor-binding, biodistribution, and metabolism studies of ^{64}Cu-DOTA-cetuximab, a PET-imaging agent for epidermal growth-factor receptor-positive tumors. Cancer Biother Radiopharm. 2008;23:158-71.

23. Cai W, Chen K, He L, Cao Q, Koong A, Chen X. Quantitative PET of EGFR expression in xenograft-bearing mice using ^{64}Cu-labeled cetuximab, a chimeric anti-EGFR monoclonal antibody. Eur J Nucl Med Mol Imaging. 2007;34:850-8.

24. Misri R, Saatchi K, Ng SS, Kumar U, Hafeli UO. Evaluation of (111)In labeled antibodies for SPECT imaging of mesothelin expressing tumors. Nucl Med Biol. 2011;38:885-96.

25. Early Breast Cancer Trialists' Collaborative Group (EBCTCG). Effects of chemotherapy and hormonal therapy for early breast cancer on recurrence and 15-year survival: an overview of the randomised trials. Lancet. 2005;365:1687-717.

26. Seidman AD, Berry D, Cirrincione C, Harris L, Muss H, Marcom PK, et al. Randomized phase III trial of weekly compared with every-3-weeks paclitaxel for metastatic breast cancer, with trastuzumab for all HER-2 overexpressors and random assignment to trastuzumab or not in HER-2 nonoverexpressors: final results of Cancer and Leukemia Group B protocol 9840. J Clin Oncol. 2008;26:1642-9.

3

CHAPTER 4

In vivo visualization of c-Met tumor expression and Anticalin biodistribution with the c-Met specific Anticalin [89]Zr-PRS-110 PET tracer

Anton G.T. Terwisscha van Scheltinga[1,2], Marjolijn N. Lub-de Hooge[2,3], Marlon J. Hinner[4], Remy B. Verheijen[1], Andrea Allersdorfer[4], Martin Hülsmeyer[4], Wouter B. Nagengast[1], Carolien P. Schröder[1], Jos G.W. Kosterink[2], Elisabeth G.E. de Vries[1], Laurent Audoly[4], Shane A. Olwill[4]

[1]Department of Medical Oncology, [2]Department of Hospital and Clinical Pharmacy, [3]Department of Nuclear Medicine and Molecular Imaging, University of Groningen, University Medical Center Groningen, Groningen, The Netherlands. Pieris-AG[4], Freising-Weihenstephan, Germany.

ABSTRACT

Anticalins are a novel class of biopharmaceuticals, displaying highly desirable attributes as imaging agents. The Anticalin PRS-110 was rationally engineered to target the oncogene c-Met with high affinity and specificity. The aim of this study was to visualize c-Met expression and analyze biodistribution of ^{89}Zr-PRS-110 in human tumor bearing mice.

Methods:

Zirconium-89 (^{89}Zr) labeled PRS-110 was generated. For biodistribution studies (96 h after injection of tracer) doses of 10-500 µg ^{89}Zr-PRS-110 were injected into Balb/c mice bearing high c-Met expressing H441 non-small cell lung cancer xenografts. Further characterization with PET imaging was performed at 6, 24, 48 and 96 h after injection of 50 µg ^{89}Zr-PRS-110 to mice bearing H441, primary glioblastoma U87-MG (intermediate c-Met) or ovarian cancer A2780 (low c-Met) xenografts. Drug distribution was also analyzed *ex vivo* using fluorescently labeled PRS-110 .

Results:

Biodistribution analyses showed a PRS-110 dose-dependent ^{89}Zr-PRS-110 H441-tumor uptake, with the highest fractional tumor uptake at 10 µg PRS-110. MicroPET imaging supported by biodistribution data revealed specific tumor uptake of ^{89}Zr-PRS-110 in the c-Met expressing H441 and U87-MG tumors while the c-Met negative A2780 tumor model showed a lower uptake similar to a non-c-Met binder Anticalin control. Tumor uptake increased up to 24 h after tracer injection and remained high, while uptake in other organs decreased over time. *Ex vivo* fluorescence revealed intracellular presence of PRS-110.

Conclusion:

^{89}Zr-PRS-110 specifically accumulates in c-Met expressing tumors in a receptor density-dependent manner. PET imaging provides real-time non-invasive information about PRS-110 distribution and tumor accumulation in preclinical models.

INTRODUCTION

Mesenchymal-epithelial transition factor receptor (c-Met) is of clinical interest as a drug target as genetic and biochemical data have shown that hepatocyte growth factor (HGF) and its receptor, the tyrosine kinase c-Met, have a causal role in essential hallmarks of cancer. (1, 2) These include uncontrolled cell survival, growth, angiogenesis and metastasis. Overexpression of c-Met at the tumor cell membrane and its ligand HGF in the surrounding stroma occur in many tumor types. (1, 2)

This strong rationale for targeting the pathway has led to multiple clinical trials which are currently underway to evaluate the efficacy of c-Met targeting agents including monoclonal antibodies (against the receptor or ligand) and tyrosine kinase inhibitors. (1) Diagnostic methods that help identify a patient population likely to respond to c-Met therapy are fundamental for successful trial outcome. Patient selection for ongoing trials is largely based on evaluation of c-Met status in biopsy material using immunohistochemistry (IHC) or fluorescent in situ hybridization (FISH) at time of enrolment however the methods are not capable of informing fluctuation in expression levels over time. Allied to this shortcoming, the evaluation of c-Met involvement in secondary tumors is often hampered by lack of tissue. An imaging tool capable of providing real time data on whole body c-Met expression would aid decision making and identification of patients who will likely benefit from a c-Met targeting agent thus reducing unnecessary administration of ineffective drugs.

Anticalins are a novel class of small biologic therapeutics, based on the human lipocalin scaffold. (3) The human lipocalins are a family of small molecular weight proteins involved in binding and transporting diverse molecules (small molecules and large proteins). (3-5) The lipocalins consist of a barrel-like structure made up of 8 beta strands connected by four loop regions. Anticalins are rationally engineered to bind with exquisite selectivity and potency a single target or specific targets by introducing discreet amino acid substitutions in select areas of the lipocalin scaffold. Importantly, Anticalins retain the overall fold of lipocalins but redesigned pharmacological properties. (6) We rationally engineered PRS-110, an Anticalin with monovalent specificity for c-Met. (7, 8) PRS-110 acts as both a full antagonist of HGF-evoked c-Met signaling and also a ligand-independent inhibitor of c-Met-driven tumorigenesis. While PRS-110 is also being developed as a therapeutic it displays many highly desirable properties as an imaging agent. As 17 kDa proteins, Anticalins may have more favorable tumor uptake and penetration when compared to the much larger IgG's (ca. 150 kDa). Moreover, circulating half-life of Anticalins can be tuned to suit specific applications through half-life extension formats such as the site-directed derivatization with a polyethylene glycol (PEG) polymer chain. (7)

The therapeutic application of Anticalins was recently demonstrated in a phase 1 trial in patients with solid tumors with a vascular endothelial growth factor (VEGF-A) targeting Anticalin antagonist (PRS-050). (9) Clinical safety and tolerability was confirmed together with clinical responses, biomarker inhibition,

4

and target engagement. This particular Anticalin displayed a terminal half-life of 6 days and no anti-drug antibody responses were observed for duration of the trial following repeat dosing (over 9 months on therapy). (9) These results support the utility of the Anticalin drug platform for broad therapeutic and diagnostic applications.

Molecular imaging has permitted the visualization of the organ distribution of antibodies by using labeled versions (e.g. zirconium-89 ^{89}Zr; t1/2 = 78.4 h) of these drugs as a tracer. (10-13) In previous studies, we developed the positron emission tomography (PET) radiopharmaceuticals ^{89}Zr labeled bevacizumab to image VEGF and ^{89}Zr-trastuzumab to image human epidermal growth factor receptor 2 (HER2) in tumors. We tested them successfully preclinical and clinically demonstrating the potential of clinical antibody imaging using these traces for tumor detection, treatment monitoring and drug distribution. (10-13) In order to visualize *in vivo* c-Met expression and study the organ distribution of the Anticalin we generated a radiolabeled version of the c-Met targeting agent (^{89}Zr-PRS-110) and assessed its specific uptake in different human tumor xenograft models. The potential application of Anticalins as imaging agents and the utility of radiolabeled PRS-110 is described herein.

MATERIALS AND METHODS

Cell lines

Cell lines with various c-Met expressions were used. The human non-small cell lung cancer (NSCLC) cell line H441 and human primary glioblastoma U87-MG cell line express c-Met. A2780 is a human ovarian cancer cell line without detectable c-Met expression. All cell lines were obtained from ATCC. c-Met status of the cell lines was determined by flow cytometry analysis using the monoclonal anti-human c-Met-Fluorescein antibody (R&D Systems FAB3582F) (Supplementary Fig. S1). H441 and A2780 cells were cultured in RPMI 1640 (Invitrogen), supplemented with 10% fetal calf serum (FCS) (Bodinco BV) and 2 mM L-glutamine (Invitrogen). U87-MG cells were cultured in DMEM high glucose (Invitrogen), supplemented with 10% FCS in gelatin coated culturing flasks. All cell lines were grown at 37°C in a fully humidified atmosphere containing 5% CO_2.

Synthesis and quality control of conjugated and radiolabeled anticalins

PRS-110 (57 kDa; 3.8 mg/mL; Pieris-AG), the c-Met specific Anticalin containing a 40 kDa L2 branched PEG moiety (7), was allowed to react with deferroxamine-p-SCN (Macrocyclics) as described by Vosjan *et al.* (14) The pH of a 1 mg/mL solution of Anticalin (Pieris AG) was set at 9.5 - 9.7 with 0.1 M Na_2CO_3. Different molar equivalents (2.5, 5 and 10) of the chelator were added. The mixture was incubated at 20 °C for 60 min. Excess deferroxamine-p-SCN was removed by ultracentrifugation using a 30 kDa polyethersulfone (PES) 2 mL Vivaspin-2 filter (Sartorius) and stored in water for injections at -20 °C. The conjugate was radiolabeled

with ^{89}Zr-oxalate (IBA Molecular) to obtain a radiochemical purity of at least 95%. The maximum specific activity for the different conjugates was chelator ratio dependent. Increasing amounts of chelator, resulted in a higher amount of ^{89}Zr which could be bound to PRS-110. A radiochemical purity of >95% could be obtained at a specific activity of 50 MBq/mg for the 1:5 chelated Anticalin.

Conjugated and radiolabeled Anticalins were analyzed for aggregation and (radiochemical) purity by size exclusion high performance liquid chromatography (SE-HPLC). SE-HPLC analysis of the conjugated and radiolabeled Anticalins showed absence of aggregates, fragments or radioactive impurities (Supplementary Fig. S2A).

Analysis of c-Met binding capacity of PRS-110 after conjugation was performed by a direct binding ELISA analysis. A 12-point dilution series of conjugated and unconjugated PRS-110 was prepared in assay buffer: phosphate-buffered saline (Life technologies) containing 0.1% Tween 20 (Roth) and 2 % bovine serum albumin (Roth). Recombinant human c-Met extracellular domain, consisting of HGF R α E25-R307 and HGF R β S308-T932 fused to Fc (Recombinant Human HGF R/c-Met Fc Chimera) (R&D Systems) in PBS (3 µg/mL) was added to each well of a 384 -microtiter plate and incubated overnight at 4 °C. The plates were blocked for 1 h with assay buffer before the Anticalin dilution was added and incubated for 1 h at room temperature. Anti-Anticalin-horseradish peroxidase (Pieris AG) was added and incubated at room temperature for 1 h. Fluoresence signal measurement was performed 5 min after addition of QuantaBlu (Thermo Scientific). In between each step the plate was washed with PBS containing 0.05% Tween 20 using a Biotek ELx405 Select CW washer. Fluorescence signals in RFU (relative fluorescence units) were measured using the Safire2 microplate reader (Tecan) at an excitation wavelength of 320 nm and emission wavelength of 430 nm. The half maximal effective concentration (EC50) values were calculated using the 4 Parameter Logistic (4PL) model with bottom fixed at zero and a fixed slope of 1. There was no detectable difference in binding capacity between the conjugated PRS-110 at a molar ratio of 2.5, 5 and 10 as tested with ELISA (Supplementary Fig. S2B).

Stability of the radiolabeled Anticalin for ^{89}Zr-PRS-110 was monitored in 0.9% NaCl at 4 ^{0}C and in human serum at 37 ^{0}C. ^{89}Zr-PRS-110 showed excellent stability in both conditions with minor release of ^{89}Zr from PRS-110 up to 168 h after radiolabeling (Supplementary Fig. S2C). Based on the tracer validation results, the 1:5 conjugated PRS-110 was selected for the *in vivo* studies.

A non-specific control 40kDa L2 PEGylated Anticalin (Tear lipocalin; Tlc-PEG) was conjugated and radiolabeled using the same procedure. Tlc-PEG was conjugated to deferroxamine-p-SCN at a ratio of 1:5, the optimal ratio as determined for PRS-110.

IRDye 800CW (Licor Biosciences) was labeled to the PRS-110 according to Licor's protocol. In short, the pH of a 1 mg/mL solution of PRS-110 was set at 8.5 with 0.1 M Na_2CO_3. IRDye 800CW was added at a molar ration of 1:5 and incubated at 20 °C for 1 h purified and analyzed as described above.

4

^{89}Zr-PRS-110 internalization assay

To determine internalization rates of ^{89}Zr-PRS-110 after binding to c-Met, an *in vitro* assay was performed. H441 cultured cells were harvested with trypsin, washed and diluted in cold 0.5% human serum albumin (HSA) in PBS. Cells (5.10^6) were incubated on ice with 0.1 µg ^{89}Zr-PRS-110 for 1.5 h. After washing twice, medium was added and cells were incubated at 37 °C to allow for internalization. Internalized and membrane bound ^{89}Zr-PRS-110 were separated by 5 min incubation with 0.2 M glycine + 4 M urea buffer. Internalized, membrane bound and ^{89}Zr-RS-110 released in the medium was counted in a LKB-1282-Compu-gamma system (LKB Wallac) and performed in at least three independent experiments.

Animal experiments

For subcutaneous (sc) tumor inoculation, cells were harvested by trypsinization and suspended in medium. *In vivo* imaging and *ex vivo* experiments were conducted using male male nude Balb-c mice (Balb/cOlaHSD-foxn^{nu}) obtained from Harlan (The Netherlands). Mice were sc injected with 5.10^6 H441 cells in 150 µL PBS, 5.10^6 U87-MG or 5.10^6 A2780 cells in 0.3 mL in medium and Matrigel (BD Biosciences). Tumor growth was followed with caliper measurements. The tracer injection was performed for H441 and U87-MG 3 weeks, and for A2780 2 weeks after tumor cell inoculation.

For biodistribution studies, 10 µg PRS-110 was labeled with 1 MBq ^{89}Zr, unlabeled PRS-110 was added to reach the desired Anticalin dose. Biodistribution analyses were performed at 96 h after injection. This timepoint was chosen based on experience with ^{89}Zr-antibody imaging, where the optimal time for imaging was 72-144 h after antibody tracer injection. (10, 12) At 96 h after tracer injection, optimal tumor accumulation of ^{89}Zr is expected and blood pool availability of ^{89}Zr-PRS-110 is reduced due to clearance of the Anticalin.

A dose escalation biodistribution study with ^{89}Zr-PRS-110 was performed in sc H441 tumor bearing mice to evaluate dose dependent tumor uptake of the Anticalin. Four dose groups of 10, 50, 100 and 500 µg cold PRS-110 were included. Each dose was administered to animals (n = 4-6) via intravenous (iv) penile vein injection. The tracer and the cold dose were injected simultaneously.

To assess *in vivo* c-Met specific uptake in different tumor models with differential c-Met expression and to assess the time dependent organ distribution of ^{89}Zr-PRS-110, microPET imaging was performed in sc xenografted mice (n = 4-6). Mice bearing H441, U87-MG and A2780 tumors, were scanned at 6, 24, 48 and 96 h after injection of 50 µg ^{89}Zr-PRS-110 (5 MBq). After the last scan, mice were sacrificed for biodistribution analysis.

To discriminate between specific and non-specific tumor uptake and biodistribution, 50 µg ^{89}Zr-Tlc-PEG (5 MBq) was injected in H441, U87-MG and A2780 bearing mice. MicroPET imaging was performed and also after the last scan, biodistribution analysis was performed.

Animals were imaged using a microPET Focus 220 rodent scanner (CTI Siemens). After image reconstruction, *in vivo* quantification was performed with AMIDE Medical Image Data Examiner software (version 0.9.1, Stanford University). (15) The data is presented as the mean standard uptake value (SUVmean). Animals were sacrificed at the time of biodistribution, organs and tissues were excised and weighed. Samples and primed standards were counted for radioactivity in a well-type gamma-counter and corrected for physical decay. *Ex vivo* tissue activity is expressed as percentage of the injected dose per gram tissue (%ID/g).

To assess tumor distribution of PRS-110, mice bearing H441 tumors received 100 µg PRS-110-800CW. Mice were sacrificed 96 h after tracer injection and harvested tumors were paraffin embedded for further analysis. The animal experiments were approved by the Institutional Animal Care and Use Committee of the University of Groningen.

Ex vivo analysis

Hematoxylin & eosin (H&E) staining was performed routinely and served to analyze tissue viability and morphology. c-Met immunohistochemistry (IHC) was performed using antibodies detecting human c-Met (Abcam, #ab51067). Photographs were acquired by digitalized scanning of slides using the NanoZoomer 2.0-HT multi-slide scanner (Hamamatsu) and the slides were analyzed using NanoZoomer Digital Pathology (NDP) viewer software (Hamamatsu). Fluorescence microscopy analysis of PRS-110 labeled with IRDye 800CW together with Hoechst staining was determined in tumor sections as described before. (16)

Statistical analysis

Data are presented as mean ± standard deviation (SD). Statistical analyses were performed using Mann-Whitney test (GraphPad 5.00). A P-value ≤ 0.05 was considered significant.

RESULTS

[89]Zr-PRS-110 internalization assays

Internalisation studies were performed with [89]Zr-PRS-110 to determine the fate of the tracer upon binding to c-Met. *In vitro* analysis using H441 cells showed [89]Zr-PRS-110 was rapidly internalized (Fig. 1). The internalized fraction increased from 3 h after start of incubation and stabilized thereafter up to 24 h. Cell surface [89]Zr-PRS-110 decreased during this period.

Dose-escalation biodistribution study

The assessment of [89]Zr-PRS-110 biodistribution at increasing protein dose was performed 96 h after tracer injection in H441 xenografts. The study showed preferential c-Met driven tumor uptake of [89]Zr-PRS-110.

The highest fractional tumor uptake was observed in the 10 µg dose group (Fig. 2). The %ID/g tumor uptake decreased with increasing doses of unlabeled PRS-110 from 7.5 ± 3.4 %ID/g at 10 µg, 5.9 ± 1.1 %ID/g at 50 µg, 4.9 ± 0.5 %ID/g at 100 µg to 2.9 ± 0.9 %ID/g at 500 µg. Liver and kidney uptake was similar for all PRS-110 doses used.
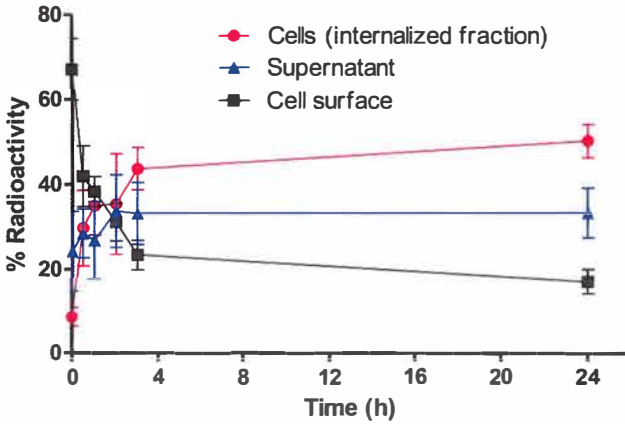

Figure 1 | Membrane binding and internalization of ^{89}Zr-PRS-110 after binding c-Met on H441 cells. Cell surface (acid buffer), intracellular radioactivity and supernatant fractions, expressed as the percentage of the total activity. Data was obtained in 3 independent experiments.
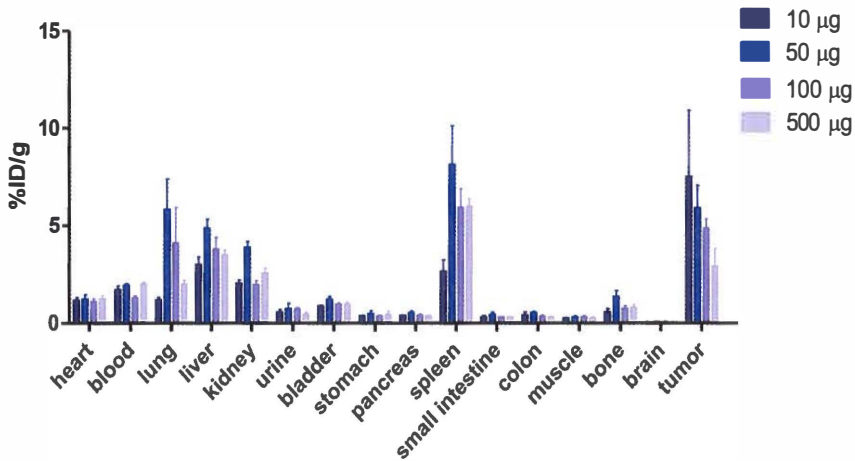

Figure 2 | Biodistribution of ^{89}Zr-PRS-110 at 96 h as determined by *ex vivo* analysis. Four dose groups of 10, 50, 100 and 500 µg PRS-110 were included in the dose-escalation biodistribution (4-6 mice per group). Data are expressed as percentage of the injected dose per gram of tissue (%ID/g).

MicroPET imaging and biodistribution in different tumor models

MicroPET scan analysis of nontarget tissues in xenograft mice revealed a high blood pool presence of ^{89}Zr-PRS-110, together with liver and kidney tracer uptake, 6 h after injection of 50 μg ^{89}Zr-PRS-110. Quantification of PET data showed that the non-specific uptake in these organs decreased over time based on the scans performed at 24, 48 and 96 h after injection of 50 μg ^{89}Zr-PRS-110 (Fig. 3A and 3B). Specific c-Met directed uptake was seen in H441 and U87-MG tumors (Fig. 4A and 4B). Tumor uptake increased between 6 and 24 h. Thereafter, non-target tissue uptake decreased, resulting in increased tumor : organ ratios up to 96 h after tracer injection. A2780 xenografts did show tumor uptake on microPET scans (Fig. 4C), however minimal differences in tumor uptake were seen between the scans at 6, 24, 48 and 96 h post-tracer injection. ^{89}Zr-Tlc-PEG showed the same pharmacokinetic profile based on microPET scans as PRS-110. Furthermore no statistically significant differences were observed between PRS-110 and Tlc-PEG control treated animals. Background non-specific tumor uptake of ^{89}Zr-Tlc-PEG could be seen in all tumor models.
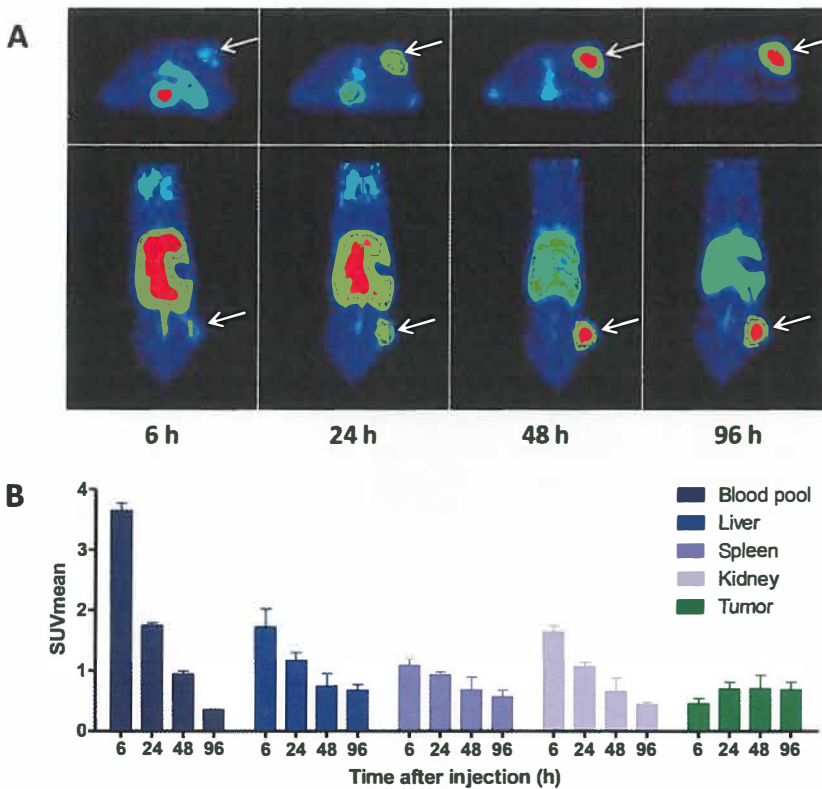

Figure 3 | ^{89}Zr-PRS-110 microPET imaging of H441 bearing mice. Representative transversal and coronal microPET images are shown at 6, 24, 48 and 96 h after tracer injection (A). MicroPET data quantification was performed for blood pool, liver, spleen, kidney and tumor uptake in all mice (4-6 mice per group) (B). Data are expressed as the mean standardized uptake value (SUVmean).
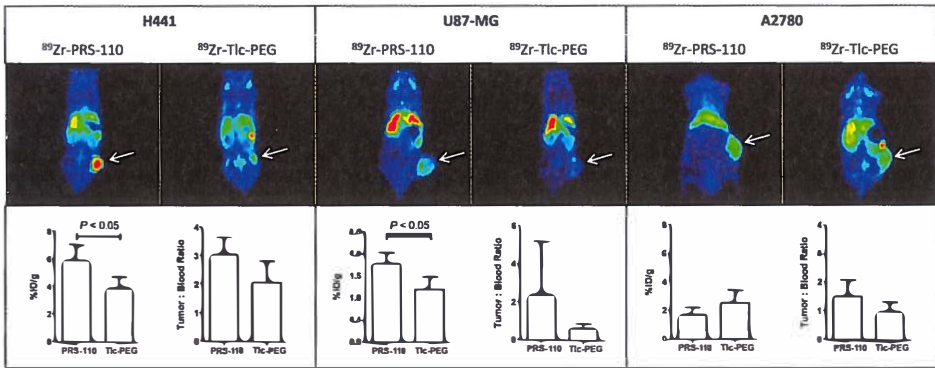
Figure 4 | [89]Zr-PRS-110 microPET imaging of H441, U87-MG and A2780 bearing mice. Representative transversal and coronal microPET images are shown at 96 h after tracer injection of [89]Zr-PRS-110 for c-Met driven tumor uptake and [89]Zr-Tlc-PEG for non-specific tumor uptake (A). *Ex vivo* tumor uptake of [89]Zr-PRS-110 and [89]Zr-Tlc-PEG. To compare specific tumor uptake between tumor models, tumor : blood ratios are provided (B) (4-6 mice per group).
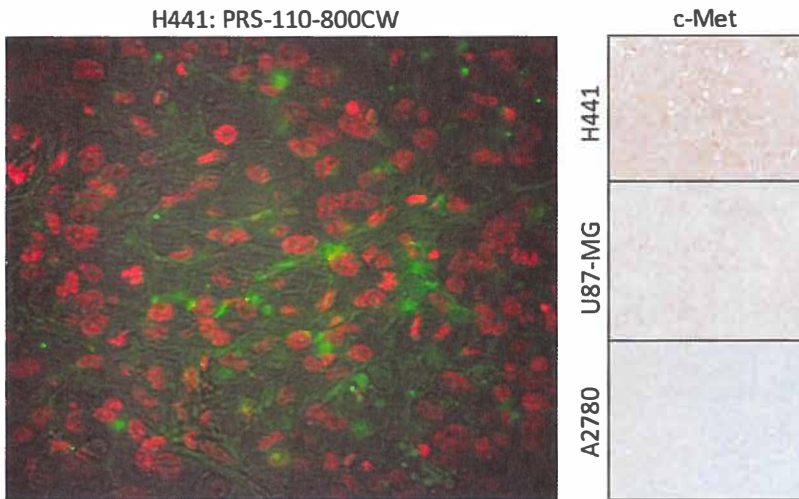
Figure 5 | *Ex vivo* tumor analysis of PRS-110 distribution 96 h after tracer injection in H441 tumor visualized by fluorescence microscopy. The green color is from IRDye 800CW which is labeled to PRS-110 and in red the nuclei are visualized, at the background the tumor structure is visible. The c-Met status of H441, U87-MG and A2780 was determined by immunohistochemistry and a representative picture is included.

After the last scan, mice were sacrificed for biodistribution analysis. Biodistribution data was fully consistent with the microPET findings, showing *ex vivo* tumor uptake of [89]Zr-PRS-110 correlated with c-Met expression (5.9 %ID/g in H441 and 1.8 %ID/g in U87-MG) (P < 0.05) (Fig. 4). [89]Zr-Tlc-PEG control tracer tumor uptake in these models was 3.9 (H441), 1.2 (U87-MG) and 2.5 (A2780) %ID/g. No difference was found between [89]Zr-PRS-110 (1.7 %ID/g) and [89]Zr-Tlc-PEG (2.5 %ID/g) tumor uptake in the A2780 (c-Met negative) model. Tumor : blood ratios of [89]Zr-PRS-110 compared to [89]Zr-Tlc-PEG confirmed these findings.

Ex vivo analysis

IHC on tumor sections of H441 and U87-MG xenografts from the microPET imaging studies revealed both cytoplasmic and membranous c-Met expression. (Fig. 5) In A2780 tumors no c-Met expression was detected. Fluorescence microscopy analysis revealed fluorescence signal of PRS-110 labeled with IRDye 800CW intracellular in H441 tumor cells and at the cell surface. The cellular uptake measured support the desirable pharmacological properties of PRS-110 as a tumor targeting agent by minimizing the impact of off-rate binding kinetics on *in vivo* labeling.

DISCUSSION

In this study, we present a new type of molecular targeted radiopharmaceutical, a [89]Zr labeled Anticalin. The preclinical evaluation of the radiolabeled c-Met Anticalin, [89]Zr-PRS-110, shows that it can be used for non-invasive PET imaging to determine c-Met status *in vivo* and to monitor tumor : organ distribution of PRS-110.

Multiple drug development programs are focused on targeting the HGF/c-Met pathway in human cancer. Currently a number of c-Met focused trials are stratifying patients based on IHC. (17, 18) This has proved useful for onartuzumab, a one-arm Ab with ligand-dependent activity. In a randomized phase II study assessing the combination of onartuzumab with erlotinib progression free survival and overall survival improved in NSCLC patients with tumors overexpressing c-Met (based on IHC). (17) A major drawback of IHC is the fact that tumor tissue is required and the information provided is limited to the biopsied part of one tumor lesion. The plasticity of c-Met expression, potential heterogeneity at different tumor sites and subjective nature of IHC scoring further supports the notion that an imaging agent capable of real time c-Met monitoring may be a useful tool. (19, 20) To select patients upfront, stratify patient populations and inform dosing regimen, molecular imaging with c-Met targeting tracers could give information of whole body c-Met status in all lesions. We show, with [89]Zr-PRS-110, that it is possible to assess c-Met status of the tumor with a clear correlation between signal intensity and receptor expression. Therefore, molecular imaging with [89]Zr-PRS-110 could support selection of patients for the c-Met targeting drugs and inform treatment decisions in the future.

Interestingly the development and quality control of [89]Zr-PRS-110 provided similar results as previously seen for [89]Zr labeling of non-c-Met antibodies. This underscores the robustness of this labeling methodology and the flexibility of Anticalins as tracers. We performed biodistribution experiments for [89]Zr-PRS-110 96 h after tracer injection. Maximal tumor uptake is already visible 24 h after tracer injection, however the ratio between tumor uptake and other organs increases over time after tracer injection. This indicates internalization and accumulation of the [89]Zr in the tumor which was also shown in our *in vitro* studies.

The clearance rate of the Anticalins is faster than that of antibodies, due to their smaller size. For antibody imaging, preclinical studies revealed optimal scanning between 72 and 144 h after [89]Zr-tracer injection. (10, 12) Optimal clinical antibody imaging for [89]Zr-bevacizumab and [89]Zr-trastuzumab requires a 4 day interval between tracer injection and imaging. (11, 13) The phase I results of the PEGylated anti-VEGF-A Anticalin showed a non-linear pharmacokinetic profile of the Anticalins and a terminal half-life of 6 days. (9) Preclinical pharmacokinetic profile assessment in 3 species and allometric scaling predict a human half-life of approximately 5 days for the PEGylated PRS-110. (8) For Anticalin imaging purposes, the optimal radioisotope for imaging should have a comparable physical half-life. Therefore, we chose to use [89]Zr to perform PET imaging with the Anticalin. For this new radiopharmaceutical, the optimal time-point for clinical imaging will need to be determined in a phase I clinical imaging study. Based on the current preclinical findings, it is expected that the optimal time point for tumor imaging will be within 2 days after tracer injection as optimal tumor targeting is reached and blood pool availability of the tracer is clearly reduced, which may facilitate more efficient imaging than conventional antibodies.

To study the specificity of [89]Zr-PRS-110, tumor uptake results were compared with the non-specific Anticalin control ([89]Zr-Tlc-PEG). This showed that tumor uptake of [89]Zr-PRS-110 was superior to the non-targeted control in c-Met expressing tumor models H441 and U87-MG. Just as for IgGs there was also some non-specific tumor uptake of [89]Zr-Tlc-PEG. This is considered to be caused by the enhanced permeability and retention effects and illustrate that anticalins reach their target organ. (21) Another confirmation of specific c-Met driven uptake is provided by the dose escalation biodistribution study. An excess of unlabeled PRS-110 reduced the tumor uptake in H441 tumors, which is caused by saturation of the c-Met receptor by unlabeled PRS-110.

Previous preclinical studies have also assessed c-Met targeting imaging agents and demonstrated potential utility. With SPECT imaging, human U87-MG tumor bearing mice tumors could be visualized with ^{125}I labeled c-Met binding peptides. (22) Moreover ^{125}I labeled Met3 and Met5 antibodies were tested in a panel of human and canine cancer xenografts and showed qualitatively similar SPECT images in mice. (23) These tumor visualization results became more explicit by using the residualizing radionuclide (which retain intracellular) [89]Zr for PET imaging. PET imaging experiments with the monoclonal antibody DN30, labeled with [89]Zr or [124]I showed that [89]Zr-DN30 tumor uptake was much higher than iodine labeled DN30 in GLT-16 and FaDu xenograft models indicating internalization of DN30 and residualization of [89]Zr. (24) Onartuzumab (MetMAb) labeled with [76]Br or [89]Zr ([76]Br-MetMAb and [89]Zr-Df-MetMAb) showed specific uptake and slow clearance of both tracers in imaging and biodistribution studies in tumor xenografts. (25) As observed with other antibodies maximal tumor accumulation took up to 120 h for [89]Zr-Df-MetMAb. With [89]Zr-PRS-110 similar levels of tumor uptake were seen compared to those reported for labeled MetMAb. In addition we characterized target expression and tracer uptake and observed a direct correlation between c-Met level and [89]Zr-PRS-110 uptake in our studies. We could distinguish the tumor uptake of [89]Zr-PRS-110 between the high c-Met expressing cell line H441 and the medium expressing tumor model U87-MG. Tracer uptake

in the c-Met negative A2780 model was similar to non-specific control. This indicates that [89]Zr-PRS-110 can be used for non-invasive assessment of the c-Met expression levels in tumor lesions. Fluorescence microscopy analysis revealed fluorescence signal of PRS-110 intracellularly and at the cell surface. PRS-110 was mostly located within tumor cells, indicating intracellular uptake of PRS-110 after internalization. This favors the use of [89]Zr for PET imaging, as it is a residualizing isotope, which accumulates in the tumor cells upon binding and internalization of [89]Zr-PRS-110 to c-Met.

PRS-110 competes with human HGF for binding to the c-Met receptor. In the current preclinical study, PRS-110 was only competing with human HGF produced by human tumor cells for the binding to c-Met as murine HGF does not cross-react with human c-Met. (26) In the clinical setting tumor signals of [89]Zr-PRS-110 may be influenced by HGF produced by paracrine and/or endocrine routes due to competition for its target, c-Met however we still expect significant specific uptake, as PRS-110 has higher affinity for c-Met compared to HGF. (27, 28) In summary, in different preclinical models [89]Zr-PRS-110 microPET was shown to image and inform about *in vivo* c-Met tumor status. [89]Zr-PRS-110 is ready for clinical evaluation and has potential utility in the selection and monitoring of patients for c-Met therapy.

4

REFERENCES

1. Blumenschein GR, Jr., Mills GB, Gonzalez-Angulo AM. Targeting the hepatocyte growth factor-c-Met axis in cancer therapy. J Clin Oncol 2012;30:3287-96.

2. Gherardi E, Birchmeier W, Birchmeier C, VandeWoude G. Targeting c-Met in cancer: rationale and progress. Nat Rev Cancer 2012;12:89-103.

3. Skerra A. Lipocalins as a scaffold. Biochim Biophys Acta 2000;1482:337-50.

4. Skerra A. Alternative binding proteins: anticalins - harnessing the structural plasticity of the lipocalin ligand pocket to engineer novel binding activities. FEBS J 2008;275:2677-83.

5. Gebauer M, Skerra A. Anticalins small engineered binding proteins based on the lipocalin scaffold. Methods Enzymol 2012;503:157-88.

6. Schonfeld D, Matschiner G, Chatwell L, Trentmann S, Gille H, Hulsmeyer M, et al. An engineered lipocalin specific for CTLA-4 reveals a combining site with structural and conformational features similar to antibodies. Proc Natl Acad Sci USA 2009;106:8198-203.

7. Gille H, Matschiner G, Hülsmeyer M, Bel Aiba S, Christian H, Trentmann S, et al. A monovalent Anticalin antagonist: A novel approach for inhibition of cMet-dependent tumor growth. Proc AACR Annual meeting 2011; abstract #3621.

8. Gille H, Matschiner G, Hülsmeyer M, Joffroy C, Bel Aiba RS, Christian H et al. Exploiting the anticalin therapeutic protein platform for the treatment of cMet ligand-independent and dependent tumors - discovery and characterization of a highly specific and potent c-Met antagonist with drug-like properties. Proc AACR Annual meeting 2011; abstract #3875.

9. Mross K, Fischer R, Richly H, Scharr D, Buechert M, Stern A, et al. First in human phase I study of PRS-050 (angiocal), a VEGF-A targeting Anticalin, in patients with advanced solid tumors: results of a dose escalation study. Proc EORTC-NCI-AACR meeting 2011; abstract #A212.

10. Nagengast WB, de Vries EG, Hospers GA, Mulder NH, de Jong JR, Hollema H, et al. In vivo VEGF imaging with radiolabeled bevacizumab in a human ovarian tumor xenograft. J Nucl Med 2007;48:1313-9.

11. Oosting SF, Brouwers AH, Van Es SC, Nagengast WB, Oude Munnink TH, Lub-de Hooge MN, et al. 89 Zr-bevacizumab PET imaging in metastatic renal cell carcinoma patients before and during antiangiogenic treatment. J Clin Oncol 30, 2012 (suppl; abstr 10581).

12. Dijkers EC, Kosterink JG, Rademaker AP, Perk LR, van Dongen GA, Bart J, et al. Development and characterization of clinical-grade [89]Zr-trastuzumab for HER2/neu immunoPET imaging. J Nucl Med 2009;50:974-81.

13. Dijkers EC, Oude Munnink TH, Kosterink JG, Brouwers AH, Jager PL, de Jong JR, et al. Biodistribution of [89]Zr-trastuzumab and PET imaging of HER2-positive lesions in patients with metastatic breast cancer. Clin Pharmacol Ther 2010;87:586-92.

14. Vosjan MJ, Perk LR, Visser GW, Budde M, Jurek P, Kiefer GE, et al. Conjugation and radiolabeling of monoclonal antibodies with zirconium-89 for PET imaging using the bifunctional chelate p-isothiocyanatobenzyl-desferrioxamine. Nat Protoc 2010;5:739-43.

15. Loening AM, Gambhir SS. AMIDE: a free software tool for multimodality medical image analysis. Mol Imaging 2003;2:131-7.

16. Terwisscha van Scheltinga AG, van Dam GM, Nagengast WB, Ntziachristos V, Hollema H, Herek JL, et al. Intraoperative near-infrared fluorescence tumor imaging with vascular endothelial growth factor and human epidermal growth factor receptor 2 targeting antibodies. J Nucl Med. 2011;52:1778-85.

17.   Spigel DR, Ervin TJ, Ramlau R, Daniel DB, Goldschmidt JH, Blumenschein GR, et al. Final efficacy results from
      OAM4558g, a randomized phase II study evaluating MetMAb or placebo in combination with erlotinib in advanced
      NSCLC. J Clin Oncol 29: 2011 (suppl; abstr 7505).

18.   Zhu M, Tang R, Doshi S, Oliner KS, Kathman S, Olsson Gisleskog P et al. Exposure-response (E-R) analysis of
      rilotumumab (R, AMG 102) plus epirubicin/cisplatin/capecitabine (ECX) in patients (pts) with locally advanced or
      metastatic gastric or esophagogastric junction (G/EGJ) cancer. J Clin Oncol 30: 2012 (suppl; abstr 2535).

19.   Steeg PS. Heterogeneity of drug target expression among metastatic lesions: lessons from a breast cancer autopsy
      program. Clin Cancer Res. 2008;14:3643-5.

20.   Matsui S, Osada S, Tomita H, Komori S, Mori R, Sanada Y et al. Clinical significance of aggressive hepatectomy for
      colorectal liver metastasis, evaluated from the HGF/c-Met pathway. Int J Oncol. 2010;37:289-97.

21.   Fang J, Nakamura H, Maeda H. The EPR effect: Unique features of tumor blood vessels for drug delivery, factors
      involved, and limitations and augmentation of the effect. Adv Drug Deliv Rev 2011;63:136-51.

22.   Kim EM, Park EH, Cheong SJ, Lee CM, Kim DW, Jeong HJ, et al. Characterization, biodistribution and small-animal
      SPECT of I-125-labeled c-Met binding peptide in mice bearing c-Met receptor tyrosine kinase-positive tumor
      xenografts. Nucl Med Biol 2009;36:371-8.

23.   Hay RV, Cao B, Skinner RS, Su Y, Zhao P, Gustafson MF, et al. Nuclear imaging of Met-expressing human and canine
      cancer xenografts with radiolabeled monoclonal antibodies (MetSeek). Clin Cancer Res 2005;11:7064s-9s.

24.   Perk LR, Stigter-van Walsum M, Visser GW, Kloet RW, Vosjan MJ, Leemans CR, et al. Quantitative PET imaging
      of Met-expressing human cancer xenografts with [89]Zr-labelled monoclonal antibody DN30. Eur J Nucl Med Mol
      Imaging 2008;35:1857-67.

25.   Jagoda EM, Lang L, Bhadrasetty V, Histed S, Williams M, Kramer-Marek G, et al. Immuno-PET of the hepatocyte
      growth factor receptor Met using the 1-armed antibody onartuzumab. J Nucl Med 2012;53:1592-600.

26.   Jeffers M, Rong S, Woude GF. Hepatocyte growth factor/scatter factor-Met signaling in tumorigenicity and invasion/
      metastasis. J Mol Med 1996;74:505-13.

27.   Basilico C, Arnesano A, Galluzzo M, Comoglio PM, Michieli P. A high affinity hepatocyte growth factor-binding site in
      the immunoglobulin-like region of Met. The J Biol Chem 2008;283:21267-77.

28.   Stamos J, Lazarus RA, Yao X, Kirchhofer D, Wiesmann C. Crystal structure of the HGF beta-chain in complex with
      the Sema domain of the Met receptor. EMBO J 2004;23:2325-35.

4

SUPPLEMENTARY FIGURES
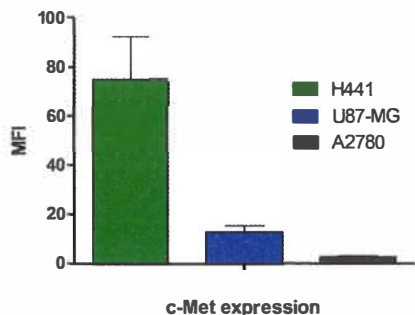
Supplementary Figure S1 | H441, U87-MG and A2780 tumor cells were analyzed for c-Met expression by flow cytometry analysis. The results are presented in mean fluorescence intensity (MFI), data was obtained in 3 independent experiments.
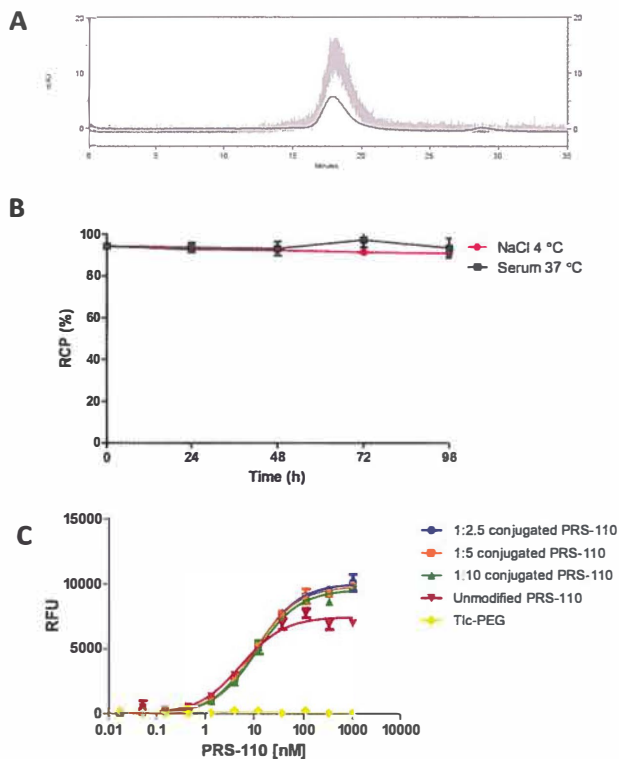
Supplementary Figure S2 | Quality control of ^{89}Zr-PRS-110. Panel A shows a typical SE-HPLC chromatogram of ^{89}Zr-PRS-110 with detection at 280 nm for the protein signal and co-registration of radioactive ^{89}Zr signal. Panel B shows the stability of ^{89}Zr-PRS-110 in 0.9% NaCl at 4 °C and in human serum at 37 °C expressed as radiochemical purity (RCP). Binding of ^{89}Zr-PRS-110 at different chelation ratios was tested in a binding ELISA (C), fluorescence signals in RFU (relative fluorescence units). Data was obtained in 3 independent experiments.

CHAPTER 5

Measurement of tumor VEGF-A levels with [89]Zr-bevacizumab PET as an early biomarker for the antiangiogenic effect of everolimus treatment in an ovarian cancer xenograft model

Arne R.M. van der Bilt[1,2#], Anton G.T. Terwisscha van Scheltinga[1,3#], Hetty Timmer-Bosscha[1], Carolien P. Schröder[1], Linda Pot[1], Jos G.W. Kosterink[3], Ate G.J. van der Zee[2], Marjolijn N. Lub-de Hooge[3,4], Steven de Jong[1], Elisabeth G.E. de Vries[1], Anna K.L. Reyners[1]

[#]These authors contributed equally

[1]Department of Medical Oncology, [2]Department of Gynecological Oncology, [3]Department of Hospital and Clinical Pharmacy, [4]Department of Nuclear Medicine and Molecular Imaging, University of Groningen, University Medical Center Groningen, Groningen, The Netherlands.

ABSTRACT

The mammalian target of rapamycin (mTOR) pathway is frequently activated in ovarian cancers. mTOR inhibitors, like everolimus, can reduce vascular endothelial growth factor-A (VEGF-A) production by cancer cells. We investigated whether early everolimus treatment effects could be monitored by positron emission tomography (PET) with ^{89}Zr-bevacizumab.

Methods:

The effect of everolimus on VEGF-A secretion was determined in a panel of human ovarian cancer cell lines and in A2780^{luc+} ovarian cancer cells xenografted subcutaneously in BALB/c mice. Mice received daily 10 mg/kg everolimus intraperitoneally for 14 days. PET scans with the tracer ^{89}Zr-labeled bevacizumab were performed before and after treatment. Ex vivo ^{89}Zr-bevacizumab biodistribution and correlative tissue analyses were performed. Tumor VEGF-A levels were measured with ELISA and mean vascular density (MVD) was determined with immunohistochemistry.

Results:

Everolimus treatment reduced VEGF-A levels in the supernatant of all cell lines. Everolimus lowered ^{89}Zr-bevacizumab tumor uptake by $21.7 \pm 4.0\%$ (SUV$_{mean}$ 2.3 ± 0.2 versus 2.9 ± 0.2, $P < 0.01$). Ex vivo biodistribution also demonstrated lower tracer uptake in the tumors of treated compared to control animals (7.8 ± 0.8 %ID/g versus 14.0 ± 1.7 %ID/g, $P < 0.01$), while no differences were observed for other tissues. This coincided with lower VEGF-A protein levels in tumor lysates in treated versus untreated tumors ($P = 0.04$) and reduced MVD ($P < 0.01$).

Conclusion:

Tumor VEGF-A levels are decreased by everolimus. ^{89}Zr-bevacizumab PET could be used to monitor tumor VEGF-A levels as an early biomarker of the antiangiogenic effect of mTOR inhibitor therapy.

INTRODUCTION

Ovarian cancer patients often present with advanced stage disease and develop resistance to conventional (platinum-based) chemotherapy during the course of treatment, resulting in a poor 30% 5-year survival rate. (1) To improve ovarian cancer prognosis, there is a clear need for additional therapeutic options. Since ovarian cancers are often extensively vascularized and overexpress proangiogenic factors like vascular endothelial growth factor-A (VEGF-A), angiogenesis inhibition has been studied as a therapeutic strategy. Phase II and III trials with the VEGF-A-neutralizing antibody bevacizumab or with VEGF receptor (VEGFR)-targeted tyrosine kinase inhibitors (TKI) targeting vascular endothelial cells have shown antitumor activity in a subgroup of patients. (2,3)

The kinase mammalian target of rapamycin (mTOR) is a potential alternative target for antiangiogenic therapy. The mTOR pathway is activated in 64-85% of ovarian cancers. (4,5) mTOR enhances translational efficacy of mRNAs that contain intricate 5' untranslated regions (5' UTRs). These regions encode oncogenic proteins like hypoxia-inducible factor (HIF) and VEGF-A. (6,7) By reducing the synthesis of these proteins by tumor cells, mTOR inhibitors have distinct antiangiogenic effects compared to classical antiangiogenic drugs like bevacizumab. (8)

In transgenic (orthotopic) and xenograft mouse models, treatment with the mTOR inhibitor everolimus delayed tumor development, reduced tumor burden and prolonged survival. (9-12) mTOR inhibition reduced VEGF-A expression and diminished vascularization in murine (xenograft) ovarian cancers. (9,10) This was even more pronounced when combined with bevacizumab. (13)

In a phase II trial, 60 patients with persistent or recurrent ovarian cancer received weekly temsirolimus. (14) A partial tumor response was observed in 9.3% of the patients, with disease stabilization in a further 40.7%. (14) This underscores the importance of discovering biomarkers for upfront patient selection or early response prediction. However, no biomarkers are currently established for predicting everolimus or VEGF(R)-targeted drug efficacy in ovarian cancer.

Whole-body positron emission tomography (PET) can potentially address this issue. It offers the possibility for longitudinal *in vivo* monitoring of tumor biology and changes herein upon treatment. In order to visualize antiangiogenic drug efficacy, we generated radiolabeled bevacizumab which proved able to non-invasively detect tumor VEGF-A levels in animal models and patients. (15-17)

The aim of this study was to analyze the effect of everolimus on ovarian cancer VEGF-A secretion *in vitro* and *in vivo*, and the potential of serially measuring tumor VEGF-A levels with [89]Zr-bevacizumab PET as an early predictive biomarker for everolimus antiangiogenic efficacy in an ovarian cancer xenograft model.

MATERIALS AND METHODS

Cell lines

The human ovarian cancer cell line A2780 was kindly provided by Dr TC Hamilton (Fox Chase Cancer Center). The luciferase transfected subline A2780[luc+] was developed as described earlier. (18) SKOV-3 and TOV-21G ovarian cancer cell lines were obtained from the American Type Culture Collection (ATCC). A2780 and A2780[luc+] cells were cultured in RPMI1640, supplemented with 10% fetal calf serum (FCS, Bodinco BV) and 2 mM L-glutamine (Invitrogen), SKOV-3 in Dulbecco's Modified Eagles Medium (DMEM) with 4.5 g/L glucose, supplemented with 10% FCS, and TOV-21G cells in Ham-F12 and DMEM (1:1), supplemented with 10% FCS. All culture media were purchased from Invitrogen. All cell lines were cultured at 37 °C in a fully humidified atmosphere containing 5% CO_2.

For *in vitro* experiments, cells were harvested with trypsin after a single wash with phosphate-buffered saline (PBS: 6.4 mM Na_2HPO_4, 1.5 mM KH_2PO_4, 0.14 mM NaCl, 2.7 mM KCl, pH = 7.2) and seeded in 6-well plates (A2780: 31,500 cells/cm², SKOV-3: 21,000 cells/cm², TOV-21G: 52,500 cells/cm²). The next day, everolimus was added in fresh medium (1.5 mL/well) to reach final concentrations of 0-100 nM.

Compounds

Everolimus was obtained from LC Laboratories (E-4040, stored at -20 °C). For *in vitro* use, everolimus was dissolved in dimethyl sulfoxide (DMSO) at 10 mM stock concentration stored at -20 °C. For *in vivo* use, everolimus was dissolved in DMSO and formulated in a stable suspension with PBS containing 0.5% Tween-80 (Sigma-Aldrich). Mice received 10 mg/kg everolimus daily via intraperitoneal injection (10 mL/kg). The everolimus dosage used is based on previous efficacy studies in xenografted mice, in which 5-10 mg/kg daily resulted in unbound (active) everolimus plasma levels comparable to those reached in humans receiving 5-10 mg daily due to higher plasma protein binding and shorter $T_{1/2}$ values in mice. (8,19-22)

Western blotting

Total and phosphorylated protein expression of mTOR target proteins was measured by Western blotting. After 24 hours everolimus exposure, adherent cell layers were washed three times with ice-cold PBS and total cellular protein content was extracted with mammalian protein extraction reagent (M-PER, Thermo Scientific). Protease and phosphatase inhibitors (Thermo Scientific) were added (1:100). Protein yield was determined with the Bradford assay. (23) Samples were diluted 1:1 with sodium dodecyl sulphate (SDS) sample buffer, containing 125 mM Tris-HCl, 2% SDS, 10% glycerol, 0.001% bromophenol blue and 10% β-mercaptoethanol, and boiled for 5-10 minutes before storage at -20 °C. Proteins (20-30 μg) were separated on SDS-polyacrylamide gels and transferred onto polyvinylidene difluoride (PVDF) membranes (Immobilon-P, Millipore) by wet blotting. (24) Primary antibodies were purchased from Cell Signaling, recognizing epitopes on p70S6K (#2708), phosho-p70S6K (Thr389) (#9206), S6 (#2217), phospho-S6 (Ser235/236) (#4856),

4E-BP1 (#9644) and phospho-4E-BP1 (Thr70) (#9455). Anti-β actin antibody (BP Biomedicals) served to assure equal protein loading. Membranes were incubated with horseradish peroxidase-labeled secondary antibodies (DAKO) for 1 hour at room temperature. Protein bands were visualized with chemiluminescence using Lumi-Light^{plus} (Roche Diagnostics).

VEGF-A ELISA

After 24 hours incubation with everolimus, cell culture supernatant was removed and centrifuged for 10-15 minutes at 450 x g, to remove any residual cells or cell remnants, and subsequently stored in aliquots at -20 °C until VEGF-A levels were measured with VEGF Quantikine enzyme-linked immunosorbent assay (ELISA) kits (DVE00, R&D Systems). To correct for experimental differences, cell counting was performed in parallel for each sample using conventional counting grids and trypan blue staining.

For *in vivo* studies, three random cores were die-cut from frozen tumor samples and lysed using M-PER. (16) In these whole-tumor protein lysates, VEGF-A levels were assayed with ELISA kits and total protein content with Bradford assays as described in the above.

Xenograft model

All animal experiments were approved by the Institutional Animal Care and Use Committee of the University of Groningen. Animal studies were performed in male nude BALB/c mice (BALB/cOlaHsd-*Foxn1^{nu}*, Harlan). Animals were allowed to feed *ad libitum*. Experiments were performed under isoflurane inhalation anesthesia (induction 3%, maintenance 1.5%).

Mice (n = 10) were xenografted subcutaneously in the flank with 5 x 10^6 A2780^{luc+} cells resuspended in 0.3 mL of a 1:1 mixture of PBS and Matrigel (BD Biosciences). To ensure tumor viability, bioluminescence imaging was performed using the IVIS Spectrum system (Caliper Life Sciences). D-luciferin (150 mg/kg, purchased from Xenogen) was reconstituted in PBS and injected intraperitoneally 20 minutes before image acquisition. Twelve days after tumor inoculation, when the tumor diameter measured 6-8 mm (~300 mm^3), a baseline 6-day microPET scan sequence was performed to determine pretreatment ^{89}Zr-bevacizumab tracer uptake (Supplemental Fig. S1). Daily everolimus treatment (10 mg/kg intraperitoneal administration) was started immediately after completing the baseline scan sequence and continued for 14 days. On day 9 during everolimus treatment, a second 6-day scan sequence was initiated after ^{89}Zr-bevacizumab injection. Animals that received everolimus were sacrificed immediately after acquiring the post-treatment scans.

To allow comparison between treated *versus* untreated tumors, a separate group of mice (*n* = 5, control group) was sacrificed after the baseline scans. Mice xenografted with A2780^{luc+} cells develop rapidly growing tumors, with a doubling time of 3-6 days. (16) Therefore, control animals cannot be maintained for the same duration as the treatment group, since tumors will grow beyond tolerable sizes. To obtain data on tumor volumes, regular caliper measurements were performed as described previously. (17) Tumor growth curves were related to control data from untreated A2780^{luc+} tumor-bearing mice obtained earlier. (17)

MicroPET imaging

Bevacizumab conjugation and labeling were performed as described previously. (15) Briefly, quality controls included size-exclusion high-performance liquid chromatography (SE-HPLC), trichloroacetic acid (TCA) precipitation and immunoreactivity analysis. Radiochemical purity of all injected tracers was > 95%. ^{89}Zr-bevacizumab (± 5 MBq, ± 30 μg) was injected into the penile vein. Animals were imaged using a MicroPET Focus 220 rodent scanner (CTI/Siemens). Static images were obtained (15-45 minutes acquisition) immediately after tracer injection and at 144 hours after tracer injection. In earlier tracer validation studies it was shown that the ^{89}Zr-bevacizumab tumor uptake was significantly higher compared to ^{89}Zr-IgG uptake, demonstrating target-driven, tumor-specific binding and accumulation of the tracer. (15,16) ^{89}Zr-bevacizumab tumor uptake is optimal in this animal model at 144 hours after tracer injection. (15,16) The tracer dose was also based on these tracer validation studies. (25) At this tracer dose, any retained cold antibody from the first tracer injection is not expected to influence tumor uptake at the second scanning period. Images were analyzed and quantified using AMIDE software (version 0.9.1, Stanford University). (26) Imaging data are presented as the mean standardized uptake value (SUV$_{mean}$). (17)

Biodistribution

Organs and tissues were excised, rinsed of residual blood and weighed. Tissues were counted for radioactivity in a calibrated well-type LKB-1282-Compu-gamma system (LKB Wallac), together with reference tracer material to correct for physical decay. *Ex vivo* tissue activity is expressed as the percentage of the injected dose per gram of tissue (%ID/g). Harvested tumors were divided, and partly paraffin-embedded and partly frozen at -80 °C for further *ex vivo* analysis.

Immunohistochemistry

Slices (3 μm thick) were cut from paraffin-embedded tumor sections using a microtome and placed on 3-aminopropyltriethoxysilane-coated glass slides. Heat-induced antigen retrieval was performed in 10 mM citrate buffer (S6, p-S6) or Tris/EDTA (Ki67) using a 400 W rotary microwave, or by using Proteinase K (vWF) at room temperature. Endogenous peroxidase was blocked by 30 minutes incubation with 0.3% H_2O_2 in PBS. Endogenous avidin/biotin activity was blocked using a commercially available blocking kit (Vector Laboratories). Slides were incubated with primary antibodies detecting human S6 and p-S6 (Cell Signaling, #2217 and #2211) and Ki67 (Dako, 1:350). In addition, slides were stained with anti-Von Willebrand factor antibody (vWF) (Dako, 1:250) to determine the mean vascular density (MVD). (17) Staining was visualized after incubation with biotinylated or peroxidase-bound secondary antibodies (Dako) using, when necessary, the streptavidin-biotin/horseradish peroxidase complex (Dako) and 3,3'-diaminobenzidine (Sigma-Aldrich). Hematoxylin counterstaining was applied routinely and hematoxylin & eosin (H&E) staining served to analyze tissue viability and morphology.

Stainings were quantified by evaluation of 10 high-power fields (400x magnification) using a calibrated grid, counting positive and negative cells (S6 and p-S6, cytoplasmic staining) or nuclei (Ki67). Data is expressed as the percentage of positive cells. MVD was determined by counting and averaging the number of vessels within 10 high-power fields. Photographs were acquired by digitalized scanning of slides using the NanoZoomer 2.0-HT multi-slide scanner (Hamamatsu). To calculate tumor viability, acquired images from H&E stained slides were analyzed using NanoZoomer Digital Pathology (NDP) viewer software (Hamamatsu). Using the freehand surface area tool, areas with non-viable tumor tissue were delineated within fixed-size squares overlaying the surface area of the slide.

Statistical analyses

Data are presented as mean ± standard deviation (SD). For *in vitro* experiments, different experimental conditions were compared using unpaired Student's t-tests. Comparison of [89]Zr-bevacizumab uptake before and after everolimus treatment was performed using the paired t-test, while unpaired testing was used for *ex vivo* analyses (comparing control *versus* treatment group data). Correlations were determined by Pearson's correlation coefficient. Statistical analyses were performed using Prism v.5 (GraphPad). A *P*-value of < 0.05 (two-tailed) was considered significant.

RESULTS

5

mTOR inhibition by everolimus reduces ovarian cancer VEGF-A secretion *in vitro*

Target inhibition by everolimus was shown by reduced phosphorylation of p70S6K, S6 and 4E-BP1 in all cell lines tested (Fig. 1A). mTOR inhibition occurred within 2 hours upon everolimus exposure (Fig. 1B).

Everolimus reduced VEGF-A secretion by all cell lines ($P < 0.05$ at all concentrations used, compared to untreated controls) (Fig. 2). The maximum effect was achieved at relatively low concentrations of everolimus (10 nM). After 24 hours drug exposure, VEGF-A levels in the culture supernatant were reduced by 57 ± 7% in A2780, 42 ± 15% in SKOV-3 and 38 ± 3% in TOV-21G cells compared to untreated cells. Cell counting experiments revealed no effect on cell number or viability after 24 hours everolimus incubation.

Everolimus reduces [89]Zr-bevacizumab tumor uptake in xenografted mice

[89]Zr-bevacizumab tracer uptake was homogeneously present within the tumors analyzed at each timepoint based on microPET scans. Everolimus decreased [89]Zr-bevacizumab tumor uptake compared to pretreatment (baseline) scans in all animals. Figure 3A shows representative PET images. In pretreatment scans, the SUV_{mean} was 2.9 ± 0.2, compared to 2.3 ± 0.2 in posttreatment scans after 2 weeks of everolimus treatment (21.7 ± 4.0% decrease in tracer uptake, $P = 0.0005$) (Fig. 3B).

Analogous, *ex vivo* biodistribution experiments demonstrated a lower [89]Zr-bevacizumab tumor uptake in everolimus-treated animals *versus* control animals (7.8 ± 0.8 %ID/g *versus* 14.0 ± 1.7 %ID/g, $P < 0.01$; Fig. 3C). These results correlated with microPET quantification data ($R^2 = 0.93$, $P < 0.0001$). No differences in [89]Zr-bevacizumab uptake were observed for non-tumor tissues between treated and untreated animals (Fig. 3D).
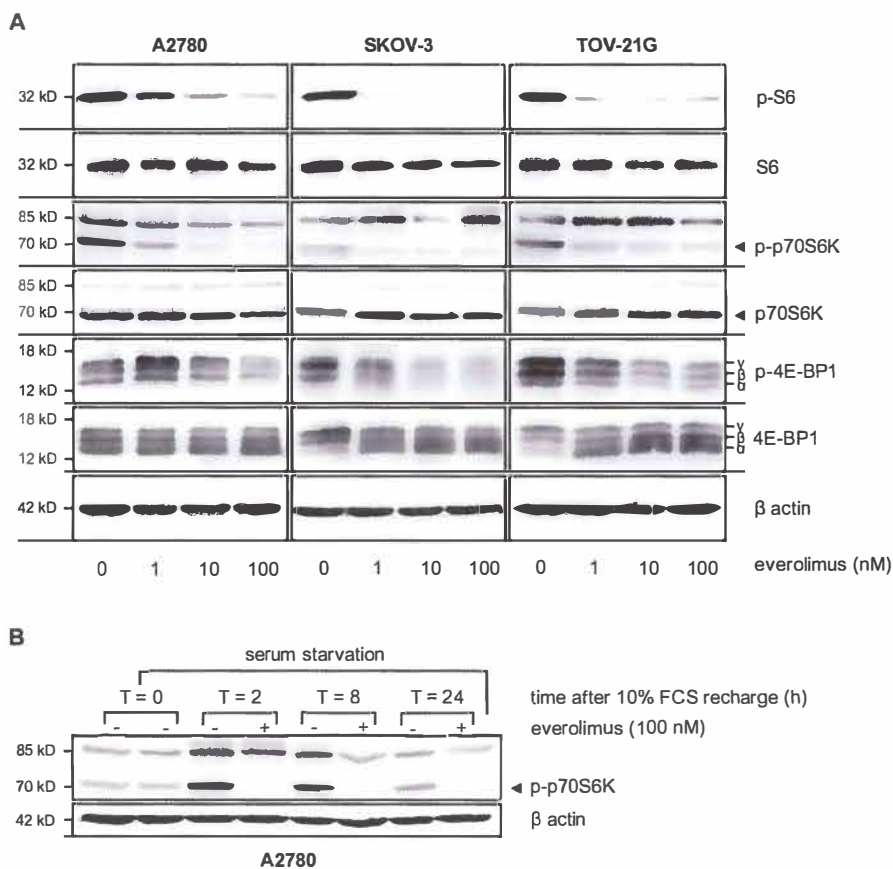

Figure 1 | (A) A2780, SKOV-3 and TOV-21G cells were treated for 24 hours with everolimus at the indicated concentrations. Western blotting showed that phosphorylation of downstream mTOR target proteins S6, p70S6K and 4E-BP1 was effectively reduced in all cell lines at all concentrations used. The upper band in the (p-)p70S6K blots is a consequence of analogous binding to p85S6K, which is another S6K splice variant. The α, β and γ isoforms of 4E-BP1 reflect differential phosphorylation, with the γ isoform being most extensively phosphorylated. β actin was used as a loading control. (B) A2780 cells were serum-starved overnight before everolimus (100 nM) was added to the culture medium. After 30 minutes of pre-incubation with everolimus, FCS was added for the indicated timepoints. As shown by the lack of p70S6K phosphorylation, mTOR is already inhibited shortly after drug exposure and inhibition persisted throughout the whole incubation period.

During the 14-day treatment period, tumor volumes in mice receiving everolimus increased to a maximum of 135 ± 17% compared to the start of treatment (Fig. 4). Tumor growth during everolimus treatment was slower compared to historical controls (untreated A2780[luc+] xenograft-bearing mice), which showed a similar increase in tumor volume already at day 3 after baseline scans. (17)

Decreased [89]Zr-bevacizumab tumor uptake corresponds with reduced tumor VEGF-A levels and reduced vascularity after everolimus treatment

Everolimus treatment resulted in effective target inhibition as the expression of phosphorylated S6 was clearly reduced in treated tumors *versus* tumors obtained from control animals after baseline scanning, while total S6 expression was not affected (Fig. 5A). Morphologic analysis of H&E stained slides revealed no difference in tumor viability between treated and control tumors (Fig. 5B). After 2 weeks of everolimus treatment the Ki67-based proliferation index was lower in treated (30.21 ± 1.76%) compared to control tumors (50.86 ± 1.46%, $P < 0.0001$) (Fig. 5C).

VEGF-A protein expression was lower in everolimus-treated *versus* control tumors (0.33 ± 0.02 *versus* 0.50 ± 0.16 pg/μg total protein, $P = 0.04$) (Fig. 5D). In addition, everolimus treatment reduced tumor vascularity, as the MVD averaged 4.1 ± 1.4 in treated *versus* 7.8 ± 1.4 vessels per high-power field ($P < 0.01$) in control mice (Fig. 5E). VEGF-A protein levels correlated with microPET quantification data ($R^2 = 0.43$, $P < 0.05$) and *ex vivo* biodistribution data ($R^2 = 0.44$, $P < 0.05$).

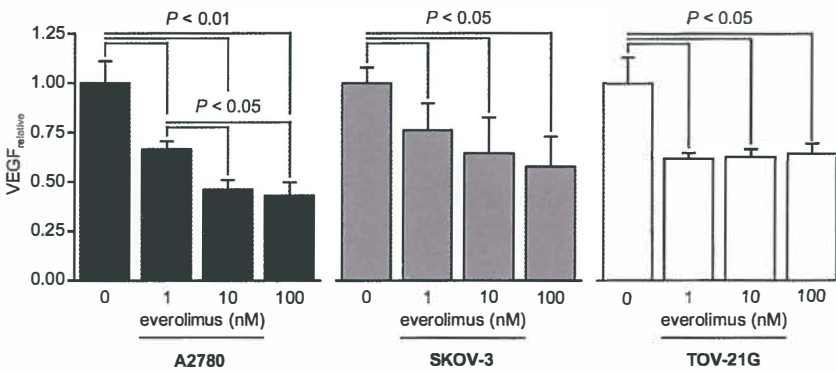

Figure 2 | Everolimus reduces VEGF-A secretion in a panel of three ovarian cancer cell lines. Cells were exposed for 24 hours at the indicated concentrations of everolimus. VEGF-A levels (measured in pg/mL supernatant) are expressed relative to those measured in the supernatant of untreated cells, corrected for cell number. VEGF-A levels were lower at all concentrations used ($P < 0.05$).
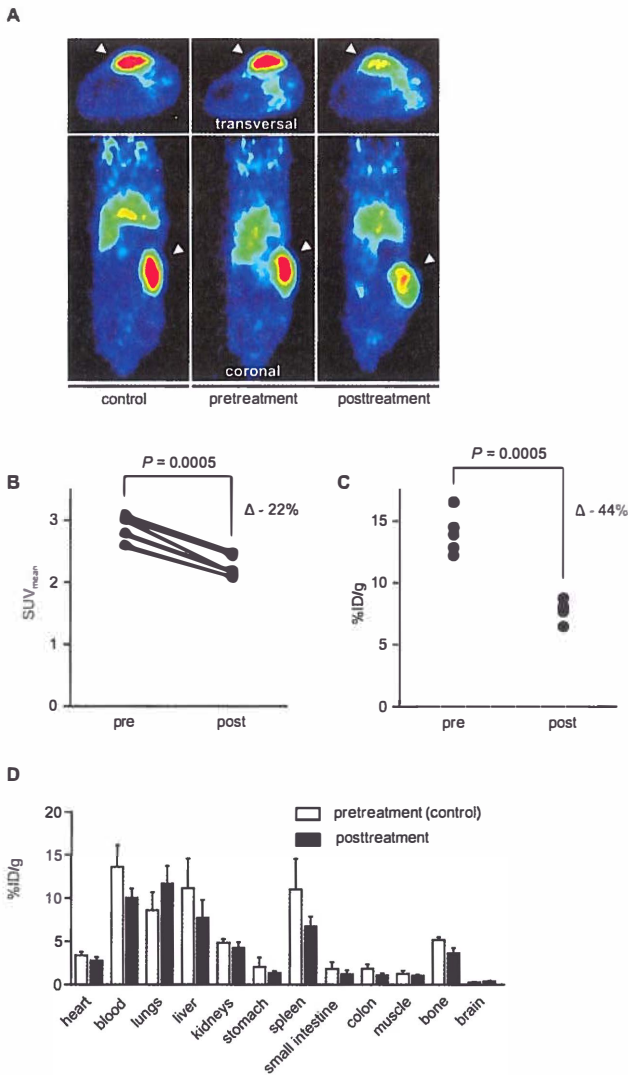
A

B

C

D

Figure 3 I (A) Representative transversal and coronal ^{89}Zr-bevacizumab microPET images of A2780^{luc+} xenografted mice in the control and treatment group. Pre- and posttreatment images are from the same animal. Tumors are indicated by arrowheads. Scans were acquired with the animals lying sideways with the inoculated left flank upwards. Tracer uptake in the tumor is clearly visible, as well as some aspecific liver uptake. (B) MicroPET quantification in individual everolimus-treated animals demonstrated a clear reduction in the SUV$_{mean}$ compared to pretreatment scans. A 22 ± 4.0% decrease in tracer uptake was observed ($P = 0.0005$). (C) *Ex vivo* biodistribution was performed in control and treated animals directly after obtaining the final ^{89}Zr-bevacizumab PET scans. Tracer uptake is expressed as percentage of injected dose per g tissue (%ID/g). Compared to tumors derived from control animals, everolimus-treated animals show lower tumor uptake by 44% ($P = 0.0005$). (D) Biodistribution data from non-tumor tissues collected from control animals after the baseline scans (pretreatment) and from treated animals after the second scanning sequence (posttreatment). Data are expressed as percentage of the injected dose per gram of tissue (%ID/g).
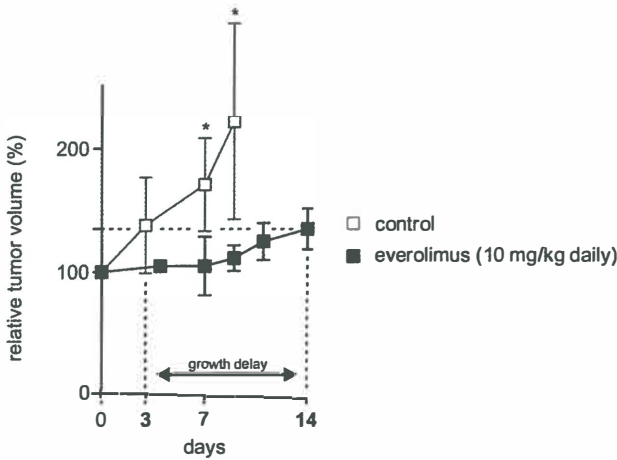
Figure 4 | Tumor size determined by caliper measurements in everolimus-treated animals compared to controls (untreated A2780[luc+] xenograft-bearing mice) (17). The point of reference is set at day 0, the last day of the baseline scanning sequence after which everolimus administration was started. After 7 days of everolimus treatment, the tumors were smaller in treated animals *versus* controls. Control animals had to be terminated at day 9 because of excessive tumor outgrowth.

DISCUSSION

This study shows that *in vivo* serial [89]Zr-bevacizumab PET imaging can visualize reduced tumor VEGF-A levels upon treatment with everolimus in an ovarian cancer xenograft model.

The relatively modest activity of temsirolimus observed in ovarian cancer patients underscores the need for patient selection. Responses limited to a subset of ovarian cancer patients have also been observed with VEGF(R)-targeted antiangiogenic drugs, as well as several other targeted agents, and could result from marked molecular heterogeneity which is characteristic to ovarian cancer. (27,28) The discovery of biomarkers for (early) response prediction might permit the selection of patients that are likely to benefit from single-agent mTOR inhibition or mTOR inhibitor-based combination regimens. Several proteins involved in mTOR signaling have been proposed as suitable biomarkers for response. Phosphorylation of mTOR in ovarian cancer specimens is a poor indicator of its kinase activity. (5) Phosphorylation of downstream target proteins (e.g. p70S6K, S6 and 4E-BP1) is a better read-out for mTOR activity and has been used to check for effective drug delivery and optimal biologic dosing in phase I clinical trials with everolimus. (20,29) Utilizing these protein expression levels as biomarkers for response is hampered by the need for (repeat) tumor tissue acquisition, or the use of surrogate tissues such as peripheral blood mononuclear cells (PBMCs), skin or hair follicles. Instability of phosphorylated proteins further challenges the reliability (and reproducibility) of such analyses. (30)
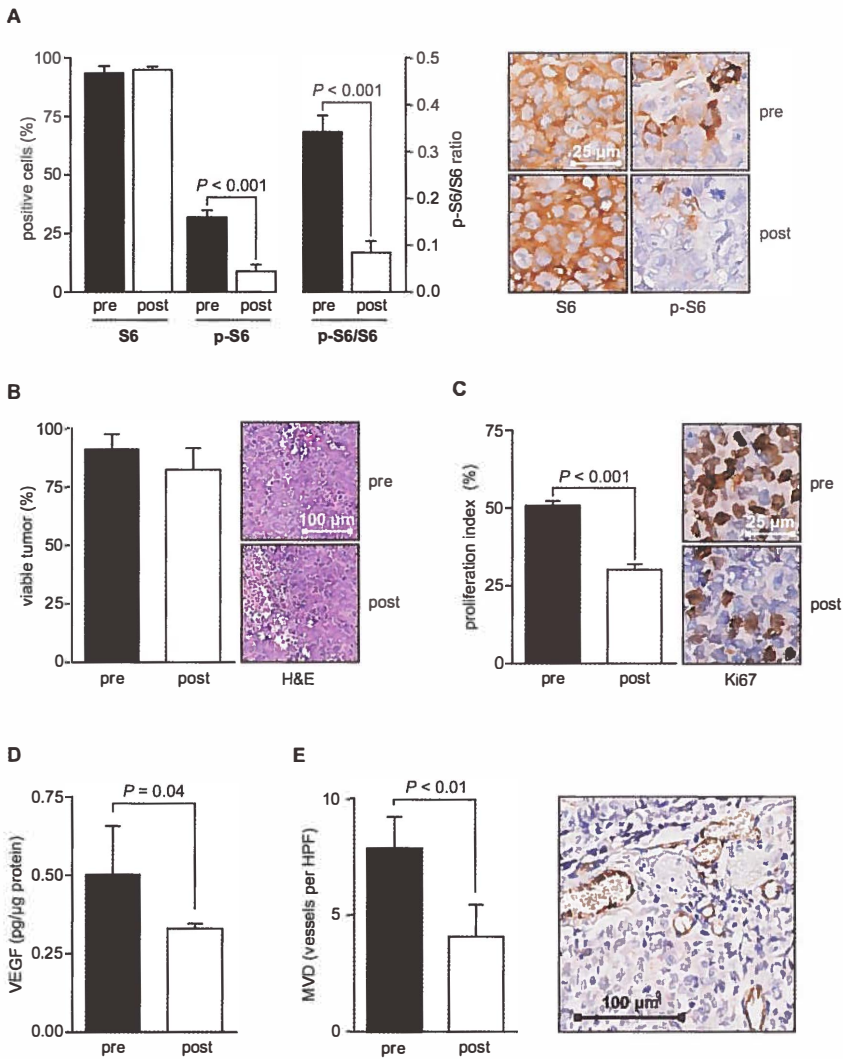
Figure 5 I (A) S6 expression was homogeneously present in > 90% of tumor cells, while p-S6 was heterogeneously expressed. Everolimus treatment did not change total S6 expression, while p-S6 expression was significantly reduced in treated *versus* control tumors ($P < 0.001$). There was a marked decrease in the ratio between p-S6/S6, which was determined for each individual tumor. (B) Tumor viability is expressed as the percentage of viable tumor tissue within the total surface area analyzed. No significant differences in tumor viability were observed between treated and control tumors. (C) The proliferation index is expressed as the percentage of nuclei positive for Ki67. Compared to control tumors, everolimus treatment reduced the proliferating fraction by 41% ($P < 0.001$). (D) VEGF-A levels determined in whole-tumor lysates show reduced VEGF-A in everolimus-treated *versus* control tumors ($P = 0.04$). VEGF-A levels are expressed relative to the total protein content of each lysate, to correct for loading differences. (E) MVD, presented as the average number of vWF positive vessels per high-power field (HPF), was reduced in treated *versus* control tumors (48% decrease, $P < 0.01$). A representative picture is included which shows an angiogenic area in a control tumor, showing specific staining of tumor vasculature.

In vivo molecular imaging provides an attractive alternative. It allows for whole-body, non-invasive monitoring of tumor biology and changes herein resulting from drug administration. These techniques are being explored as tools for patient selection for several molecular targeted drugs, including mTOR inhibitors. Thus far, ^{18}F-fluorodeoxyglucose PET (FDG-PET) measuring tumor glucose metabolism has received most attention. (31,32) Inhibition of mTOR does indeed reduce glucose uptake by reducing glucose transporter 1 (GLUT1) expression and/or hexokinase activity. (33) However, changes in FDG-PET according to EORTC criteria did not correlate with radiographic response according to RECIST criteria or progression-free survival in 34 patients with different cancer types treated with rapamycin. (31)

Given the role of mTOR in angiogenesis, we instead monitored the downstream effect of mTOR inhibition by everolimus on VEGF-A levels in xenografted ovarian cancers with [89]Zr-bevacizumab PET. Everolimus treatment resulted in reduced [89]Zr-bevacizumab tumor uptake, which coincided with delayed tumor growth, lower tumor VEGF-A protein expression and reduced MVD.

Accumulation of radiolabeled bevacizumab results from its interaction with larger human VEGF-A isoforms bound to (tumor) cell surfaces and extracellular matrix components. (34) For VEGF-A$_{165}$, the most abundant isoform, equilibrium is thought to exist between bound and freely diffusible fractions due to weak binding properties. [89]Zr-bevacizumab PET thus has the potential of not only visualizing presence but also activity of tumor-associated VEGF-A. This is supported by the finding that there was a 48% reduction in tumor vascularity (MVD) after everolimus treatment, demonstrating an antiangiogenic response. These findings are of interest to evaluate in the clinic. [89]Zr-bevacizumab PET is already known to show excellent tracer uptake in tumor lesions of renal cell cancer patients and is currently tested as an early biomarker for response to everolimus in 2 clinical trials (Everol*image*, NCT01028638; NETPET, NCT01338090). (35) Moreover, [89]Zr-bevacizumab PET might provide more insight in differential effects of antiangiogenic drugs on individual tumor lesions within a patient.

It is of interest that we observed a homogeneous decrease in tracer uptake after everolimus treatment based on microPET scans. This was also observed previously with the heat shock protein 90 (HSP90) inhibitor NVP-AUY922. (16) This differs from previous findings with the VEGFR-targeted TKI sunitinib, which acts at the level of the endothelial cells. [89]Zr-ranibizumab, the radiolabeled Fab-fragment derived from bevacizumab, was used to visualize the effect of sunitinib treatment on tumor VEGF-A levels in an ovarian cancer xenograft model. (17) Reduction of tracer uptake was more pronounced in the tumor center *versus* the rim of the tumor. Increased invasiveness was observed in xenograft models treated with sunitinib, and it was speculated that hypoxia (and consequently HIF activity) drives this adaptive response. (36) Lack of differential tracer uptake between tumor center and periphery observed with mTOR or HSP90 inhibitors might reflect their potential to inhibit HIF activity, through reducing its translation or stability.

Our results provide a proof-of-principle of using [89]Zr-bevacizumab PET to monitor reduction of tumor VEGF-A levels in response to antiangiogenic treatment with everolimus. The *in vivo* experiments were performed

5

in a subcutaneous human ovarian cancer xenograft. The sensitivity (resolution) of PET scanning requires a minimum volume and minimum of tracer uptake to detect and quantify any individual tumor lesion. This hampers tumor visualization and quantification of tracer uptake in small tumor lesions, certainly when trying to visualize disseminated disease in the peritoneal cavity of small animals such as mice. Clinical studies are needed to determine whether this imaging modality would also allow visualization of VEGF-A levels in patients with widespread disseminated, intraperitoneal disease.

Collectively, our data demonstrate that [89]Zr-bevacizumab PET provides a novel tool for non-invasive monitoring of antiangiogenic effects upon mTOR inhibitor therapy. It provides an interesting candidate biomarker in cancers in which angiogenesis inhibition is thought to underlie treatment efficacy, like ovarian cancer. Our results support the evaluation of [89]Zr-bevacizumab PET to measure tumor VEGF-A levels as an early biomarker for antiangiogenic efficacy of mTOR inhibitor therapy in clinical studies.

**Disclosure of potential conflicts of interest**
None to disclose.

REFERENCES

1. Jemal A, Bray F, Center MM, Ferlay J, Ward E, Forman D. Global cancer statistics. CA Cancer J Clin 2011;61:69-90.

2. Burger RA, Brady MF, Bookman MA, Fleming GF, Monk BJ, Huang H, et al. Incorporation of bevacizumab in the primary treatment of ovarian cancer. N Engl J Med 2011;365:2473-83.

3. Perren TJ, Swart AM, Pfisterer J, Ledermann JA, Pujade-Lauraine E, Kristensen G, et al. A phase 3 trial of bevacizumab in ovarian cancer. N Engl J Med 2011;365:2484-96.

4. Altomare DA, Wang HQ, Skele KL, De Rienzo A, Klein-Szanto AJ, Godwin AK, et al. AKT and mTOR phosphorylation is frequently detected in ovarian cancer and can be targeted to disrupt ovarian tumor cell growth. Oncogene 2004;23:5853-7.

5. No JH, Jeon YT, Park IA, Kim YB, Kim JW, Park NH, et al. Activation of mTOR signaling pathway associated with adverse prognostic factors of epithelial ovarian cancer. Gynecol Oncol 2011;121:8-12.

6. Ma XM, Blenis J. Molecular mechanisms of mTOR-mediated translational control. Nat Rev Mol Cell Biol 2009;10:307-18.

7. Skinner HD, Zheng JZ, Fang J, Agani F, Jiang BH. Vascular endothelial growth factor transcriptional activation is mediated by hypoxia-inducible factor 1alpha, HDM2, and p70S6K1 in response to phosphatidylinositol 3-kinase/AKT signaling. J Biol Chem 2004;279:45643-51.

8. Lane HA, Wood JM, McSheehy PM, Allegrini PR, Boulay A, Brueggen J, et al. mTOR inhibitor RAD001 (everolimus) has antiangiogenic/vascular properties distinct from a VEGFR tyrosine kinase inhibitor. Clin Cancer Res 2009;15:1612-22.

9. Mabuchi S, Altomare DA, Connolly DC, Klein-Szanto A, Litwin S, Hoelzle MK, et al. RAD001 (Everolimus) delays tumor onset and progression in a transgenic mouse model of ovarian cancer. Cancer Res 2007;67:2408-13.

10. Mabuchi S, Altomare DA, Cheung M, Zhang L, Poulikakos PI, Hensley HH, et al. RAD001 inhibits human ovarian cancer cell proliferation, enhances cisplatin-induced apoptosis, and prolongs survival in an ovarian cancer model. Clin Cancer Res 2007;13:4261-70.

11. Mabuchi S, Kawase C, Altomare DA, Morishige K, Sawada K, Hayashi M, et al. mTOR is a promising therapeutic target both in cisplatin-sensitive and cisplatin-resistant clear cell carcinoma of the ovary. Clin Cancer Res 2009;15:5404-13.

12. Miyazawa M, Yasuda M, Fujita M, Kajiwara H, Hirabayashi K, Takekoshi S, et al. Therapeutic strategy targeting the mTOR-HIF-1 alpha-VEGF pathway in ovarian clear cell adenocarcinoma. Pathol Int 2009;59:19-27.

13. Huynh H, Teo CC, Soo KC. Bevacizumab and rapamycin inhibit tumor growth in peritoneal model of human ovarian cancer. Mol Cancer Ther 2007;6:2959-66.

14. Behbakht K, Sill MW, Darcy KM, Rubin SC, Mannel RS, Waggoner S, et al. Phase II trial of the mTOR inhibitor, temsirolimus and evaluation of circulating tumor cells and tumor biomarkers in persistent and recurrent epithelial ovarian and primary peritoneal malignancies: A Gynecologic Oncology Group study. Gynecol Oncol 2011;123:19-26.

15. Nagengast WB, De Vries EG, Hospers GA, Mulder NH, De Jong JR, Hollema H, et al. In vivo VEGF imaging with radiolabeled bevacizumab in a human ovarian tumor xenograft. J Nucl Med 2007;48:1313-9.

16. Nagengast WB, De Korte MA, Oude Munnink TH, Timmer-Bosscha H, Den Dunnen WF, Hollema H, et al. [89]Zr-bevacizumab PET of early antiangiogenic tumor response to treatment with HSP90 inhibitor NVP-AUY922. J Nucl Med 2010;51:761-7.

17. Nagengast WB, Lub-De Hooge MN, Oosting SF, Den Dunnen WF, Warnders FJ, Brouwers AH, et al. VEGF-PET imaging is a noninvasive biomarker showing differential changes in the tumor during sunitinib treatment. Cancer Res 2011;71:143-53.

5

18. Duiker EW, De Vries EG, Mahalingam D, Meersma GJ, Boersma-Van Ek W, Hollema H, et al. Enhanced antitumor efficacy of a DR5-specific TRAIL variant over recombinant human TRAIL in a bioluminescent ovarian cancer xenograft model. Clin Cancer Res 2009;15:2048-57.

19. O'Reilly T, McSheehy PM, Kawai R, Kretz O, McMahon L, Brueggen J, et al. Comparative pharmacokinetics of RAD001 (everolimus) in normal and tumor-bearing rodents. Cancer Chemother Pharmacol 2010;65:625-39.

20. O'Donnell A, Faivre S, Burris HA, Rea D, Papadimitrakopoulou V, Shand N, et al. Phase I pharmacokinetic and pharmacodynamic study of the oral mammalian target of rapamycin inhibitor everolimus in patients with advanced solid tumors. J Clin Oncol 2008;26:1588-95.

21. Honer M, Ebenhan T, Allegrini PR, Ametamey SM, Becquet M, Cannet C, et al. Anti-angiogenic/vascular effects of the mTOR inhibitor everolimus are not detectable by FDG/FLT-PET. Transl Oncol 2010;3:264-75.

22. Cejka D, Kuntner C, Preusser M, Fritzer-Szekeres M, Fueger BJ, Strommer S, et al. FDG uptake is a surrogate marker for defining the optimal biological dose of the mTOR inhibitor everolimus in vivo. Br J Cancer 2009;100:1739-45.

23. Bradford MM. A rapid and sensitive method for the quantitation of microgram quantities of protein utilizing the principle of protein-dye binding. Anal Biochem 1976;72:248-54.

24. Duiker EW, Meijer A, Van der Bilt AR, Meersma GJ, Kooi N, Van der Zee AG, et al. Drug-induced caspase 8 upregulation sensitises cisplatin-resistant ovarian carcinoma cells to rhTRAIL-induced apoptosis. Br J Cancer 2011;104:1278-87.

25. Stollman TH, Scheer MG, Leenders WP, Verrijp KC, Soede AC, Oyen WJ, et al. Specific imaging of VEGF-A expression with radiolabeled anti-VEGF monoclonal antibody. Int J Cancer 2008;122:2310-4.

26. Loening AM, Gambhir SS. AMIDE: a free software tool for multimodality medical image analysis. Mol Imaging 2003;2:131-7.

27. Gershenson DM. The heterogeneity of epithelial ovarian cancer: getting it right. Cancer 2010;116:1400-2.

28. Gourley C, Michie CO, Keating KE, Deharo S, O'Brien EJ, Winter A, et al. Establishing a molecular taxonomy for epithelial ovarian cancer (EOC) from 363 formalin-fixed paraffin embedded (FFPE) specimens. J Clin Oncol 2011;29s:abstr 5000.

29. Tanaka C, O'Reilly T, Kovarik JM, Shand N, Hazell K, Judson I, et al. Identifying optimal biologic doses of everolimus (RAD001) in patients with cancer based on the modeling of preclinical and clinical pharmacokinetic and pharmacodynamic data. J Clin Oncol 2008;26:1596-602.

30. Baker AF, Dragovich T, Ihle NT, Williams R, Fenoglio-Preiser C, Powis G. Stability of phosphoprotein as a biological marker of tumor signaling. Clin Cancer Res 2005;11:4338-40.

31. Ma WW, Jacene H, Song D, Vilardell F, Messersmith WA, Laheru D, et al. (18F)fluorodeoxyglucose positron emission tomography correlates with Akt pathway activity but is not predictive of clinical outcome during mTOR inhibitor therapy. J Clin Oncol 2009;27:2697-704.

32. Kinross KM, Brown DV, Kleinschmidt M, Jackson S, Christensen J, Cullinane C, et al. In vivo activity of combined PI3K/mTOR and MEK inhibition in a KrasG12D;Pten deletion mouse model of ovarian cancer. Mol Cancer Ther 2011;10:1440-9.

33. Wei LH, Su H, Hildebrandt IJ, Phelps ME, Czernin J, Weber WA. Changes in tumor metabolism as readout for mammalian target of rapamycin kinase inhibition by rapamycin in glioblastoma. Clin Cancer Res 2008;14:3416-26.

34. Stollman TH, Scheer MG, Franssen GM, Verrijp KN, Oyen WJ, Ruers TJ, et al. Tumor accumulation of radiolabeled bevacizumab due to targeting of cell- and matrix-associated VEGF-A isoforms. Cancer Biother Radiopharm 2009;24:195-200.

35. Oosting SF, Nagengast WB, Oude Munnink TH, Lub-De Hooge MN, Brouwers AH, Glaudemans AWJM, et al. [89]Zr-bevacizumab PET imaging in renal cell carcinoma patients: feasibility of tumor VEGF quantification. Eur J Cancer Suppl 2010;8:72-3.

36. Paez-Ribes M, Allen E, Hudock J, Takeda T, Okuyama H, Vinals F, et al. Antiangiogenic therapy elicits malignant progression of tumors to increased local invasion and distant metastasis. Cancer Cell 2009;15:220-31.

5

SUPPLEMENTARY FIGURE
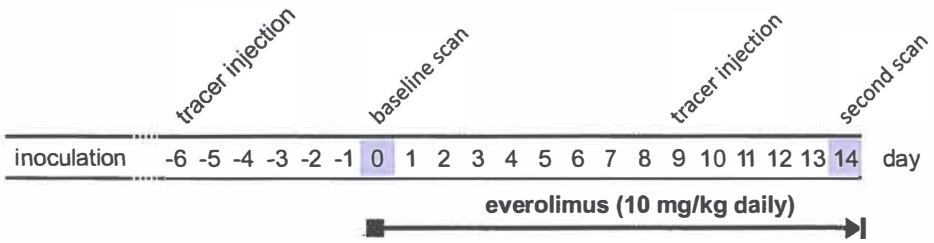
Supplementary Figure S1 | Schematic representation of the study design. The point of reference is set at day 0, at which the baseline scans were performed and everolimus treatment was started consecutively. After the baseline (pretreatment) scans, control animals were sacrificed and biodistribution studies performed. Biodistribution on everolimus-treated animals was performed directly after the second (posttreatment) scans.

CHAPTER 6

Visualizing dual downregulation of IGF-1R and VEGF-A by Hsp90 inhibition effect in triple negative breast cancer

Anton G.T. Terwisscha van Scheltinga[1,2], Paul Berghuis[1],
Hilde H. Nienhuis[1], Hetty Timmer-Bosscha[1], Linda Pot[1],
Sietske B.M. Gaykema[1], Marjolijn N. Lub-de Hooge[2,3],
Jos G.W. Kosterink[2], Elisabeth G.E. de Vries[1], Carolien P. Schröder[1]

[1]Department of Medical Oncology, [2]Department of Hospital and Clinical Pharmacy, [3]Department of Nuclear Medicine and Molecular Imaging, University of Groningen, University Medical Center Groningen, Groningen, The Netherlands.

ABSTRACT

Triple negative breast cancer (TNBC) is biologically characterized by heterogeneous presence of molecular pathways underlying it. Insulin-like growth factor receptor-1 (IGF-1R) expression and vascular endothelial growth factor-A (VEGF-A) have been identified as key factors in these pathways in TNBC. In this study, we aimed at *in vivo* PET imaging the effect of heat shock protein (Hsp) 90 inhibition by means of NVP-AUY922 on these pathways, with zirconium-89 (^{89}Zr) labeled antibodies targeting IGF-1R and VEGF-A.

Methods:

In vitro NVP-AUY922 effects on cellular IGF-1R expression and VEGF-A secretion were determined in MCF-7 and MDA-MB-231 cell lines. Moreover human TNBC bearing MDA-MB-231 mice received 50 mg/kg NVP-AUY922 or vehicle q3d intraperitoneally for 21 days. PET scans with ^{89}Zr-MAB391 and ^{89}Zr-bevacizumab for visualization of IGF-1R and VEGF-A were performed before and during treatment. *Ex vivo* biodistribution and correlative tissue analyses were performed.

Results:

NVP-AUY922 treatment reduced IGF-1R expression and VEGF-A excretion in both cell lines. Hsp90 inhibition lowered tumor uptake on ^{89}Zr-MAB391-PET by 37.3% (P < 0.01) and on ^{89}Zr-bevacizumab-PET by 44.4% (P < 0.01). This was confirmed by *ex vivo* biodistribution with a reduction of 41.3 % injected dose (ID)/g for ^{89}Zr-MAB391 and 37.8 %ID/g for ^{89}Zr-bevacizumab, while no differences were observed for other tissues. This coincided with reduced IGF-1R expression and mean vessel density in the NVP-AUY922 treated tumors.

Conclusion:

^{89}Zr-MAB391 and ^{89}Zr-bevacizumab PET reflect effect of Hsp90 inhibitors and can therefore potentially be used to monitor therapeutic effects of Hsp90 inhibitor therapy in TNBC.

INTRODUCTION

Triple negative breast cancer (TNBC) accounts for ~15% of the invasive breast cancers. (1) These tumors lack estrogen receptor (ER), progesterone receptor (PR) and human epidermal growth factor receptor (HER) 2 expression. TNBC has an aggressive phenotype with an affinity for onset at premenopausal age, early dissemination and high frequency of relapse. Regardless of disease stage, women with TNBC have a worse survival than other breast cancer patients. (2) Breast cancers found in BRCA1 mutation carriers are frequently triple negative and basal like. Effective systemic treatment is limited to chemotherapy and this type of breast cancer lacks effective targeted treatment for standard use. (1-2) The search for effective targeted agents has been hampered by the heterogeneous presence of molecular mechanisms in TNBC, which is much more complex compared to other breast cancer types. (1-2) It is unlikely that one driver process can be identified and targeted in this setting, to produce a straightforward effective anti-tumor treatment. Moreover, much effort is ongoing with sophisticated techniques to identify relevant pathways in TNBC. Insulin-like growth factor receptor-1 (IGF-1R) and vascular endothelial growth factor-A (VEGF-A) which regulates angiogenesis are key factors in these pathways. (3-4) IGF-1R is important for tumor growth and survival and plays a major role in the multistep metastatic process where it regulates migration, invasion and angiogenesis. (5)

Therefore an agent with a broad spectrum anti-tumor activity, is of interest in TNBC. Targeting heat shock protein 90 (Hsp90) allows such a broad focus, by inhibiting multiple pathways in cancer. Hsp90 is a widely expressed molecular chaperone, required for proper folding and activation of a multitude of key oncogenic proteins. (6) Hsp90 supports in tumor cells the activated or metastasizing forms of oncoproteins and buffers cellular stresses induced by the malignant environment. (7) Hsp90 client proteins such as IGF-1R, hypoxia-inducible factor 1α (HIF-1α), epidermal growth factor receptor (EGFR) and HER2, are involved in all hallmarks of cancer, including tumor cell growth, invasion, metastasis and angiogenesis. (8-9) VEGF is a downstream product of various Hsp90 client proteins. All of these processes are potentially affected by Hsp90 inhibition, and Hsp90 inhibitors are currently among the most actively pursued cancer drug targets by the pharmaceutical industry.

This rationale for Hsp90 inhibition in TNBC, is supported by two preclinical studies which showed efficacy in TNBC models. (10-11) Clinical trials have so far focused on non-TNBC subtypes with well known Hsp90 client proteins, such as HER2 overexpressing breast cancer. Absence of clinical trials in TNBC might be related to the lack of biomarkers for Hsp90 inhibition effect in TNBC. Molecular imaging *in vivo*, a technique that is also applicable in the human setting, can be used to examine Hsp90 targets as potential biomarkers.

In the present study, we have therefore visualized dual therapeutic effects in TNBC that can be influenced by Hsp90 inhibition with NVP-AUY922 *in vitro* and *in vivo*, namely IGF-1R expression and angiogenesis, driven by VEGF-A.

6

MATERIALS AND METHODS

Cell lines and reagents

Cell lines MCF-7 and MDA-MB-231 cells were purchased from the American Type Culture Collection (ATCC). They were cultured in RPMI 1640 and DMEM (Gibco) respectively, supplemented with 10% fetal calf serum (FCS) (Sanbio) in a humidified atmosphere with 5% CO_2 at 37 °C. MDA-MB-231 medium was in addition supplemented with 1 mM glutamine. MCF-7 was used as a positive control cell line for high IGF-1R expression, MDA-MB-231 cells were chosen as TNBC cell line model with intermediate IGF-1R expression.

Recombinant human IGF-1 was purchased from R&D systems. NVP-AUY922 was provided by Novartis Pharma AG. NVP-AUY922 was dissolved in DMSO and stored at -80 °C for *in vitro* experiments. For intraperitoneal (ip) administration, NVP-AUY922 was dissolved in 5% glucose. The IGF-1R antibody MAB391 (R&D Systems) and bevacizumab (Roche) were used for *in vivo* imaging of IGF-1R and VEGF-A respectively.

SDS-polyacrylamide gel electrophoresis and Western blotting

Cells were lyzed in M-PER (Thermo Scientific) according to the manufacturer's instructions and standard Western blot sample buffer (50 mM Tris/HCl, pH 6.8, 2% SDS, 10% glycerol, 5% 2-β-mercaptoethanol) was added. Samples were boiled for 5 minutes. Total cell lysates were size fractionated on sodium dodecyl sulfate-polyacrylamide gel electrophoresis (SDS-PAGE) and transferred onto activated polyvinylidene difluoride membranes (Millipore). Protein concentration was determined according to Bradford. Membranes were blocked in 5% bovine serum albumin (BSA) in Tris-HCl buffer (50 mM, pH 7.4) containing 0.1% Tween-20 for 1 hour and exposed to primary antibodies (anti-IGF-1R; Cell Signaling Technology) and mouse anti-β-actin (Sigma-Aldrich). Binding of antibodies was determined using horseradish peroxidase (HRP)-conjugated secondary antibodies (DAKO) and visualized with the Lumi-light plus kit of Roche Diagnostics.

Conjugation and radiolabeling of MAB391, bevacizumab and IgG

Conjugation and radiolabeling of MAB391 and bevacizumab were performed as described earlier. (12-13) Briefly, MAB391 and bevacizumab were first conjugated with the chelator tetrafluorphenol N-succinyldesferal (TFP-N-sucDf), which was kindly provided by Dr. G.A. van Dongen (VU Medical Center, Amsterdam, the Netherlands). After conjugation, the product was purified by ultracentrifugation and stored at −20 °C. In the second step, the conjugated MAB391 and bevacizumab were radiolabeled with zirconium-89 ([89]Zr) (IBA Molecular).

Human IgG (Sanquin) conjugation and labeling were performed according to Ruegg *et al*. (14) IgG was first conjugated to the bifunctional conjugating agent 2-(4-isothiocyanatobenzyl)-diethylenetriaminepentaacetic acid (p-SCN-Bn-DTPA, Macrocyclics). After conjugation, the product was stored at −20 °C. Conjugated human IgG was radiolabeled with indium-111 (^{111}In) chloride (Covidien).

In vitro assays evaluating Hsp90 inhibition effect on IGF-1R and VEGF-A expression

To examine the IGF-1R expression on cell membranes, flow cytometry analyses were performed on MCF-7 and MDA-MB231 cells. Attached cells were incubated with 100, 200 or 300 nM NVP-AUY922 and thereafter harvested, washed and diluted in cold PBS. Cells were incubated for 1 hour with MAB391 (10 µg/mL) followed by 1 hour with 10 µg/mL monoclonal anti-mouse IgG, labeled with PE. Membrane receptor expression was analyzed using flow cytometry (FACSCalibur, Becton Dickinson) with Winlist software. For every treatment condition, three independent experiments were performed.

A radio-immuno assay was performed by incubating attached cells with 100, 200 or 300 nM NVP-AUY922 for 24 hours. Cells were harvested, washed and diluted in cold PBS. For each condition, 1×10^6 cells were incubated in triplicate with 5 ng ^{89}Zr-MAB391 at 4 °C. To correct for aspecific binding, a sample of untreated cells was blocked with a 200-fold excess of unlabeled MAB391. Binding of ^{89}Zr-MAB391 was measured in a calibrated well-type LKB-1282-Compu-gamma system (LKB Wallac). For every treatment condition, three independent experiments were performed.

VEGF-A levels were determined in supernatant of MCF-7 and MDA-MB-231 cells after 24 hours incubation with Hsp90 inhibitor NVP-AUY922. Cell culture supernatant was removed and centrifuged for 15 minutes at 450 g, to remove any residual cells or cell remnants, and subsequently stored in aliquots at -20 °C. VEGF-A levels were measured with VEGF enzyme-linked immunosorbent assay (ELISA) according to manufacturer's instructions (Quantikine, R&D Systems). The absorbance of each well was measured by microplate reader (Bio Rad Benchmark) at a wavelength of 450 nm. Wavelength correction was performed by subtracting measurements at 595 nm from the 450 nm readings.

^{89}Zr-MAB391 and ^{89}Zr-bevacizumab tracer validation and imaging in TNBC tumors

Tumor cells for xenografting were harvested by trypsinization and resuspended in medium. Mice were injected subcutaneously (sc) with 5×10^6 MCF-7 or MDA-MB-231 cells in 0.3 mL in medium and Matrigel™ (BD Bioscience). MCF-7 tumor bearing mice received one day prior to tumor inoculation a 17β-estradiol pellet (0.18 mg, 90-day release; Innovative Research of America) which was implanted sc in the neck region to support tumor growth. *In vivo* imaging and *ex vivo* experiments were conducted using male nude Balb-c mice (Balb/cOlaHSD-foxn^{nu}) obtained from Harlan Nederland.

^{89}Zr-MAB391 tracer validation was performed in MCF-7 (n=6) and MDA-MB-231 (n=6) tumor bearing mice. Mice received 10 µg ^{89}Zr-MAB391 and 10 µg ^{111}In-IgG as aspecific control via intravenous (iv) injection. The tested protein tracer dose of 10 µg was chosen based on previous IGF-1R antibody imaging results (15), showing specific tumor uptake without completely saturating the target. MCF-7 and MDA-MB-231 tumor bearing mice showed specific IGF-1R expression driven tumor uptake of ^{89}Zr-MAB391. Animals were imaged using a MicroPET Focus 220 rodent scanner (CTI Siemens) at 24, 72 and 144 hours after tracer injection followed by *ex vivo* biodistribution. This revealed excellent tumor uptake in all 12 mice. Tumor uptake could

6

already be demonstrated 24 hours after [89]Zr-MAB391 administration, even though blood-pool and liver activity were still dominant at this time point (Supplementary Fig. S1A, B). From days 1-6, tumor uptake increased in both MCF-7 and MDA-MB-231 tumors, whereas blood-pool and liver uptake decreased. The data is presented as the mean standard uptake value (SUVmean). MCF-7 tumors obtained a tumor SUVmean of 1.7, MDA-MB-231 a SUVmean of 0.9 of [89]Zr-MAB391. *Ex vivo* biodistribution confirmed microPET findings with tumor uptake of 10.4 and 7.3 %ID/g for MCF-7 and MDA-MB-231 tumors respectively (Supplementary Fig. S1A, B). Liver uptake of MAB391 was relatively high, and a difference in liver uptake was found in mice bearing MCF-7 and MDA-MB-231 tumors of 10.8 %ID/g and 15.8 %ID/g respectively. As a result of this, antibody blood levels were different between MAB391 and IgG. To compare specific versus non specific tumor uptake with ^{111}In-IgG, tumor-to-blood ratios were calculated. Higher tumor-to-blood ratios were found for both MCF-7 and MDA-MB231 tumors for [89]Zr-MAB391 compared to ^{111}In-IgG (Supplementary Fig. S1C). Based on these results the 10 µg protein tracer dose was used for the treatment monitoring experiments with Hsp90 inhibition.

[89]Zr-bevacizumab was validated previously. (13) To determine the uptake in MDA-MB-231 tumors, 6 animals were injected with 10 µg [89]Zr-bevacizumab and 10 µg ^{111}In-IgG and scanned at 144 hours after injection of the tracer. Biodistribution was performed afterwards.

In vivo molecular imaging model evaluating Hsp90 inhibition effect on IGF-1R and VEGF-A

Mice received a tracer injection and underwent a microPET scan 144 hours after tracer injection before and during treatment. Mice received 22 days after inoculation co-injection of 10 µg [89]Zr-bevacizumab or [89]Zr-MAB391 with 10 µg IgG. Following the first scan week, mice received treatment with 50 mg/kg NVP-AUY922 or vehicle every-third-day (q3d) administrated ip. The second scan week was initiated after 2 weeks of treatment. Mice received again 10 µg [89]Zr-bevacizumab or [89]Zr-MAB391, now with 10 µg ^{111}In-IgG as aspecific control. *Ex vivo* biodistribution studies were performed after the second scan week, which was after 3 weeks of treatment.

After PET image reconstruction, *in vivo* quantification was performed with AMIDE Medical Image Data Examiner software (version 0.9.1, Stanford University, Stanford, CA). (16) Animals were sacrificed after the last scan and organs and tissues were excised and weighed. Samples and primed standards were counted for radioactivity in a calibrated well-type LKB-1282-Compu-gamma system (LKB Wallac) and corrected for physical decay. *Ex vivo* tissue activity is expressed as percentage of the injected dose per gram tissue (%ID/g). Harvested tumors were paraffin embedded for further analysis.

All animal experiments were performed with isoflurane inhalation anesthesia (induction 3%, maintenance 1.5%). The animal experiments were approved by the Institutional Animal Care and Use Committee of the University of Groningen.

Ex vivo tissue analysis

Slices (3 μm thick) were cut from paraffin-embedded tumor sections using a microtome and placed on glass slides. Heat-induced antigen retrieval was performed in 10 mM citrate buffer (IGF-IRβ) or Tris/EDTA (Ki67) using a 400 W rotary microwave, or by using proteinase K at room temperature. Endogenous peroxidase was blocked by 30 minutes incubation with 0.3% H_2O_2 in PBS. Endogenous avidin/biotin activity was blocked using a commercially available blocking kit (Vector Laboratories). Slides were incubated with primary antibody detecting Ki67 (Dako) or IGF-1Rβ (Cell Signaling). In addition, slides were stained with anti-von Willebrand factor antibody (vWF) (Dako) to determine the mean vascular density (MVD). Staining was visualized after incubation with biotinylated or peroxidase-bound secondary antibodies (Dako) using, when necessary, the streptavidin-biotin/horseradish peroxidase complex (Dako) and 3,3'-diaminobenzidine (Sigma-Aldrich). Hematoxylin counterstaining was applied routinely and hematoxylin & eosin (H&E) staining served to analyze tissue viability and morphology.

Stainings were quantified by evaluation of 100 cells in 3 high-power fields (400x magnification) using a calibrated grid, counting positive and negative nuclei (Ki67). Data is expressed as the percentage of positive cells. MVD was determined by counting the number of vessels within at least 3 angiogenic hot-spots as described previously (17). Immunohistochemistry results of IGF-1Rβ were scored semi-quantitatively according to the system used in clinical testing (0, 1, 2 and 3+, which corresponds with no, weak, moderate or strong staining). Photographs were acquired by Leica Application Suite (Version 3.7) or by digitalized scanning of slides using the NanoZoomer 2.0-HT multi-slide scanner (Hamamatsu). To calculate tumor viability, acquired images from H&E stained slides were analyzed using NanoZoomer Digital Pathology (NDP) viewer software (Hamamatsu).

Statistical analysis

Data are presented as mean ± SD. Statistical analysis was performed using the Mann-Whitney test for non-parametric data and a paired sampled t test for paired data (GraphPad Prism, version 5). Differences were considered significant when $P < 0.05$.

RESULTS

Hsp90 inhibition effects *in vitro* on IGF-1R and VEGF-A

NVP-AUY922 treatment for 24 hours with 300 nM resulted in an 87.9% downregulation of IGF-1R in MCF-7 cells and an 86.1% downregulation in MDA-MB-231 cells in FACS experiments (Fig. 1A). Similar results were found with [89]Zr-MAB391 (Fig. 1B). NVP-AUY922 treatment at 300 nM for 24 hours down-regulated IGF-1R 84.8% in MCF-7 and 84.5% in MDA-MB-231 cells. Excess of unlabeled MAB391 reduced [89]Zr-MAB391 uptake to 1.1% non-specific uptake in MCF-7 and 0.9% in MDA-MB-231 cells. NVP-AUY922 reduced IGF-

1R expression in both cell lines, with undetectable IGF-1R levels at a concentration of 200 nM (Fig. 1C). In a 24 hours pretreatment IGF-1R recovery experiment, NVP-AUY922 (500 nM) reduced the levels of IGF-1R in both cell lines and recurrence of detectable IGF-1R protein expression was observed after 48 hours (Fig. 1D).

In both cell lines NVP-AUY922 treatment reduced VEGF-A excretion dose dependently. MDA-MB-231 cells excreted more VEGF-A in the medium following 24 hours NVP-AUY922 treatment, compared to MCF-7 cells (Fig. 2).

Visualization of dual downregulation of IGF-1R and VEGF-A by NVP-AUY922 in TNBC

Tumor uptake of ^{89}Zr-MAB391 was lowered by 37.3% (P < 0.01) after 3 weeks of treatment with 50 mg/kg NVP-AUY922 every-third-day. In the vehicle treated mice ^{89}Zr-MAB391 tumor uptake before and 21 days after vehicle treatment was not affected (Fig. 3A). These *in vivo* imaging data were supported by *ex vivo* biodistribution data (Fig. 3A). ^{89}Zr-MAB391 tumor uptake was 41.3% (P < 0.01) lower in NVP-AUY922–treated versus vehicle-treated animals. The difference between the control and treated animals was 47.1% (P < 0.01). There was no difference between the tumor uptake in the control group where mice were sacrificed after the baseline scan versus the vehicle group of which the mice were sacrificed after the second scan week (P = 0.310). Treatment with NVP-AUY922 did not change normal-organ (non-tumor) biodistribution of ^{89}Zr-MAB391. ^{111}In-IgG tumor uptake was consistent in the different groups, showing 3.3 %ID/g in the control group sacrificed after the baseline scan, 3.4 %ID/g in NVP-AUY922 treated mice and 4.0 %ID/g in vehicle treated mice. This indicates that tumor perfusion was unaffected by treatment, and that the difference in ^{89}Zr-MAB391 tumor uptake was therefore due to IGF-1R downregulation.

MicroPET analysis 144 hours after tracer injection showed clear tumor uptake of ^{89}Zr-bevacizumab in MDA-MB-231 TNBC xenograft model (Fig. 3B), supporting the presence of high VEGF levels in this xenograft model. Before treatment of MDA-MB-231 bearing mice, an average tumor SUVmean was 2.41 ± 0.56. ^{89}Zr-bevacizumab tumor uptake as quantified by microPET data analysis, decreased with 44.4% (P < 0.01) after NVP-AUY922 50 mg/kg q3d, compared with pretreatment. In vehicle treated mice, tumor uptake of ^{89}Zr-bevacizumab was not affected, indicating no influence of the time between the scans on tracer tumor uptake (Fig. 3B). These *in vivo* imaging data were also supported by *ex vivo* biodistribution data (Fig. 3B). ^{89}Zr-bevacizumab tumor uptake was 37.8% (P < 0.01) lower in NVP-AUY922–treated versus vehicle-treated animals. The difference between the control mice sacrificed after the baseline scan and treated animals sacrificed after the second scan period was 48.1% (P < 0.01). There was no difference between the tumor uptake in the mice of the control group versus the mice of vehicle group (P < 0.05). ^{111}In-IgG tumor uptake was in all groups consistent, indicating that tumor perfusion was unaffected by treatment, and that the difference in ^{89}Zr-bevacizumab tumor uptake was therefore due to VEGF-A downregulation.
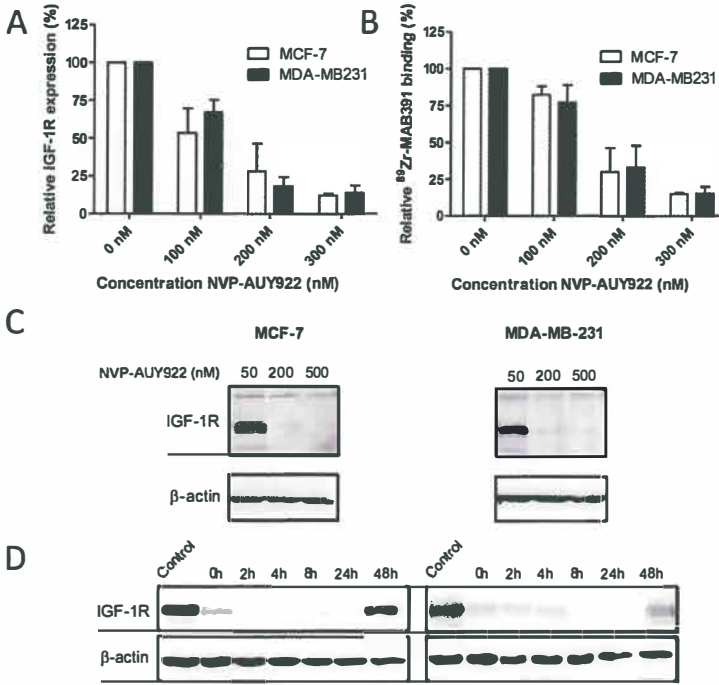
Figure 1 | Reduced IGF-1R expression after NVP-AUY922 treatment. IGF-1R membrane expression is decreased after Hsp90 inhibition in ER-positive MCF-7 and TNBC MDA-MB-231 cells (A). Tumor cell uptake of ^{89}Zr-MAB391 is reduced after treatment with NVP-AUY922 (B). Western blot of total IGF-1R after Hsp90 inhibition (C). Cells were pretreated with increasing dose of NVP-AUY922 for 24 hours. NVP-AUY922 reduced IGF-1R levels at a concentration of 200 nM in both MCF-7 cells and MDA-MB-231. Recovery of IGF-1R expression after cessation of treatment occurred 48 hours after NVP-AUY922 (500 nM) treatment. However, the total IGF-1R levels did not reach initial levels (D).
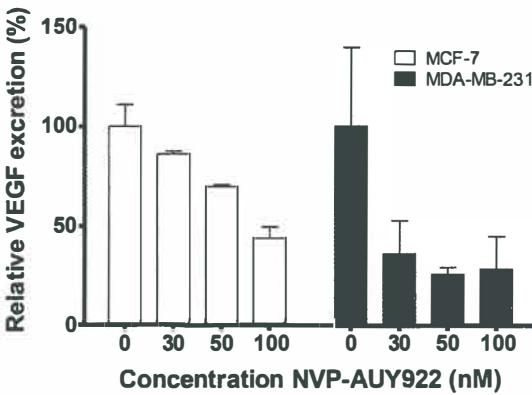
6

Figure 2 | Reduced VEGF-A secretion after NVP-AUY922 treatment. VEGF-A secretion by MCF-7 and MDA-MB-231 cells after treatment with Hsp90 inhibitor NVP-AUY922. Cells were incubated for 24 hours in control medium or in 30, 50 or 100 nM NVP-AUY922 containing medium.
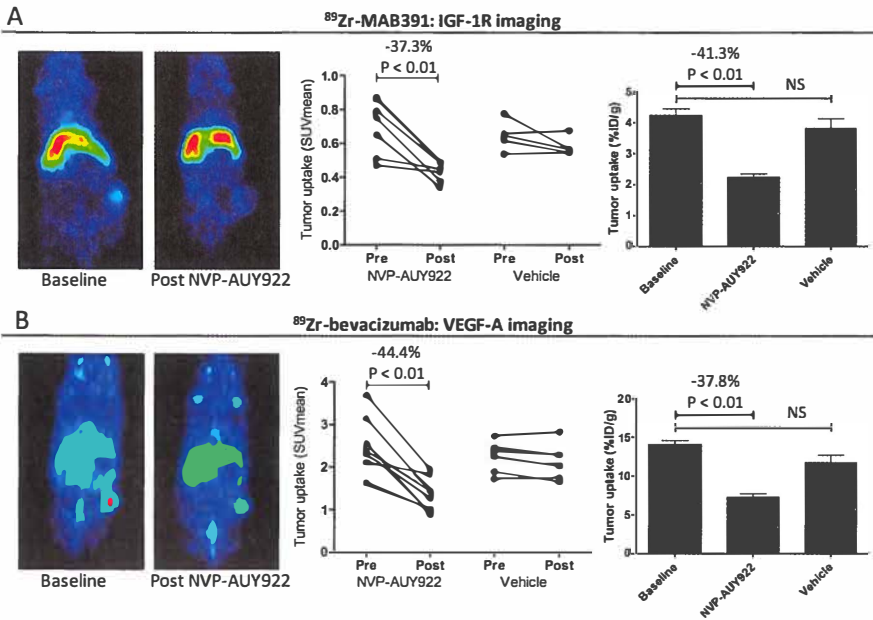
Figure 3 | Visualization of IGF-1R and VEGF-A downregulation after NVP-AUY922 treatment. Hsp90 inhibition effects in TNBC xenograft visualized with ^{89}Zr-MAB391 and ^{89}Zr-bevacizumab. Coronal PET images of representative mice scanned with ^{89}Zr-MAB391 before and after treatment with NVP-AUY-922 (A). PET quantification of ^{89}Zr-bevacizumab tumor uptake at 144 hours post tracer injection in individual animals is shown in B.

Ex vivo tumor analysis supporting in vivo imaging results

H&E stainings showed no differences also not with respect to necrosis in NVP-AUY922 treated animals compared to untreated and control animals. Therefore, decreased ^{89}Zr-MAB391 and ^{89}Zr-bevacizumab tumor uptake in MDA-MB-231 was not due to increased tumor necrosis (Fig. 4).

IGF-1R stainings of tumors obtained from the biodistribution experiments confirmed the IGF-1R downregulation in tumors of the NVP-AUY922 treated mice. All the tumors of the treated mice expressed IGF-1R positive (1+ or 2+), but less intense compared to the control group (Fig. 4). The MVD was lower in NVP-AUY922 treated tumors, indicating decreased angiogenesis. Anti-proliferative effects of NVP-AUY922 were seen in MDA-MB-231 xenografts indicating also an anti-tumor effect (Fig. 4).
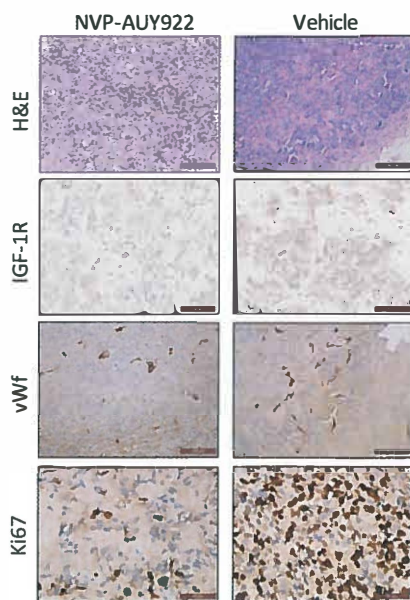
Figure 4 | Ex vivo tissue analysis. Representative H&E, IGF-1R, vWf and Ki67 staining of NVP-AUY922 and vehicle treated MDA-MB-231 xenografts.

DISCUSSION

This study visualized that Hsp90 inhibitor NVP-AUY922 has dual effects on IGF-1R and VEGF-A in TNBC. Molecular imaging of IGF-1R and VEGF-A, as read out biomarker for treatment effect of HSP90 inhibitors, may therefore further support clinical development of these agents in TNBC patients.

An agent with a broad spectrum of anti-tumor activity is of interest in TNBC. Hsp90 inhibitors interact with the N-domain ATP-binding pocket, prevent ATP binding, and stop the chaperone cycle leading to client protein degradation. (6) Following the proof of concept of the Hsp90 inhibitors 17-AAG (tanespimycin) and 17-DMAG (alvespimycin) as geldanamycin analogs, (7) synthetic small-molecule Hsp90 inhibitors were developed to overcome the limitations of these first molecules. The resorcinylic pyrazole/isoxazole amide compound NVP-AUY922, is a potent inhibitor of Hsp90 and reported promising efficacy in breast cancer and non-small cell lung cancer as a single agent and in combination with target therapy in phase II clinical evaluation. (18-19) Biomarkers to predict the effect of, or monitor, Hsp90 inhibition therapy *in vivo*, could support the drug development and selection of patients before start of therapy. (20) Preclinical findings suggest that Hsp70 serum levels could be useful as pharmacodynamic marker of tumor response. (21) Most pharmacodynamic assays to measure Hsp90 inhibition in patients focused on client proteins expressed in peripheral blood mononuclear cells (PBMCs). However, PBMCs showed no predictive value regarding clinical activity or biological response to Hsp90 inhibition in tumor tissue. (22-23) PBMC Hsp70

levels induced by Hsp90 inhibition did also not correlate with clinical response. (24) Hsp90 inhibitors preferentially accumulate in tumor cells instead of normal cells and sensitivity to Hsp90 inhibition between these cell types is fundamentally different. (6) Therefore, it would be preferable to analyze at the tumor level the pharmacodynamic effects of the Hsp90 inhibition. This is possible with molecular imaging. Many oncoproteins are clients of Hsp90. Therefore several more dedicated molecular imaging target opportunities are available for non-invasive monitoring of Hsp90 inhibition.

This is the first study which illustrates that IGF-1R is also *in vivo* a relevant client protein of Hsp90 inhibitors, in TNBC. This combined with the finding that 70-80% of TNBCs express cytoplasmic and membranous IGF-1R, makes IGF-1R an interesting client protein of Hsp90. (25-26) Especially in mutant BRCA1 related TNBC, elevated tumor IGF-1R and IGF-1 levels are found. The current study showed the proof of principle that two effects can be visualized at the tumor level in TNBC. [89]Zr-MAB391 and [89]Zr-bevacizumab PET reflect effect of Hsp90 inhibitors and can therefore potentially be used to monitor therapeutic effects of Hsp90 inhibitor therapy in TNBC. The advantage of using a PET tracer for molecular imaging is that tumor uptake of the tracer can be quantified with PET, this quantification can be used for measurement of treatment effects.

Hsp90 inhibitors exhibit antiangiogenic effects *in vivo*. (17-18) We observed a decreased tumor MVD after NVP-AUY922 treatment, indicating the antiangiogenic effect in the TNBC model. Reduced VEGF secretion by tumor cells after Hsp90 inhibition is considered to be mediated via multiple pathways. VEGF-A monitoring visualized earlier target downregulation by Hsp90 inhibition in an ovarian cancer model and in breast cancer patients. (17, 27) Hsp90 inhibition also downregulated HER2 and EGFR. (28-31) In contrast to EGFR and HER2, which are abundantly expressed in a selected group of cancer patients, VEGF-A has a more general role in cancer. Therefore [89]Zr-bevacizumab can be used as a biomarker in much more cancer types, including TNBC.

Collectively, our data demonstrate that [89]Zr-MAB391 and [89]Zr-bevacizumab provide a novel tool for dual non-invasive monitoring of anti-tumor effects upon Hsp90 inhibitor therapy. It provides an interesting candidate biomarker in cancers in which these drivers are thought to underlie treatment efficacy, like TNBC. Clinical imaging will be the next step to determine the value of this approach in patient selection and treatment follow-up.

Disclosure of potential conflicts of interest
None to disclose.

REFERENCES

1. Foulkes WD, Smith IE, Reis-Filho JS. Triple-negative breast cancer. N Engl J Med 2010;363:1938-48.

2. Carey L, Winer E, Viale G, Cameron D, Gianni L. Triple-negative breast cancer: disease entity or title of convenience? Nat Rev Clin Oncol 2010;7:683-92.

3. Litzenburger BC, Creighton CJ, Tsimelzon A, Chan BT, Hilsenbeck SG, Wang T, et al. High IGF-1R activity in triple-negative breast cancer cell lines and tumorgrafts correlates with sensitivity to anti-IGF-1R therapy. Clin Cancer Res 2011;17:2314-27.

4. Ossovskaya V, Wang Y, Budoff A, Xu Q, Lituev A, Potapova O, et al. Exploring molecular pathways of triple-negative breast cancer. Genes Cancer 2011;2:870-9.

5. Samani AA, Yakar S, LeRoith D, Brodt P. The role of the IGF system in cancer growth and metastasis: overview and recent insights. Endocr Rev 2007;28:20-47.

6. Trepel J, Mollapour M, Giaccone G, Neckers L. Targeting the dynamic HSP90 complex in cancer. Nat Rev Cancer 2010;10:537-49.

7. Neckers L, Workman P. Hsp90 molecular chaperone inhibitors: are we there yet? Clin Cancer Res 2012;18:64-76.

8. Taipale M, Jarosz DF, Lindquist S. HSP90 at the hub of protein homeostasis: emerging mechanistic insights. Nat Rev Mol Cell Biol 2010;11:515-28.

9. Hanahan D, Weinberg RA. Hallmarks of cancer: the next generation. Cell 2011;144:646-74.

10. Mehta PP, Whalen P, Baxi SM, Kung PP, Yamazaki S, Yin MJ. Effective targeting of triple-negative breast cancer cells by PF-4942847, a novel oral inhibitor of Hsp 90. Clin Cancer Res 2011;17:5432-42.

11. Caldas-Lopes E, Cerchietti L, Ahn JH, Clement CC, Robles AI, Rodina A, et al. Hsp90 inhibitor PU-H71, a multimodal inhibitor of malignancy, induces complete responses in triple-negative breast cancer models. Proc Natl Acad Sci USA 2009;106:8368-73.

12. Dijkers EC, Kosterink JG, Rademaker AP, Perk LR, van Dongen GA, Bart J, et al. Development and characterization of clinical-grade [89]Zr-trastuzumab for HER2/neu immunoPET imaging. J Nucl Med 2009;50:974-81.

13. Nagengast WB, de Vries EG, Hospers GA, Mulder NH, de Jong JR, Hollema H, et al. In vivo VEGF imaging with radiolabeled bevacizumab in a human ovarian tumor xenograft. J Nucl Med 2007;48:1313-9.

14. Ruegg CL, Anderson-Berg WT, Brechbiel MW, Mirzadeh S, Gansow OA, Strand M. Improved in vivo stability and tumor targeting of bismuth-labeled antibody. Cancer Res 1990;50:4221-6.

15. Heskamp S, van Laarhoven HW, Molkenboer-Kuenen JD, Franssen GM, Versleijen-Jonkers YM, Oyen WJ, et al. ImmunoSPECT and immunoPET of IGF-1R expression with the radiolabeled antibody R1507 in a triple-negative breast cancer model. J Nucl Med 2010;51:1565-72.

16. Loening AM, Gambhir SS. AMIDE: a free software tool for multimodality medical image analysis. Mol Imaging 2003;2:131-7.

17. Nagengast WB, de Korte MA, Oude Munnink TH, Timmer-Bosscha H, den Dunnen WF, Hollema H, et al. [89]Zr-bevacizumab PET of early antiangiogenic tumor response to treatment with HSP90 inhibitor NVP-AUY922. J Nucl Med 2010;51:761-7.

18. Eccles SA, Massey A, Raynaud FI, Sharp SY, Box G, Valenti M, et al. NVP-AUY922: a novel heat shock protein 90 inhibitor active against xenograft tumor growth, angiogenesis, and metastasis. Cancer Res 2008;68:2850-60.

19. Jensen MR, Schoepfer J, Radimerski T, Massey A, Guy CT, Brueggen J, et al. NVP-AUY922: a small molecule HSP90 inhibitor with potent antitumor activity in preclinical breast cancer models. Breast Cancer Res 2008;10:R33.

6

20. Kelloff GJ, Sigman CC. Cancer biomarkers: selecting the right drug for the right patient. Nat Rev Drug Discov 2012;11:201-14.

21. Dakappagari N, Neely L, Tangri S, Lundgren K, Hipolito L, Estrellado A, et al. An investigation into the potential use of serum Hsp70 as a novel tumour biomarker for Hsp90 inhibitors. Biomarkers 2010;15:31-8.

22. Grem JL, Morrison G, Guo XD, Agnew E, Takimoto CH, Thomas R, et al. Phase I and pharmacologic study of 17-(allylamino)-17-demethoxygeldanamycin in adult patients with solid tumors. J Clin Oncol 2005;23:1885-93.

23. Ramanathan RK, Egorin MJ, Erlichman C, Remick SC, Ramalingam SS, Naret C, et al. Phase I pharmacokinetic and pharmacodynamic study of 17-dimethylaminoethylamino-17-demethoxygeldanamycin, an inhibitor of heat-shock protein 90, in patients with advanced solid tumors. J Clin Oncol 2010;28:1520-6.

24. Kummar S, Gutierrez ME, Gardner ER, Chen X, Figg WD, Zajac-Kaye M, et al. Phase I trial of 17-dimethylaminoethylamino-17-demethoxygeldanamycin (17-DMAG), a heat shock protein inhibitor, administered twice weekly in patients with advanced malignancies. Eur J Cancer 2010;46:340-7.

25. Maor S, Yosepovich A, Papa MZ, Yarden RI, Mayer D, Friedman E, et al. Elevated insulin-like growth factor-I receptor (IGF-IR) levels in primary breast tumors associated with BRCA1 mutations. Cancer Lett 2007;257:236-43.

26. Hudelist G, Wagner T, Rosner M, Fink-Retter A, Gschwantler-Kaulich D, Czerwenka K, et al. Intratumoral IGF-I protein expression is selectively upregulated in breast cancer patients with BRCA1/2 mutations. Endocr Relat Cancer 2007;14:1053-62.

27. Schroder CP, Pedersen JV, Chua S, Swanton C, Akimov M, Ide S, et al. Use of biomarkers and imaging to evaluate the treatment effect of AUY922, an HSP90 inhibitor, in patients with HER2+ or ER+ metastatic breast cancer. J Clin Oncol 29: 2011 (suppl; abstr e11024).

28. Oude Munnink TH, Korte MA, Nagengast WB, Timmer-Bosscha H, Schroder CP, Jong JR, et al. [89]Zr-trastuzumab PET visualises HER2 downregulation by the HSP90 inhibitor NVP-AUY922 in a human tumour xenograft. Eur J Cancer 2010;46:678-84.

29. Smith-Jones PM, Solit DB, Akhurst T, Afroze F, Rosen N, Larson SM. Imaging the pharmacodynamics of HER2 degradation in response to Hsp90 inhibitors. Nat Biotechnol 2004;22:701-6.

30. Niu G, Li Z, Cao Q, Chen X. Monitoring therapeutic response of human ovarian cancer to 17-DMAG by noninvasive PET imaging with ^{64}Cu-DOTA-trastuzumab. Eur J Nucl Med Mol Imaging 2009;36:1510-9.

31. Niu G, Cai W, Chen K, Chen X. Non-invasive PET imaging of EGFR degradation induced by a heat shock protein 90 inhibitor. Mol Imaging Biol 2008;10:99-106.

SUPPLEMENTARY FIGURE
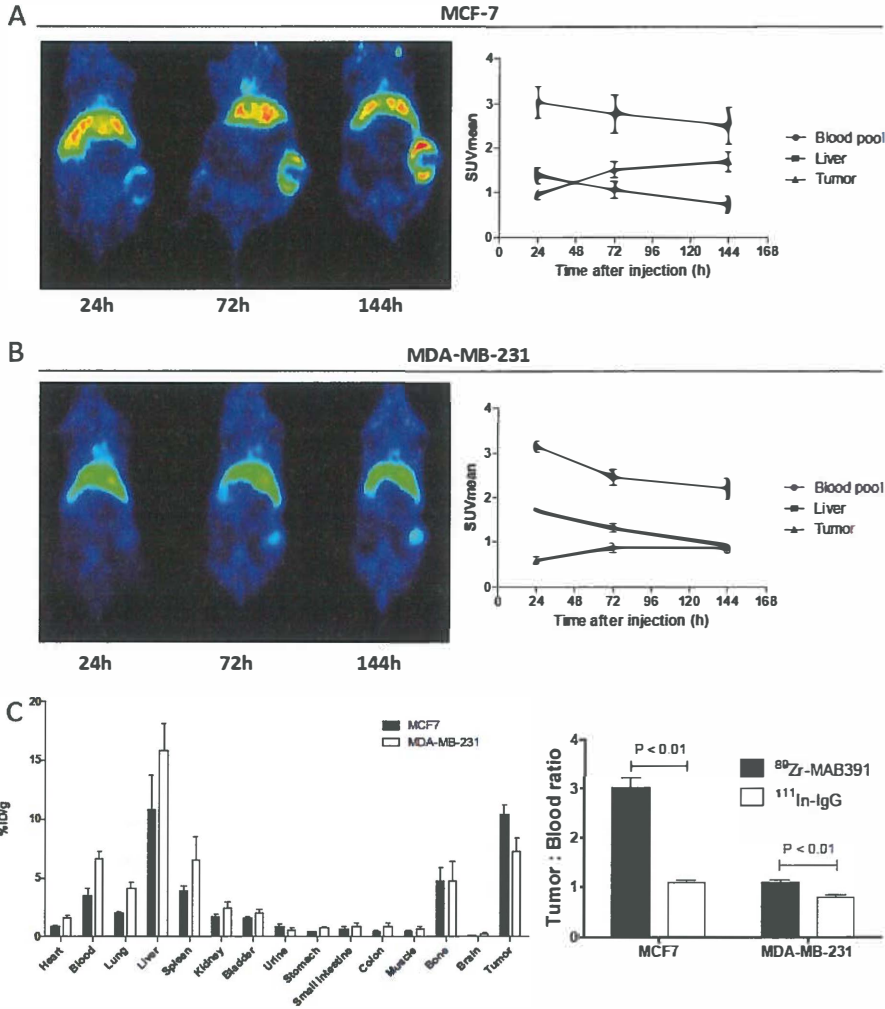
Supplementary Figure S1 | [89]Zr-MAB391 tracer validation. Coronal planes of microPET images at 24, 72 and 144 hours post injection of [89]Zr-MAB391 in MCF-7 (A) and MDA-MB-231 (B) tumors. MicroPET quantification is expressed in SUVmean. *Ex vivo* biodistribution of [89]Zr-MAB391 and comparison of tumor-to-blood ratios between [89]Zr-MAB391 and ^{111}In-IgG, showing specific IGF-1R driven tumor uptake of [89]Zr-MAB391 (C).

CHAPTER 7

Intraoperative near-infrared fluorescence tumor imaging with VEGF and HER2 targeting antibodies

Anton G.T. Terwisscha van Scheltinga[1,2], Gooitzen M. van Dam[3],
Wouter B. Nagengast[1], Vasilis Ntziachristos[4], Harry Hollema[5],
Jennifer L. Herek[6], Carolien P. Schröder[1], Jos G.W. Kosterink[2],
Marjolijn N. Lub-de Hooge[2,7], Elisabeth G.E. de Vries[1]

[1]Department of Medical Oncology, [2]Department of Hospital and Clinical Pharmacy, [3]Department of Surgery, [5]Department of Pathology, [7]Department of Nuclear Medicine and Molecular Imaging, University of Groningen, University Medical Center Groningen, Groningen, The Netherlands. [4]Institute for Biological and Medical Imaging, Technical University of Munich and Helmholtz Center Munich, Germany. [6]Optical Sciences group, MESA+ Institute for Nanotechnology, University of Twente, The Netherlands.

ABSTRACT

Fluorescence imaging is currently attracting much interest as a method for intraoperative tumor detection, but most current tracers lack tumor specificity. Therefore, this technique can be further improved by tumor-specific detection. With tumor targeted antibodies bound to a radioactive label, tumor-specific SPECT or PET imaging is feasible in the clinical setting. The aim of the present study was to apply antibody-based tumor detection to intraoperative optical imaging, using preclinical *in vivo* mouse models.

Methods:
Anti-VEGF antibody bevacizumab and anti-HER2 antibody trastuzumab were labeled with the near infrared (NIR) fluorescence dye IRDye 800CW. Tumor uptake of the fluorescent tracers and their zirconium-89 (^{89}Zr) labeled radioactive counterparts for PET imaging, was determined in human-xenograft-bearing athymic mice during one week after tracer injection, followed by *ex vivo* biodistribution and pathological examination. Intraoperative imaging of fluorescent VEGF- or HER2-positive tumor lesions was performed in subcutaneous tumors and in intraperitoneal (ip) tumor dissemination models.

Results:
Tumor-to-background ratios, with fluorescent imaging, were 1.93 ± 0.40 for bevacizumab and 2.92 ± 0.29 for trastuzumab on day 6 after tracer injection. Real-time intraoperative imaging even detected tumor lesions at the sub-millimeter level in ip-disseminated tumor models. These results were supported by standard histology, immunohistochemistry and fluorescence microscopy analyses.

Conclusion:
NIR fluorescent labeled antibodies, targeting VEGF or HER2, can be used for highly specific and sensitive detection of tumor lesions *in vivo*. These preclinical findings encourage future clinical studies with NIR fluorescent labeled tumor-specific antibodies for intraoperative guided surgery in cancer patients.

INTRODUCTION

Fluorescence imaging is currently attracting much interest as a method for superior intraoperative tumor detection, but most current imaging tracers lack tumor specificity. Therefore combining know-how obtained from targeted therapies such as the use of monoclonal antibodies and expertise on molecular imaging for targeted tumor tracer development might greatly benefit the patient in such a setting.

Molecular imaging, the *in vivo* characterization and measurement of biological processes at the cellular and molecular level. (1) Most experience in translating this approach into the clinic has taken place with positron emission tomography (PET) and single photon emission computed tomography (SPECT) in oncology. (2) Initially, the focus in radionuclide imaging was on the visualization of general tumor processes such as glucose consumption with ^{18}F-fluordeoxyglucose (FDG-PET) and DNA proliferation with ^{18}F-3'-fluoro-3'-deoxy-L-thymidine (FLT-PET). However, the availability of novel targeted tracers and new detection systems for clinical use have expanded the potential of molecular imaging even into the intraoperative setting. A wide variety of tumor characteristics can now be visualized using tracers based on monoclonal antibodies. (3) We developed the PET radiopharmaceuticals zirconium-89 (^{89}Zr) labeled bevacizumab to image vascular endothelial growth factor (VEGF) and ^{89}Zr-trastuzumab to image human epidermal growth factor receptor 2 (HER2) in tumors and tested them successfully preclinical and clinically. (4-7) Bevacizumab, a humanized monoclonal antibody which neutralizes all isoforms of the ligand VEGF-A. (8,9) Trastuzumab, the anti-human HER2 monoclonal antibody, targets the extracellular domain of HER2. (10)

Fluorescence imaging in the intraoperative setting has recently entered the clinical testing phase. This technique uses light instead of ionizing radiation, is real-time, provides high resolution imaging and is relatively inexpensive. (2,11) Compared to PET imaging optical imaging can however not provide non-invasive whole body imaging and there is a limited penetration depth of the signal. There are currently a few intraoperative imaging systems operational in the clinic (12,13), but there is still an unmet need for tumor-specific detection with tumor-specific fluorescent tracers. Our intraoperative tumor-targeted imaging approach of using a small ligand like folate linked to a fluorophore (i.e. fluoresceine isothiocyanate, FITC) which targets specifically the folate-α receptor in ovarian cancer patients will provide the proof-of-principle concept (Netherlands Trial Register #1980; http://www.trialregister.nl). However, because of tissue scattering properties, autofluorescence and absorption of light in the 400-650 nm range, the use of a near infrared (NIR) fluorophore is more attractive for deeper seated tumors with respect to sensitivity and accuracy. Such a tracer should preferably perform in the NIR fluorescence spectrum, which uses light in the 650 – 900 nm spectrum. In this spectrum autofluorescence signals are thus minimized, and there is the lowest tissue absorption of light; this results in optimal tissue penetration. (14) However, few NIR fluorescence tracers are currently available for use in the clinic, and all are non-targeted. Recently, various groups have reported experience with the introduction of image-guided surgery for the detection of the sentinel node in breast cancer and cervical cancer patients with the NIR fluorescence tracer indocyanine green (ICG). (13,15)

7

The use of tumor-specific targeted intraoperative imaging can potentially be expanded to detect tumor margins, locoregional metastases and residual disease after surgery. We therefore decided to test whether we could translate the excellent performance of radiolabeled bevacizumab and trastuzumab into optical imaging with a clinically applicable tumor targeted fluorescent tracer. IRDye 800CW is a NIR fluorophore with optimal characteristics for clinical use, which allows binding to antibodies when used in its N-hydroxysuccinimide (NHS) ester form. A preclinical toxicity study with IRDye 800CW carboxylate showed no toxicity up to 20 mg/kg intravenously (iv) or intradermally. (16)

To develop IRDye 800CW labeled bevacizumab and trastuzumab for specific tumor detection *in vivo*, we verified the results with [89]Zr-bevacizumab and [89]Zr-trastuzumab PET. To this end, *in vivo* mouse models were used with human tumor xenografts for VEGF imaging and HER2 imaging. Intraoperative surgery with the clinically used NIR camera was performed in both subcutaneous (sc) and intraperitoneal (ip) dissemination tumor models.

MATERIALS AND METHODS

Cell lines

The human ovarian cancer cell line A2780 (HER2 negative, with high VEGF production) was kindly provided by Dr. T.C. Hamilton (Fox Chase Cancer Center, Philadelphia, PA). Development of the luciferase transfected subline A2780[luc+] was described by Duiker EW, *et al*. (17) The SK-BR-3 (HER2 overexpressing) breast cancer and KATO-III (HER2 overexpressing) gastric cancer cell lines were obtained from ATCC. The ovarian cancer cell line SKOV-3[luc+] (HER2 overexpressing) was obtained from Caliper Life Sciences. Cell lines were quarantined until screening for microbial contamination and mycoplasm was performed; these tests were negative. Meanwhile, a reproducible supply of cells was established by cryopreservation.

All experiments were performed within a predefined number of passages. Key features of the cell lines were routinely checked. Growth and morphology of the cells was observed and noted to be consistent with prior descriptions of the lines. A2780[luc+] cells were cultured in RPMI 1640 (Invitrogen), supplemented with 10% heat inactivated fetal calf serum (FCS) (Bodinco BV) and 2 mM L-glutamine (Invitrogen). SK-BR-3 and SKOV-3[luc+] were cultured in D-MEM (Invitrogen) supplemented with 10% FCS, KATO-III in RPMI 1640 medium supplemented with 20% FCS. All cell lines were cultured at 37°C in a fully humidified atmosphere containing 5% CO_2.

Bevacizumab and trastuzumab labeling with IRDye 800CW and *in vitro* evaluation of fluorescent labeled compounds

IRDye 800CW-NHS (Li-Cor Biosciences) was coupled to bevacizumab (Roche) and trastuzumab (Roche) according to the manufacturer's protocol. In short, antibodies were reacted with IRDye 800CW at a molar ratio of 1:4 in PBS (pH = 8.5), which was determined as the optimal ratio. The product was purified by ultracentrifugation with Vivaspin sample concentrators (GE Healthcare). Labeling efficiency and purity were determined by size-exclusion high-performance liquid chromatography (SE-HPLC), with UV detector wavelengths at 220, 280 and 790 nm. The labeling efficiency obtained was 85-90% which gives a labeling ratio of an average of 3.5 dyes per antibody, with a purity of >95% after purification. The stability of bevacizumab-800CW and trastuzumab-800CW was verified by storing the final product in 1 mL 0.9% sodium chloride at 4 °C and 37 °C for 7 days. SE-HPLC measurements were performed for one week. No measurable decreases in bound IRDye 800CW were found. The binding properties to VEGF of bevacizumab-800CW were evaluated using a VEGF-coated enzyme-linked immunosorbent assay, as described previously by Nagengast WB, *et al*. (4) Binding of the antibody to the antigen was measured with the Odyssey imaging system (Li-Cor Biosciences). Trastuzumab-800CW binding properties were determined by using a competition assay with unlabeled trastuzumab on SK-BR-3 cells stitched to a 96-well plate with poly-L-lysine (0.01% w/v in water, Sigma-Aldrich). Both bevacizumab-800CW and trastuzumab-800CW showed no decrease in binding affinity.

Bevacizumab and trastuzumab conjugation and zirconium-89 labeling

Conjugation and radiolabeling of bevacizumab and trastuzumab were performed as described earlier. (4,5) Briefly, both antibodies were first conjugated with the chelator tetrafluorphenol N-succinyldesferal (TFP-N-sucDf), which was kindly provided by Dr. GA van Dongen (VU Medical Center, Amsterdam, the Netherlands). After conjugation, the product was purified by ultracentrifugation and stored at −20 °C. In the second step, the conjugated antibodies were radiolabeled with clinical-grade ^{89}Zr oxalate (IBA Molecular). As PET is more quantitative compared to SPECT we used ^{89}Zr labeled antibodies instead of the ^{111}In labeled analogues.

IgG conjugation and indium-111 labeling

Human IgG was used as an aspecific control in the experiments. Human IgG (Sanquin) conjugation and labeling was performed as described by Ruegg *et al*. (18) Briefly, IgG was first conjugated to the bifunctional conjugating agent 2-(4-isothiocyanatobenzyl)-diethylenetriaminepentaacetic acid (p-SCN-Bn-DTPA, Macrocyclics). After conjugation, the product was stored at −20 °C. Conjugated human IgG was radiolabeled with indium-111 (^{111}In) chloride (Covidien).

Glassware, materials and solutions used for the ^{89}Zr and ^{111}In conjugation and labeling procedures were sterilized, pyrogen-free and metal-free. All radiolabeled antibodies had a purity of >95% before administration to the animals.

Animal experiments

For sc tumor models, cells were harvested by trypsinization and resuspended in PBS. *In vivo* imaging and *ex vivo* experiments were conducted using male nude Balb-c mice (Balb/cOlaHSD-foxn^{nu}) obtained from Harlan Nederland. Mice were not kept on a specific diet. At 6-8 weeks of age the mice were injected sc with 5 x 10^6 A2780^{luc+} (n = 10) or 2.5 x 10^6 SK-BR-3 (n = 10) cells in 0.3 mL in Matrigel™ (BD Bioscience). A2780^{luc+} was selected for these experiments given its high VEGF tumor levels when xenografted and the characterization of ^{89}Zr-bevacizumab available in this model. (4) Trastuzumab-800CW was tested in the SK-BR-3 tumor-bearing mice.

Tumor growth was followed with caliper measurements. The tracer was injected when the tumors measured 6-8 mm in diameter (for A2780, 2 weeks after tumor cell inoculation, for SK-BR-3, 4 weeks after inoculation). To compare fluorescence optical imaging with PET, mice received a co-injection of IRDye 800CW- and ^{89}Zr- (5 MBq) labeled bevacizumab or trastuzumab together with the same protein dose of ^{111}In-IgG (1 MBq) as an aspecific control. During a scan sequence, images were made immediately at post-injection of the tracer and at 24, 48, 72 and 144 h afterwards. Two protein doses were tested per tracer: for bevacizumab 30 and 100 µg and for trastuzumab 50 and 100 µg. Half of the tracer protein dose was labeled fluorescently. This correlates with 0.41, 0.68 and 1.36 µg dye for respectively 30, 50 and 100 µg protein, based on a labeling ratio of 3.5 molecules dye per antibody. The difference in lowest protein dose used was different for bevacizumab and trastuzumab as a difference in maximal specific activity could be obtained. Tracer injection was intravenous via the penile vein in a volume of 150 µL.

Animals were imaged using a MicroPET Focus 220 rodent scanner (CTI Siemens). After image reconstruction, *in vivo* quantification was performed with AMIDE Medical Image Data Examiner software (version 0.9.1, Stanford University, Stanford, CA). (19) The data is presented as the mean standard uptake value (SUVmean), which analyzes tumor uptake by comparing it with the total average whole body uptake. Animals were sacrificed after the last scan and organs and tissues were excised and weighed. Samples and primed standards were counted for radioactivity in a calibrated well-type LKB-1282-Compu-gamma system (LKB Wallac) and corrected for physical decay. *Ex vivo* tissue activity is expressed as percentage of the injected dose per gram tissue (%ID/g). Harvested tumors were paraffin embedded for further analysis.

In vivo fluorescence and bioluminescence images were obtained with the IVIS Spectrum (Caliper Life Sciences). Fluorescence images were retrieved by measuring a spectrum with different excitation wavelengths of 675 and 745 nm and using a filter of 800 nm. Data was analyzed using Living Image 3.2 software (Caliper Life Sciences). To determine TBR from NIR fluorescence images, the tumor boundary was set as region of interest (ROI), and the ratio was calculated by comparing the tumor uptake with the background value within the mouse. The TBR was determined after spectral unmixing of the fluorescent signal, performed by Living Image software, to distinguish the IRDye 800CW signal from autofluorescence.

Bioluminescence was achieved by injecting the animals ip weekly with D-luciferin (150 mg/kg; Xenogen) reconstituted in PBS, followed by imaging.

The real-time intraoperative multispectral fluorescence imaging system as developed by Themelis G, *et al.* (12) was used to visualize the location of the fluorescent-labeled antibodies. This system contains three cameras operating in parallel: a color and fluorescence camera and an intrinsic camera for light attenuation images at the excitation wavelength. Images and videos were obtained during surgery and *ex vivo* studies. Figures were made with Adobe Photoshop (version CS4) for creation of the overlay pictures.

Female nude Balb-c mice (Balb/cOlaHSD-foxn^{nu}) with A2780^{luc+} (n = 5), SKOV-3^{luc+} (n = 10) and KATO-III (n = 5) cells were used for ip dissemination tumor models. Mice were kept on an alfalfa-free diet to reduce autofluorescence in the peritoneum. A total of 2×10^6, 5×10^6 or 2×10^6 cells were injected ip (volume 0.5 mL). Tumor growth was tracked with weekly bioluminescence measurements in mice who received cells of a luciferase-positive cell line, using the IVIS Spectrum. The fluorescent tracer was injected ip 3 weeks after inoculation of A2780^{luc+} and KATO-III and 4 weeks after SKOV-3^{luc+}. Ten mice inoculated with the A2780^{luc+} (n = 5) or SKOV-3^{luc+} (n = 5) received 100 µg bevacizumab-800CW. Trastuzumab-800CW (100 µg) was administered in 5 mice inoculated with SKOV-3^{luc+} and 5 mice with KATO-III tumor. On day 4 after tracer injection, all mice received isoflurane inhalation anesthesia (induction 3%, maintenance 1.5%) to undergo NIR fluorescent imaging during surgery.

To validate the findings with the intraoperative fluorescence imaging system, one animal from each group was also scanned in the IVIS Spectrum system. If present, at least three fluorescent spots were excised intraoperatively for pathological and fluorescence microscopy analysis. Harvested fluorescent lesions were paraffin embedded for further analysis. During surgery, intraoperative imaging was performed by recording still images and movies. After this procedure the mice were sacrificed. The animal experiments were approved by the animal experiments committee of the University of Groningen.

Ex vivo tissue analysis

Paraffin-embedded sc tumors and fluorescent ip lesions were stained with hematoxylin and eosin (H&E) and immunohistochemically for VEGF (sc-152, Santa Cruz) or HER2 (CB11, Neomarkers).

Hoechst staining (33258, Invitrogen) was used to visualize nuclei for fluorescence microscopy. Fluorescence microscopy analysis was performed using an Olympus Fluoview 300 confocal scan box mounted on an Olympus IX 71 inverted microscope. The laser source (Coherent, Paladin) produces photons of 532 nm and 1064 nm. The optical parametric oscillator (APE Berlin) converts photons to longer wavelengths. (20) In this setting the 532 nm photons are converted to 770 nm, which served to visualize the IRDye 800CW bound to the antibody. Light at 1064 nm was used to visualize the Hoechst nuclear staining by two-photon fluorescence. The filter set consisted of the combination of two band-pass filters (Chroma #850-90m-2p) and long-pass emission filters (Chroma #HQ795LP). Image analysis was performed using FV10-ASW (version 1.6).

Statistical analysis

Data are presented as mean ± SD. Statistical analysis was performed using the Mann-Whitney test for non-parametric data (GraphPad Prism, version 5). A P value of 0.05 or less was considered significant.

RESULTS

Dual modality VEGF imaging

First we compared the characteristics of fluorescent labeled bevacizumab with [89]Zr-bevacizumab (Fig. 1A, B). In the luciferase-positive tumors, an increasing bioluminescence signal was observed during tumor growth, assuring the vitality of most tumor cells. Quantification of tumor uptake by TBR of the optical fluorescence images revealed an increased signal with a higher fluorescent tracer protein dose of bevacizumab-800CW (Fig. 1A). The TBR was 1.35 ± 0.11 in the 30 µg bevacizumab group and 1.93 ± 0.40 in the 100 µg bevacizumab group (P = 0.014) 6 days after tracer injection. The tumor SUVmean of [89]Zr-bevacizumab was slightly lower in the 100 µg bevacizumab group than in the 30 µg group (Fig. 1B). Optical and nuclear imaging showed an increasing tumor signal over time. Specificity of [89]Zr-bevacizumab tumor uptake was shown as [89]Zr-bevacizumab tumor uptake *ex vivo* compared to ^{111}In-IgG as nonspecific tumor uptake. There was a 64.7% higher uptake in the 30 µg bevacizumab group (P < 0.0001) and 53.2% (P < 0.0049) higher uptake in the 100 µg bevacizumab group compared to the IgG tumor uptake.
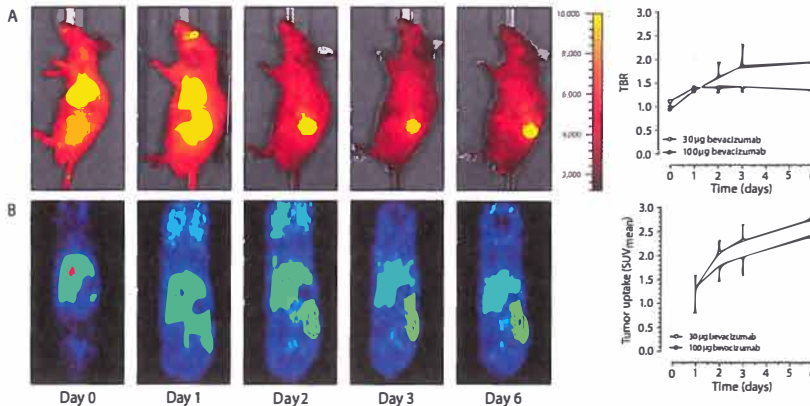

Figure 1 | Dual modality imaging of VEGF in a sc A2780[luc+] xenograft model. A, Representative sagittal (two-dimensional) fluorescence images of bevacizumab-800CW immediately after tracer injection of 100 µg bevacizumab and at indicated days and relative tumor uptake displayed in TBR. B, Correlated coronal microPET images after [89]Zr-bevacizumab injection and tumor uptake (SUVmean) as determined by microPET data quantification for both dose groups (30 and 100 µg bevacizumab). TBR = tumor-to-background ratio, SUVmean = mean standard uptake value.

Dual modality HER2 imaging

Based on the fluorescent images, the TBR showed a dose-related effect with 1.67 ± 0.18 at 50 µg and 2.92 ± 0.29 at 100 µg trastuzumab (P < 0.0001) (Fig. 2A). The tumor uptake in the low-dose trastuzumab group was already maximal at Day 1 post-injection. The optimal time point for measuring fluorescence was comparable to VEGF imaging: between 3 and 6 days after fluorescent tracer injection, based on increasing TBR. The maximum ^{89}Zr-trastuzumab tumor uptake, measured with microPET, was similar for the 50 and 100 µg trastuzumab groups (Fig. 2B). The specificity of this ^{89}Zr-trastuzumab tumor uptake, shown as tumor uptake of ^{111}In-IgG (co-injected), was less in both groups: 74.0% in the 100 µg protein dose group (P = 0.0016) and 91.2% in the 50 µg protein dose group (P < 0.0001).
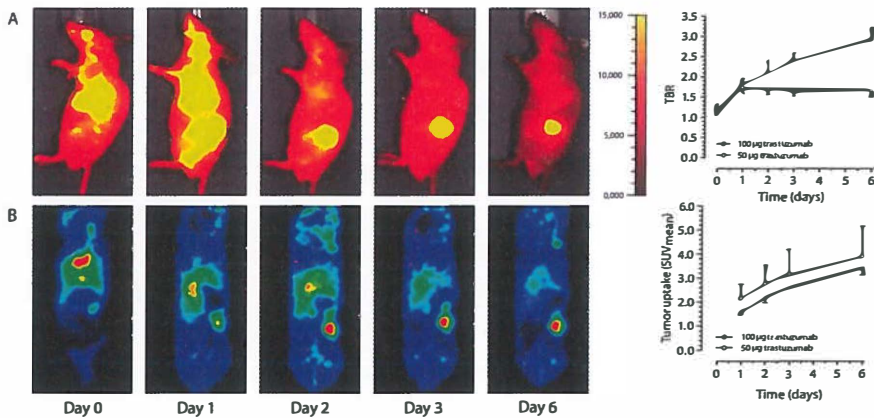

Figure 2 | Dual modality imaging of HER2 in a sc SK-BR-3 xenograft model. A, Representative sagittal (two-dimensional) fluorescence images of trastuzumab-800CW immediately after tracer injection of 100 µg trastuzumab and at indicated days and relative tumor uptake displayed in TBR. B, Correlated coronal microPET images after ^{89}Zr- trastuzumab injection and tumor uptake (SUVmean) as determined by microPET data quantification (50 and 100 µg trastuzumab). TBR = tumor-to-background ratio, SUVmean = mean standard uptake value.

NIR fluorescent labeled antibodies allow *in vivo* intraoperative guided surgery in a sc and ip dissemination tumor model

Tumor uptake of the fluorescent-labeled antibodies was clearly visible with the intraoperative fluorescent system in mice receiving bevacizumab-800CW (Fig. 3) or trastuzumab-800CW (Supplemental Fig. S1A). The fluorescence signal of the sc tumor was detectable despite the intact skin overlying the tumor.

The supplemental video shows the fluorescence signal of trastuzumab-800CW captured by the intraoperative fluorescence imaging system while the surgeon removes the sc SK-BR-3 tumor (Supplemental Digital Content; Video 1, supplemental videos are available online only at http://jnm.snmjournals.org).

Tumor models with high peritoneal metastatic spread were used to investigate whether the fluorescent-labeled antibodies were able to visualize small tumor spots in the peritoneal cavity.
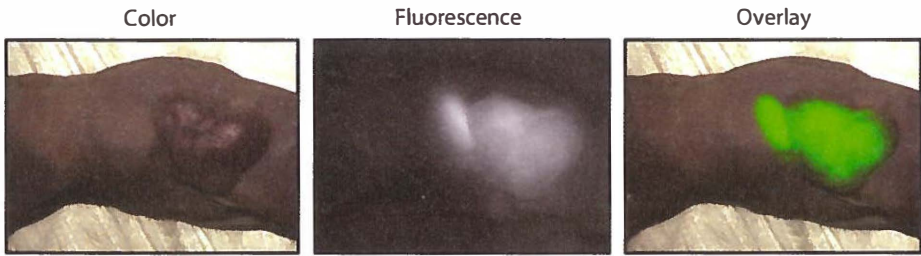
Figure 3 | Intraoperative images of bevacizumab-800CW. Representative intraoperative images of a sc A2780 tumor bearing mouse. The ovarian cancer was targeted with bevacizumab-800CW. Three images are shown: the color image, the fluorescent image and an overlay of the fluorescence signal in green on top of the color image. The weaker background fluorescence of the stomach comes from the fluorescence of chlorophyll in the food of the animals used in these groups. These mice were not kept on alfalfa-free diet.

In mice bearing the luciferase-positive cell lines, increasing bioluminescence was observed over time after inoculation, indicating tumor growth and vitality of tumor cells.

For bevacizumab-800CW and trastuzumab-800CW, even sub-millimeter lesions could be distinguished intraoperatively by the emitted fluorescent signal. Peroperative images for bevacizumab-800CW are shown in the Supplemental Fig. S2A, B. Both ovarian cancer models showed ip tumor growth measured with bioluminescence imaging. For the HER2 overexpressing SKOV-3^{luc+}, small tumor lesions could be visualized with bevacizumab-800CW (Supplemental Fig. S2B) as well as with trastuzumab-800CW (Supplemental Fig. S1B) with the intraoperative camera. Trastuzumab-800CW was also able to visualize the HER2 positive KATO-III tumor lesions (Fig. 4). Lesions were found ranging from sub-millimeter size to several centimeters. In addition, lesions smaller than 1 mm were removed from the peritoneum based on the fluorescence signal.
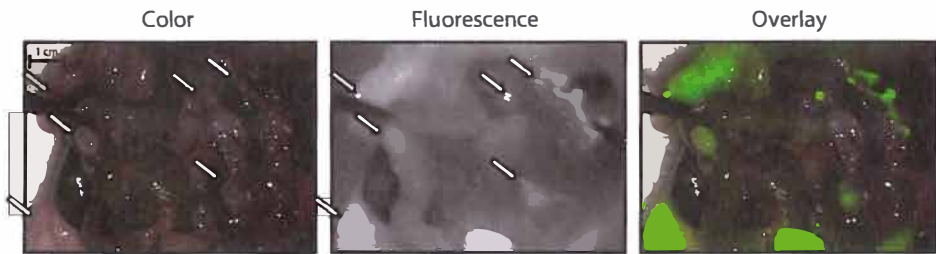

Figure 4 | Intraoperative images of trastuzumab-800CW. Images of human gastric cancer KATO-III ip tumor model. Three images are shown: the color image, the fluorescent image and an overlay of the fluorescence signal in green on top of the color image.

The intense fluorescence signal correlates with tumor lesions as measured with bioluminescence. This indicates specific tumor uptake and detection of lesions by fluorescence signal during imaging. The fluorescent signal is present where vital tumor cells are shown using bioluminescent imaging of A2780^{luc+} tumors, fluorescence signal is obtained with bevacizumab-800CW (Supplemental Fig. S3A) and SKOV-3^{luc+} tumors with trastuzumab-800CW (Supplemental Fig. S3B).

The supplemental video (Supplemental Digital Content; Video 2) visualizes the experimental setting of intraoperative imaging during surgery on a mouse. The fluorescence signal of bevacizumab-800CW was captured during removal of ip SKOV-3^{luc+} tumor spots as a representative example.

Ex vivo tissue analysis supports tumor-specific detection with NIR fluorescent labeled antibodies

H&E staining, VEGF staining and fluorescence microscopy showed that the lesions with fluorescent signals contained tumor cells; this is illustrated for the A2780^{luc+} sc tumor (Fig. 5). The same results were found in small ip lesions of the ip-injected A2780^{luc+} and SKOV-3^{luc+}. Comparably, in the SK-BR-3 sc tumor, viable tumor cells were detected with H&E, HER2 and fluorescence microscopy (Fig. 5). SKOV-3^{luc+}, and KATO-III ip fluorescent lesions also showed viable tumor cells. As expected, fluorescence microscopy showed bevacizumab-800CW in the extracellular matrix of the tumor, while trastuzumab-800CW fluorescence was detected mainly on the tumor cell surface.
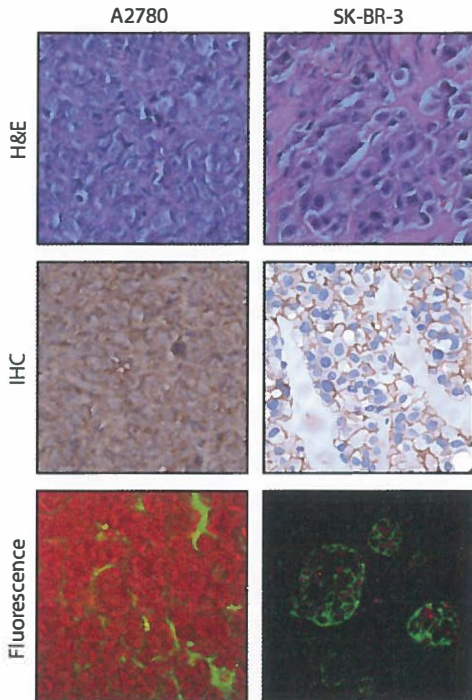

Figure 5 | A2780 sc tumor microscopy images (400x); H&E staining, VEGF staining and fluorescence signal of bevacizumab-800CW (green) and nuclei visualized by fluorescence after Hoechst staining (red). SK-BR-3 sc tumor microscopy images (400x); H&E staining, HER2 staining and fluorescence signal of trastuzumab-800CW (green) and nuclei (red).

DISCUSSION

These results are the first to show that tumor targeted NIR fluorescence labeled therapeutic antibodies can be used for specific tumor detection *in vivo* in a preclinical setting, using the real-time intraoperative clinical prototype camera system.

In the present study, the excellent selective tumor uptake previously shown with PET of [89]Zr-bevacizumab and [89]Zr-trastuzumab in mice bearing human xenografts (4,5) was also observed for the same antibodies labeled with a fluorescent dye.

The TBR obtained for trastuzumab-800CW was somewhat higher compared to bevacizumab-800CW. This can at least partially be explained by the fact that bevacizumab targets only human VEGF, which is produced by the implanted human tumor cells. In the human xenograft tumor models, murine VEGF also plays a role, but bevacizumab does not bind or neutralize murine VEGF. (21,22) This assumption is supported by the finding that the radioactive bevacizumab tracer showed a lower tumor uptake in the preclinical setting than in patients. (6,7)

[89]Zr-bevacizumab and [89]Zr-trastuzumab showed high specific tumor uptake, with increasing tumor-to-background ratios during the first 4 days following tracer injection. (6,7) The long half-life of the antibodies implies that these antibodies require days to accumulate optimally in the tumor. Our clinical studies with [89]Zr-bevacizumab and [89]Zr-trastuzumab indicated that day 4 after tracer injection is optimal for nuclear imaging. In the present study, the optimal time for optical imaging for both antibodies was around day 3 after fluorescent tracer injection. Our results with the IRDye 800CW-labeled antibodies directing against VEGF and HER2 revealed the possibility of detecting sub-millimeter lesions with a clinical intraoperative camera.

This information adds to the recent data obtained for fluorescent labeled antibodies targeting the epidermal growth factor receptor (EGFR), HER2 and the insulin-like growth factor receptor 1 (IGF-1R). (23-26) Cetuximab labeled with the NIR fluorescent dye Cy5.5 showed specific tumor uptake in head and neck squamous cell carcinoma xenografts (23), while the IGF-1R targeting antibody AVE-1642 labeled with the NIR fluorescent dye Alexa 680 was specifically taken up by the R-/IGF-1R xenograft tumor. (24) Trastuzumab that was dual labeled with ^{111}In-DTPA and IRDye 800CW showed a similar tumor-to-muscle ratio of 2.25 for fluorescence measurements and 2.66 in a SK-BR-3[luc+] model for SPECT. (25) Although these results are very promising, no clinical trials have yet been performed with these targeted fluorescent labels. This specific uptake – not only of HER2 and VEGF, but also of EGFR and IGF-1R directed antibodies labeled with a fluorescent tracer – further supports the potential to expand our findings to several other targets that could be visualized in tumor tissues of patients with optical imaging when labeled with clinical grade IRDye 800CW. No NIR targeted tracers are currently available for clinical use; the tracers discussed above could fill this gap in future clinical studies.

Currently, the only NIR fluorescence tracer approved by the FDA for human use is ICG, but it is not a targeted tracer. To address this problem, the antibodies daclizumab (targets CD25), panitumumab (targets HER1) and trastuzumab (targets HER2), were labeled with activatable NIR fluorescent tracers of ICG. They were tested in the preclinical setting and indeed visualized the tumors. (26) However, because ICG loses its fluorescence once it is covalently bound to protein, the fluorescence only becomes visible after activation due to cellular internalization of the tracer and degradation of the antibody. (26,27) Consequently, this approach cannot visualize VEGF, which is mainly present in the extracellular matrix. It could also underestimate the signal, for example in case of growth factor receptors such as HER2. In that case, apart from internalization of the receptor, there will also be a receptor at the cell membrane, as demonstrated in fluorescent microscopy results, which will not lead to a fluorescent signal. Our fluorescent microscopic analysis of IRDye 800CW clearly showed that the signal originates precisely where it was expected for both tracers: for bevacizumab-800CW between tumor cells in the microenvironment and for trastuzumab-800CW intracellular and on the tumor cell surface.

The dose of labeled antibodies required for molecular imaging in patients is in the sub-therapeutic microdose ranges. When antibodies have a linear kinetic profile, no supplementation of unlabeled antibody is necessary for PET imaging. This is the case for U36, a CD44v6-specific murine mAb, and for bevacizumab. (28-30) Therefore, imaging studies in patients with these [89]Zr labeled antibodies were performed with 10 mg for U36 and 5 mg for bevacizumab. (7,31) For optical clinical imaging purposes, comparable protein doses will be used. This is different for trastuzumab, which has dose-dependent pharmacokinetics. After multiple therapeutic doses, trastuzumab clearance has an average terminal half-life of 28.5 days at steady state. (32) However, when given as a single dose of 10 mg, trastuzumab has terminal half-life of only 1.5 days. (33) This is too short to allow adequate accumulation of the tracer in the tumors and subsequent imaging. In the [89]Zr-trastuzumab study, supplementation with 50 mg unlabeled trastuzumab was optimal. (6) This aspect will have to be taken into account for the imaging with trastuzumab-800CW as well.

Given the interesting characteristics of IRDye 800CW for use in the clinic, we are currently performing the preclinical toxicity testing of bevacizumab-800CW to permit clinical trials with this tracer. However, the best optical imaging may require a cocktail of tracers targeting different tumor characteristics. For example, this is important for breast cancer because it is increasingly becoming clear that this is a heterogeneous disease, which can exhibit a variety of characteristics. Based on these experiments, both tracers can be interesting for the clinic, depending on the presence of the target in the tumor. Compared to HER2, VEGF is the more general target for cancer detection, as it is more frequently overexpressed in many tumor types. (8)

Apart from intraoperative image-guided surgery, fluorescence imaging systems are also being developed for diffuse optical imaging (DOI), hand-held photo-acoustic based imaging, fluorescent endoscopy and confocal laser endomicroscopy (CLE). (34-36) When used for studying breast tissue, DOI is often referred to as optical mammography. This technique is currently being tested in early clinical trials. (37) CLE allows *in vivo*

7

imaging of the mucosal layer during gastrointestinal endoscopy. Interestingly, the feasibility of VEGF imaging in a preclinical gastrointestinal cancer model and human tissue using CLE was recently demonstrated by using a polyclonal rabbit antibody raised against the -121, -165 and -189 isoforms of human and murine VEGF labeled with Alexa-Fluor 488. (34) The VEGF-specific signal was visualized and correlated well with *ex vivo* microscopy. The first clinical trials using CLE with tumor targeted fluorescent tracers are expected to start soon.

CONCLUSION

In a preclinical setting, NIR fluorescent labeled antibodies targeting VEGF or HER2 allowed highly specific and sensitive detection of tumor lesions *in vivo*. These findings strongly support future clinical studies with NIR fluorescent labeled tumor-specific antibodies. This applies to a wide range of clinical applications, including intraoperative image-guided surgery.

### Disclosure of potential conflicts of interest
None to disclose.

REFERENCES

1. Weissleder R, Mahmood U. Molecular imaging. Radiology. 2001;219:316-333.

2. Pysz MA, Gambhir SS, Willmann JK. Molecular imaging: current status and emerging strategies. Clin Radiol. 2010;65:500-516.

3. van Dongen GA, Vosjan MJ. Immuno-positron emission tomography: shedding light on clinical antibody therapy. Cancer Biother Radiopharm. 2010;25:375-385.

4. Nagengast WB, de Vries EG, Hospers GA, Mulder NH, de Jong JR, Hollema H, et al. In vivo VEGF imaging with radiolabeled bevacizumab in a human ovarian tumor xenograft. J Nucl Med. 2007;48:1313-1319.

5. Dijkers EC, Kosterink JG, Rademaker AP, Perk LR, van Dongen GA, Bart J, et al. Development and characterization of clinical-grade [89]Zr-trastuzumab for HER2/neu immunoPET imaging. J Nucl Med. 2009;50:974-981.

6. Dijkers EC, Oude Munnink TH, Kosterink JG, Brouwers AH, Jager PL, de Jong JR, et al. Biodistribution of [89]Zr-trastuzumab and PET imaging of HER2-positive lesions in patients with metastatic breast cancer. Clin Pharmacol Ther. 2010;87:586-592.

7. Oosting SF, Nagengast WB, Oude Munnink TH, Lub-de Hooge MN, Brouwers AH, Glaudemans AW, et al. [89]Zr-bevacizumab PET imaging in renal cell carcinoma patients: feasibility of tumor VEGF quantification. Eur J Cancer. Suppl. 2010;7:72-73.

8. Ferrara N, Davis-Smyth T. The biology of vascular endothelial growth factor. Endocr Rev. 1997;18:4-25.

9. Gerber HP, Ferrara N. Pharmacology and pharmacodynamics of bevacizumab as monotherapy or in combination with cytotoxic therapy in preclinical studies. Cancer Res. 2005;65:671-680.

10. Moasser MM. The oncogene HER2: its signaling and transforming functions and its role in human cancer pathogenesis. Oncogene. 2007;26:6469-6487.

11. Frangioni JV. New technologies for human cancer imaging. J Clin Oncol. 2008;26:4012-4021.

12. Themelis G, Yoo JS, Soh KS, Schulz R, Ntziachristos V. Real-time intraoperative fluorescence imaging system using light-absorption correction. J Biomed Opt. 2009;14:064012.

13. Troyan SL, Kianzad V, Gibbs-Strauss SL, Gioux S, Matsui A, Oketokoun R, et al. The FLARE intraoperative near-infrared fluorescence imaging system: a first-in-human clinical trial in breast cancer sentinel lymph node mapping. Ann Surg Oncol. 2009;16:2943-2952.

14. Hilderbrand SA, Weissleder R. Near-infrared fluorescence: application to in vivo molecular imaging. Curr Opin Chem Biol. 2010;14:71-79.

15. Crane LM, Themelis G, Pleijhuis RG, Harlaar NJ, Sarantopoulos A, Arts HJ, et al. Intraoperative multispectral fluorescence imaging for the detection of the sentinel lymph node in cervical cancer: a novel concept. Mol Imaging Biol. 2011; In press.

16. Marshall MV, Draney D, Sevick-Muraca EM, Olive DM. Single-dose intravenous toxicity study of IRDye 800CW in Sprague-Dawley rats. Mol Imaging Biol. 2010;12:583-594.

17. Duiker EW, de Vries EG, Mahalingam D, Meersma GJ, Boersma-van Ek W, Hollema H, et al. Enhanced antitumor efficacy of a DR5-specific TRAIL variant over recombinant human TRAIL in a bioluminescent ovarian cancer xenograft model. Clin Cancer Res. 2009;15:2048-2057.

18. Ruegg CL, Anderson-Berg WT, Brechbiel MW, Mirzadeh S, Gansow OA, Strand M. Improved in vivo stability and tumor targeting of bismuth-labeled antibody. Cancer Res. 1990;50:4221-4226.

19. Loening AM, Gambhir SS. AMIDE: a free software tool for multimodality medical image analysis. Mol Imaging. 2003;2:131-137.

7

20. Jurna M, Korterik JP, Offerhaus HL, Otto C. Noncitical phase-matched lithium triborate optical parametric oscillator for high resolution coherent anti-Stokes Raman scattering spectroscopy and microscopy. Appl Phys Lett. 2006;89:251116.

21. Yu L, Wu X, Cheng Z, Lee CV, LeCouter J, Campa C et al. Interaction between bevacizumab and murine VEGF-A: a reassessment. Invest Ophthalmol Vis Sci. 2008;49:522-527.

22. Lee S, Chen TT, Barber CL, Jordan MC, Murdock J, Desai S, et al. Autocrine VEGF signaling is required for vascular homeostasis. Cell. 2007;130:691-703.

23. Rosenthal EL, Kulbersh BD, King T, Chaudhuri TR, Zinn KR. Use of fluorescent labeled anti-epidermal growth factor receptor antibody to image head and neck squamous cell carcinoma xenografts. Mol Cancer Ther. 2007;6:1230-1238.

24. Zhang H, Zeng X, Li Q, Gaillard-Kelly M, Wagner CR, Yee D. Fluorescent tumour imaging of type I IGF receptor in vivo: comparison of antibody-conjugated quantum dots and small-molecule fluorophore. Br J Cancer. 2009;101:71-79.

25. Sampath L, Kwon S, Ke S, Wang W, Schiff R, Mawad ME, et al. Dual-labeled trastuzumab-based imaging agent for the detection of human epidermal growth factor receptor 2 overexpression in breast cancer. J Nucl Med. 2007;48:1501-1510.

26. Ogawa M, Kosaka N, Choyke PL, Kobayashi H. In vivo molecular imaging of cancer with a quenching near-infrared fluorescent probe using conjugates of monoclonal antibodies and indocyanine green. Cancer Res. 2009;69:1268-1272.

27. Kobayashi H, Choyke PL. Target-cancer-cell-specific activatable fluorescence imaging probes: Rational design and in vivo applications. Acc Chem Res. 2011;44:83-90.

28. de Bree R, Roos JC, Quak JJ, den Hollander W, Snow GB, van Dongen GA. Radioimmunoscintigraphy and biodistribution of technetium-99m-labeled monoclonal antibody U36 in patients with head and neck cancer. Clin Cancer Res. 1995;1:591-598.

29. Colnot DR, Quak JJ, Roos JC, van Lingen A, Wilhelm AJ, van Kamp GJ, et al. Phase I therapy study of 186Re-labeled chimeric monoclonal antibody U36 in patients with squamous cell carcinoma of the head and neck. J Nucl Med. 2000;41:1999-2010.

30. Gordon MS, Margolin K, Talpaz M, Sledge GW Jr, Holmgren E, Benjamin R, et al. Phase I safety and pharmacokinetic study of recombinant human anti-vascular endothelial growth factor in patients with advanced cancer. J Clin Oncol 2001;19:843-850.

31. Borjesson PK, Jauw YW, Boellaard R, de Bree R, Comans EF, Roos JC, et al. Performance of immuno-positron emission tomography with zirconium-89-labeled chimeric monoclonal antibody U36 in the detection of lymph node metastases in head and neck cancer patients. Clin Cancer Res. 2006;12:2133-2140.

32. Bruno R, Washington CB, Lu JF, Lieberman G, Banken L, Klein P.. Population pharmacokinetics of trastuzumab in patients with HER2+ metastatic breast cancer. Cancer Chemother Pharmacol. 2005;56:361-369.

33. US Food and Drug Administration. FDA Clinical Review of BLA 98-0369: Herceptin Trastuzumab (rhuMAb HER2). <http://www.fda.gov/downloads/Drugs/DevelopmentApprovalProcess/HowDrugsareDevelopedandApproved/ApprovalApplications/TherapeuticBiologicApplications/ucm091373.pdf>.

34. Foersch S, Kiesslich R, Waldner MJ, Delaney P, Galle PR, Neurath MF, et al. Molecular imaging of VEGF in gastrointestinal cancer in vivo using confocal laser endomicroscopy. Gut. 2010;59:1046-1055.

35. Ntziachristos V, Razansky D. Molecular imaging by means of multispectral optoacoustic tomography (MSOT). Chem Rev. 2010;110:2783-2794.

36. van de Ven SM, Elias SG, van den Bosch MA, Luijten P, Mali WP. Optical imaging of the breast. Cancer Imaging. 2008;8:206-215.

37. van de Ven S, Wiethoff A, Nielsen T, Brendel B, van der Voort M, Nachabe R, et al. A novel fluorescent imaging agent for diffuse optical tomography of the breast: first clinical experience in patients. Mol Imaging Biol. 2010;12:343-348.

7

SUPPLEMENTARY FIGURES
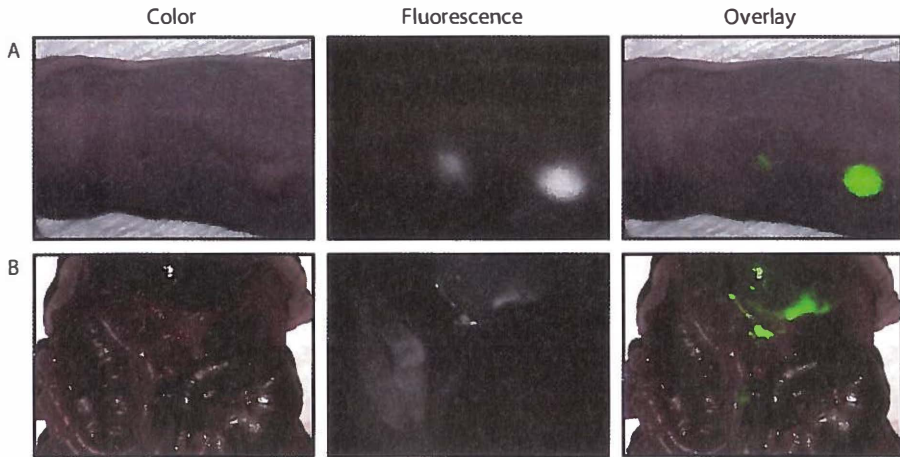
Supplementary Figure S1 | Intraoperative images of trastuzumab-800CW. A, Representative intraoperative images of mice with sc SK-BR-3 tumor. The breast cancer was targeted with trastuzumab-800CW. B, Images of human ovarian tumor SKOV-3[luc+] ip dissemination model. Three images are shown in each lane: the color image, the fluorescent image and an overlay of the fluorescence signal in green on top of the color image. The weaker background fluorescence of the stomach comes from the fluorescence of chlorophyll in the food of the animals used in these groups. These mice were not kept on alfalfa-free diet.
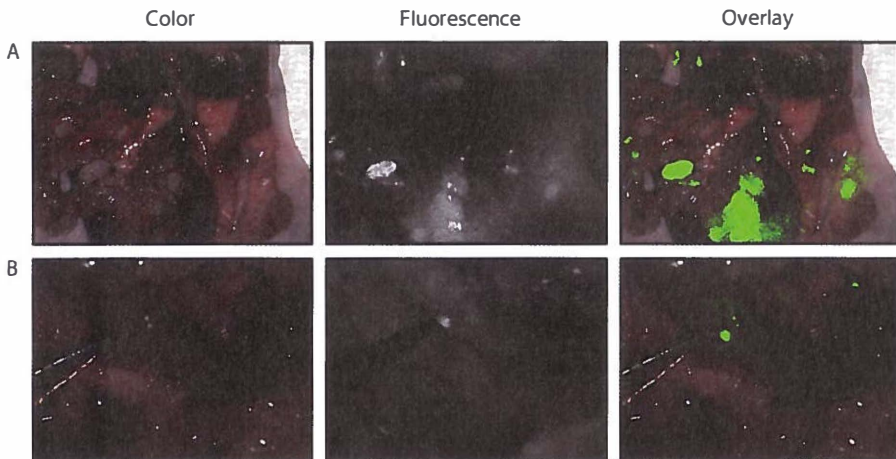
Supplementary Figure S2 | Intraoperative images of bevacizumab-800CW. A, Images of A2780 ip dissemination model. B, Images of ovarian tumor SKOV-3[luc+] ip tumor model. Three images are shown in each lane: the color image, the fluorescent image and an overlay of the fluorescence signal in green on top of the color image.
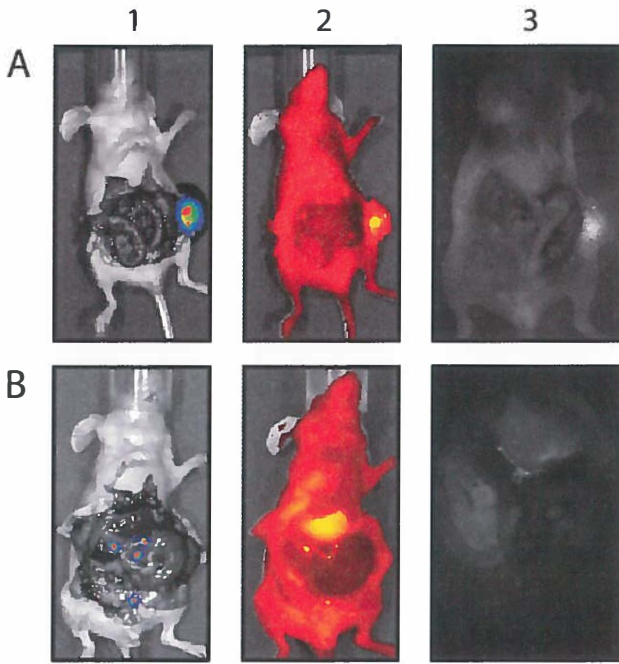
Supplementary Figure S3 ❘ Correlation between bioluminescence and fluorescence signal. 1. Bioluminescence signal measured with IVIS Spectrum. 2. Fluorescence signal measured with IVIS Spectrum. 3. Fluorescence signal measured with intra-operative camera system. Fluorescent signal is present where vital tumor cells are shown with bioluminescent imaging for both bevacizumab-800CW (A) and trastuzumab-800CW (B).

CHAPTER 8

Summary, general discussion and future perspectives

SUMMARY

Therapeutic approaches in oncology consist besides local treatment by surgery and radiotherapy, of drugs administered systemically. Together these approaches form the basis of anti-cancer treatment. Anticancer drugs consist of chemotherapeutic drugs and targeted agents. Chemotherapeutic drugs directly or indirectly aim to induce DNA damage resulting in cell cycle arrest and apoptosis. Per tumor type, different specific combinations of cytostatic agents are being combined. Unfortunately resistance against the chemotherapeutic agents often occurs, which leads to treatment failure.

In the past decades tumor biology research identified new molecular tumor characteristics, also defined as the hallmarks of cancer. (1) These hallmarks include among others sustaining proliferative signaling, evading growth suppressors, inducing angiogenesis and activating invasion and metastasis. Understanding of these hallmarks increasingly affect the development of new drugs. (2-3) Numerous new targeted anticancer agents, specific for cellular targets at the cell membrane, within the tumor cell, soluble targets in the extracellular matrix or at the blood vessels of the tumor, have been developed. Relevant drug targets where this thesis focused on are the receptor tyrosine kinases from the human epidermal growth factor receptor (HER) family, insulin-like growth factor receptor 1 (IGF-1R) and the mesenchymal-epithelial transition factor (c-Met) receptor. Also the pro-angiogenic vascular endothelial growth factor (VEGF) , the molecular chaperone heat shock protein-90 (Hsp90) and the downstream factor mammalian target of rapamycin (mTOR) have been used as target for drug targeting.

The novel molecular targets for anticancer treatment resulted in the development of targeted anticancer drugs, including therapeutic monoclonal antibodies. Molecular imaging using radiolabeled antibodies can identify noninvasively the presence of specific targets against which the drug is raised. Moreover it provides whole body information about tumor uptake and organ distribution of the antibodies. Besides visualization of drug distribution, these radiolabeled antibodies can be used to monitor tumor status during treatment effects, thereby using the receptor or ligands as biomarker. Depending on the type of radioisotope labeled to the antibody, imaging can be performed with planar scintigraphy and single photon emission computed tomography (SPECT) or positron emission tomography (PET). This approach can potentially serve in the clinic for patient selection, tumor staging and as (early) predictive biomarker for tumor response. Additionally, molecular imaging is explored for its use in translating cancer science, in the discovery, development, evaluation and implementation of targeted anticancer agents. (4)

ImmunoPET is defined as the tracking and quantification of radiolabeled monoclonal antibodies with PET *in vivo*. A suitable radioisotope for PET-imaging with antibodies currently available is zirconium-89 (^{89}Zr). ^{89}Zr has been labeled to various antibodies and tested successfully preclinical and clinically. Besides nuclear imaging, also fluorescent labeled antibodies can be visualized using optical imaging approaches. Potential local measurement of drug targets will become available in the near future which can be visualized using

fluorescent labeled antibodies by using newly developed optical imaging platforms such as intraoperative camera, multispectral optoacoustic tomography and fluorescent endoscopy.

This thesis aimed at the development and application of new tracers for molecular imaging with ^{89}Zr-labeled radiopharmaceuticals for PET imaging and fluorescent labeled antibodies for optical imaging.

Chapter 1 provides an introduction and description of the contents. In chapter 2 an overview is presented on imaging modalities which can be used to visualize multidrug resistance (MDR) and it addresses the possibility to image targets for the follow up of targeted therapies. MDR is the resistance of tumor cells to several structurally unrelated classes of chemotherapeutic drugs from natural origin, including anthracyclines, taxanes and vinca-alkaloids. Several mechanisms can attribute to MDR, including the expression of adenosine triphosphate binding cassette transporters (ABC transporters). These transporters, including P-glycoprotein (P-gp) and multidrug resistance protein (MRP), function as drug efflux pumps. To improve the understanding of their *in vivo* function, nuclear medicine imaging techniques have been developed to visualize the activity of these pumps with SPECT and PET. The methods and possibilities to visualize these pumps in the tumor, the blood brain barrier and other locations were discussed in this chapter. The clinical relevance of these pumps in oncology appeared to be limited so far, as the addition of blockers of these pumps to chemotherapy did not improve cancer patient outcome. It is becoming clear that MDR can be circumvented by the newer non-chemotherapeutic targeted agents. In that respect, also visualization of the targets of these new agents is relevant. These targets include the HER2 and angiogenic factors like VEGF. Molecular imaging allows not only visualization of these targets in preclinical models and cancer patients, but also the quantification of target modulation by specific drugs. Molecular imaging techniques can therefore be used for evaluation of several aspects involved in MDR, including drug efflux pumps.

In chapters 3 and 4 the development of new radiopharmaceuticals is described, including the preclinical validation by performing PET imaging with these tracers in human tumor bearing mice.

Chapter 3 describes the development and preclinical validation of PET imaging with the ^{89}Zr-labeled HER3 antibody GE-huMAb-HER3. The HER transmembrane receptor tyrosine kinase family consists of four members: epidermal growth factor receptor (EGFR), HER2, HER3 and HER4. Members of this family play a critical role in tumor cell survival, proliferation, maturation, metastasis and angiogenesis via diverse cellular pathways. HER3 plays a prominent role in tumor growth and maintenance and the fact that it is overexpressed in many solid tumors makes it is an interesting target to inhibit HER family signaling. One example of such a drug is the humanized glycoengineered IgG1 class monoclonal antibody with high affinity for HER3, GE-huMAb-HER3. In order to visualize *in vivo* HER3 expression and study the biodistribution of this antibody we performed the *in vivo* evaluation of ^{89}Zr-GE-huMAb-HER3 in human tumor bearing mice. The human head and neck squamous cell carcinoma (HNSCC) FaDu cell line and human non-small cell lung cancer (NSCLC) cell line H441 are high expressing HER3, QG-56, a human NSCLC cell line with medium and

8

Calu-1 human NSCLC cell line without HER3 expression were used. Dose-dependency of organ distribution and specific tumor uptake was assessed in human tumor bearing mice. Biodistribution analyses showed a dose- and time-dependent ^{89}Zr-GE-huMAb-HER3 tumor uptake in sc FaDu (HER3 positive). The highest tumor uptake of ^{89}Zr-GE-huMAb-HER3 was observed in the 0.05 mg/kg dose group with 27.5 %ID/g at 144 h after tracer injection. MicroPET imaging was performed with ^{89}Zr-GE-huMAb-HER3 in xenografts with varying HER3 expression which revealed specific tumor uptake of ^{89}Zr-GE-huMAb-HER3 in FaDu and H441 models with an increase in tumor uptake over time. Biodistribution data was consistent with the microPET findings. It showed *ex vivo* tumor uptake of ^{89}Zr-GE-huMAb-HER3 of 13.9, 19.0, 9.2 and 7.6 %ID/g in FaDu, H441, QG56 and Calu-1 xenografts respectively. This uptake correlated with HER3 expression levels. ^{89}Zr-GE-huMAb-HER3 specifically accumulated in HER3 overexpressing tumors. It therefore could be concluded that PET imaging with this tracer provides real-time non-invasive information about GE-huMAb-HER3 distribution and tumor accumulation.

Anticalins are a novel class of biopharmaceuticals, which are high affinity scaffold proteins based on human lipocalins. The anticalin PRS-110 targets with high affinity the oncogene c-Met. c-Met is of interest as drug target as genetic and biochemical data showed that the growth and motility factor hepatocyte growth factor (HGF), also called scatter factor and its receptor, the tyrosine kinase c-Met, play a causal role in essential hallmarks of cancer. In chapter 4 we aimed to radiolabel PRS-110 with ^{89}Zr and to visualize c-Met expression and analyze biodistribution of PRS-110 in human tumor bearing mice. PRS-110 was also labeled with the fluorescent dye IRDye 800CW to study the tracer distribution within the tumor. Biodistribution analyses showed a PRS-110 dose-dependent ^{89}Zr-PRS-110 H441 (NSCLC) tumor uptake, with the highest tumor uptake at 10 µg PRS-110 resulting in 7.5 %ID/g at 96 h after tracer injection. MicroPET imaging revealed specific tumor uptake of ^{89}Zr-PRS-110 in the c-Met expressing H441 and U87 (human primary glioblastoma) tumors. Comparison with non-specific anticalin showed non-specific tumor uptake in c-Met non-expressing A2780 human ovarian cancer tumors. Biodistribution data supported the microPET findings, showing *ex vivo* tumor uptake of ^{89}Zr-PRS-110 of 5.9, 1.8 and 1.7 %ID/g in H441, U87 and A2780 xenografts respectively, which correlated with c-Met expression levels. ^{89}Zr-PRS-110 specifically accumulated in c-Met expressing tumors. PET imaging with this tracer provided real-time non-invasive information about PRS-110 distribution and tumor accumulation.

Chapters 5 and 6 describe the application of radiolabeled antibodies to monitor tumor status during treatment effects.

Several targeted therapies are being explored for their potential to inhibit angiogenesis in ovarian cancer. mTOR controls the translation of several oncogenic proteins, including several factors involved in angiogenesis. Inhibiting mTOR results in repression of translation of VEGF-A. Monitoring reductions in tumor VEGF-A expression, as an early read-out for antitumor efficacy, could potentially provide an early response prediction which might benefit patient selection. In chapter 5 we monitored tumor VEGF-A levels with

PET imaging before and during treatment with the mTOR inhibitor everolimus in a human ovarian cancer xenograft mouse model. Tumor VEGF-A levels were measured before and after 2 weeks of continuous everolimus treatment using ^{89}Zr-bevacizumab. Everolimus lowered ^{89}Zr-bevacizumab tumor uptake by 21.7 ± 4.0% (SUV$_{mean}$ 2.3 ± 0.2 versus 2.9 ± 0.2). *In vivo* imaging results were correlated with *ex vivo* biodistribution data and tumor VEGF-A protein levels. *Ex vivo* biodistribution also demonstrated lower tracer uptake in the tumors of treated compared to control animals (7.8 ± 0.8 %ID/g versus 14.0 ± 1.7 %ID/g), while no differences were observed for other tissues. This coincided with lower VEGF-A protein levels in tumor lysates in treated versus untreated tumors and reduced mean vascular density. It was concluded that tumor VEGF-A levels are decreased by everolimus and ^{89}Zr-bevacizumab PET could be used to monitor tumor VEGF-A levels as an early biomarker of the antiangiogenic effect of mTOR inhibitor therapy.

Another drug which effect could be evaluated by molecular imaging is Hsp90 inhibition. The Hsp90 inhibitor NVP-AUY922 downregulates the expression of many oncogenic proteins including IGF-1R and hypoxia inducible factor 1α (HIF-1α) resulting in decreased VEGF-A excretion. Triple negative breast cancer is biologically characterized by heterogeneous presence of molecular pathways. We therefore visualized and monitored in chapter 6 two early Hsp90 inhibition effects in triple negative breast cancer that can be influenced by Hsp90 inhibition with NVP-AUY922 *in vitro* and *in vivo*, namely IGF-1R expression and VEGF-A levels. ^{89}Zr was used as PET radionuclide to label antibodies targeting IGF-1R and VEGF-A. In MCF-7 and MDA-MB-231 human breast cancer cell lines NVP-AUY922 treatment reduced IGF-1R expression and VEGF-A excretion by both cell lines. Human triple negative breast cancer xenograft bearing mice received NVP-AUY922 for 21 days. PET scans with ^{89}Zr-MAB391 and ^{89}Zr-bevacizumab for visualization of IGF-1R and VEGF-A were performed before and after treatment. Hsp90 inhibition lowered tumor uptake on ^{89}Zr-MAB391-PET by 37.3% and on ^{89}Zr-bevacizumab-PET by 44.4%. This was confirmed by *ex vivo* biodistribution with a reduction of 41.3 %ID/g for ^{89}Zr-MAB391 and 37.8 %ID/g for ^{89}Zr-bevacizumab, while no differences were observed for other tissues. This coincided with reduced IGF-1R expression and mean vessel density in the NVP-AUY922 treated tumors. ^{89}Zr-MAB391 and ^{89}Zr-bevacizumab PET reflect effect of Hsp90 inhibitors and can therefore potentially be used to monitor therapeutic effects of Hsp90 inhibitor therapy in triple negative breast cancer.

Fluorescence imaging is currently attracting much interest as a method for intraoperative tumor detection. This technique can potentially be further improved with tracers developed to specifically target tumor-specific characteristics. In chapter 7 we applied antibody-based tumor detection to intraoperative optical imaging, using preclinical *in vivo* mouse models. Bevacizumab and trastuzumab were labeled with the near-infrared fluorescence dye IRDye 800CW. Tumor uptake of the fluorescent tracers and their ^{89}Zr-labeled radioactive counterparts for PET was determined in human xenograft–bearing athymic mice during 1 week following tracer injection, followed by *ex vivo* biodistribution and pathologic examination. Tumor-to-background ratios, with fluorescent imaging, were 1.93 ± 0.40 for bevacizumab and 2.92 ± 0.29 for trastuzumab on day 6 after tracer injection. Intraoperative imaging of fluorescent VEGF- or HER2-positive tumor lesions

8

was also performed in subcutaneous tumors and in intraperitoneal dissemination tumor models. Real-time intraoperative imaging even detected tumor lesions at the sub-millimeter level in the intraperitoneal disseminated tumor models. These results were supported by standard histology, immunohistochemistry and fluorescence microscopy analyses. Near-infrared fluorescent labeled antibodies, targeting VEGF or HER2, can be used for highly specific and sensitive detection of tumor lesions *in vivo*. These preclinical findings encourage future clinical studies with near-infrared fluorescent labeled tumor-specific antibodies for intraoperative guided surgery in cancer patients.

In conclusion, this thesis describes the development and application of newly developed radiopharmaceuticals for PET imaging and the application of radiolabeled antibodies to monitor tumor status during treatment effects. Furthermore, fluorescent labeled antibodies have been developed and can be used for local detection of tumor lesions.

GENERAL DISCUSSION AND FUTURE PERSPECTIVES (4)

Molecular imaging is the *in vivo* characterization and measurement of biological processes at the cellular and molecular level. (5) Most experience in translating this approach into clinical oncology has taken place with PET and SPECT. (6) Initially, the focus in radionuclide imaging was on the visualization of general tumor processes such as glucose consumption with ^{18}F-fluordeoxyglucose (FDG-PET) and DNA proliferation with ^{18}F-3'-fluoro-3'-deoxy-L-thymidine (FLT-PET). However, the availability of novel targeted tracers and new detection systems for clinical use have expanded the potential of molecular imaging even into the intraoperative setting. After labeling the antibodies with ^{89}Zr for PET imaging or IRDye 800CW for optical imaging, a wide variety of tumor characteristics can be visualized.

Soon much information will become available from recently finalized and ongoing clinical studies with ^{89}Zr-antibody imaging. ImmunoPET may be able to support drug development in early clinical trials. The relationship between target expression as measured with ^{89}Zr-antibody tumor uptake and response to therapy of new antibodies will be determined. Also visualization of organ distribution and target accumulation of ^{89}Zr labeled antibody might be useful to determine the optimal drug dose. (7) Besides drug development, this dose finding might also allow precise dosing per patient. (8)

Using molecular imaging with radiolabeled antibodies permits serial characterization of the tumor as pharmacodynamic biomarker for treatment follow up at the whole body level. It is well known that different tumor lesions have variable expression of targets over time and even heterogeneity exists within one lesion. Furthermore during treatment it may be helpful to evaluate whether the drug is achieving the desired effect on its target. To evaluate this approach breast cancer patients who got the Hsp90 inhibitor NVP-AUY922 got a ^{89}Zr-trastuzumab or ^{89}Zr-bevacizumab PET (depending on HER2 expression) before treatment

as well as early during treatment. (9) By using the obtained PET images as pharmacodynamic biomarker for early prediction of response it becomes potentially possible to timely change the treatment plan and spare patients from side effects. In this thesis we showed two preclinical studies in which radiolabeled antibodies were able to monitor treatment effect of mTOR (chapter 5) and Hsp90 inhibition (chapter 6).

Robust trials need to be performed comparing presence of the target in tumor lesions with immunohistochemical staining of a biopsy and conventional imaging modalities with the molecular whole body tumor profile using ^{89}Zr-immunoPET. If such a profile could be proven relevant for optimizing the right selection, moment and dose for targeted therapy the next challenge would be to make these novel PET-tracers more widely available. The half-life and stability of the ^{89}Zr radiopharmaceutical allows production it at a site significantly distant from that of the tracer administration and scanning.

Antibody-drug conjugates (ADCs) such as trastuzumab-DM1, deliver toxins specifically to the tumor and are a promising new class of targeted therapies. Antibody-drug conjugates are antibodies with highly potent cytotoxic agents attached to it via a linker, which is released after internalization in the target cell. Numerous antibody-drug conjugates are currently in clinical development. To determine the amount of toxin delivered to the tumor, immunoPET might be used to calculate the delivery of the compound to the tumor by labeling the naked antibody with ^{89}Zr.

This thesis forms the basis for clinical imaging trials. The newly developed tracers are ready to be used in the clinical setting. ^{89}Zr-GE-HuMab-HER3 (chapter 3) is currently tested in the clinic in order to determine the *in vivo* biodistribution and organ pharmacokinetics of ^{89}Zr labeled GE-huMAb-HER3 in patients with metastatic and/or locally advanced HER3-expressing tumor of epithelial cell origin. This imaging side study is a part of the phase I clinical study of the drug itself. In this side-study, potentially a correlation between tumor uptake of ^{89}Zr-GE-huMAb-HER3, HER3 status and treatment effect can be made. Information about target saturation is also aimed to obtain, which might help to select the appropriate dosing of the antibody in future clinical trials. Imaging results allow supporting the choice for patient selection in phase II clinical studies. The newly developed tracer based on the c-Met targeting anticalin ^{89}Zr-PRS-110 (chapter 4) is ready for clinical translation after the successful development and preclinical studies. The clinical application of the tracer could potentially support the development of the drug PRS-110.

Combining targeted drugs demands a clear mechanistic rationale to test these combinations in clinical studies. Using molecular imaging, assistance may be obtained in providing rationale for combinations of drugs. An understanding of growth factor receptor dynamics, including mechanisms leading to antibody uptake, recycling and degradation of these receptors, and cross-over between them is necessary. Insight in growth factor receptor dynamics *in vivo* in preclinical models and in patients during various conditions using PET imaging will help to improve the personalized treatment of growth factor associated cancers.

8

Moreover, the knowledge obtained with [89]Zr-labeled antibodies can be translated to optical imaging. Clinical testing with the fluorescent labeled antibodies has started based on a similar procedure as used for the radiolabeled antibodies. In chapter 7 we described the preclinical development and validation of fluorescent labeled antibodies. Bevacizumab-800CW is currently produced under good manufacturing practice (GMP) conditions and tested in a clinical study to determine tracer safety and uptake of bevacizumab-800CW in breast cancer tissue. It is likely that also trastuzumab-800CW will be applied clinically soon. Apart from intraoperative image-guided surgery, fluorescence imaging systems are also being developed for diffuse optical imaging, hand-held photo-acoustic based imaging, fluorescent endoscopy and confocal laser endomicroscopy. After the first clinical experience with bevacizumab-800CW, other imaging modalities and other fluorescence labeled antibodies targeting a wide variety of tumor characteristics will be tested in early clinical studies.

REFERENCES

1. Hanahan D , Weinberg RA. Hallmarks of cancer: the next generation. Cell. 2011;144:646-74.

2. de Bono JS, Ashworth A. Translating cancer research into targeted therapeutics. Nature. 2010;467:543-9.

3. Schilsky RL. Personalized medicine in oncology: the future is now. Nat Rev Drug Discov. 2010;9:363-6.

4. Terwisscha van Scheltinga AG, Lamberts LE, de Jong JR, Brouwers AH, Lub-de Hooge MN, de Vries EG. Molecular imaging of tumors with radioactive labeled antibodies from laboratory to the clinic. Am Assoc Cancer Res Educ Book 2012:227-32.

5. Weissleder R, Mahmood U. Molecular imaging. Radiology. 2001;219:316-33.

6. Pysz MA, Gambhir SS, Willmann JK. Molecular imaging: current status and emerging strategies. Clin Radiol. 2010;65:500-16.

7. de Vries EGE, Oude Munnink TH, van Vugt MATM, Nagengast WB. Toward molecular imaging–driven drug development in oncology. Cancer Discovery. 2011;1:25-8.

8. Oude Munnink TH, Dijkers EC, Netters SJ, Lub-de Hooge MN, Brouwers AH, Haasjes JG, et al. Trastuzumab pharmacokinetics influenced by extent human epidermal growth factor receptor 2-positive tumor load. J Clin Oncol. 2010;28:e355-6.

9. Schroder CP, Pedersen JV, Chua S, et al. Use of biomarkers and imaging to evaluate the treatment effect of AUY922, an HSP90 inhibitor, in patients with HER2+ or ER+ metastatic breast cancer. J Clin Oncol 2011;suppl: abstr e11024.

CHAPTER 9

Nederlandse samenvatting
(Summary in Dutch)

Kankerbehandelingen bestaan naast locale behandeling met chirurgie en radiotherapie, uit medicamenteuze behandeling. Gezamenlijk vormen deze behandelingen de basis van de antikankerbehandeling. Antikankermedicijnen bestaan uit chemotherapeutische en moleculair gerichte medicijnen. Met chemotherapeutische middelen wordt geprobeerd direct of indirect schade aan het DNA toe te brengen wat resulteert in remming van de celdeling en inductie van apoptose. Per tumortype worden verschillende chemotherapeutische middelen gegeven al dan niet in combinatie. Niet altijd wordt antitumor effect met deze medicijnen bereikt en er kan resistentie ontstaan tegen deze middelen. Daarom is er behoefte aan uitbreiding van het medicamenteuze arsenaal.

In de afgelopen decennia heeft onderzoek op het gebied van de tumorbiologie nieuwe moleculaire tumorkenmerken geïdentificeerd. Deze kenmerken omvatten onder andere het behoud van proliferatieve signalering, ontwijken van groeiremmers, induceren van angiogenese en het activeren van invasie en metastasering. Inzicht in deze kenmerken heeft een steeds grotere invloed op de ontwikkeling van nieuwe geneesmiddelen. Moleculair gerichte antikankermedicijnen zijn ontwikkeld die specifiek gericht zijn op doelen op of in de tumorcel, doelen in de extracellulaire matrix of op de bloedvaten in de tumor. Voorbeelden van doelen waartegen medicijnen gericht zijn en welke ook relevant zijn voor dit proefschrift, zijn de receptoren voor groeifactoren 'human epidermal growth factor receptor (HER) family', 'insulin-like growth factor receptor 1' (IGF-1R) en de 'mesenchymal-epithelial transition factor' (c-Met) receptor. Ook het pro-angiogene 'vascular endothelial growth factor' (VEGF), het chaperone eiwit 'heat shock protein-90' (Hsp90) en het intracellulaire doel 'mammalian target of rapamycin' (mTOR) zijn gebruikt als om geneesmiddelen tegen te richten.

De ontdekking van nieuwe moleculaire doelen om antikankertherapie tegen te richten heeft geleid tot vele specifiek tumorgerichte antikankermedicijnen, waaronder de therapeutische monoclonale antilichamen. Moleculaire beeldvorming waarbij gebruik wordt gemaakt van radioactief gelabelde antilichamen als tracer kan de aanwezigheid van het doel waartegen het antilichaam gericht is identificeren. Ook kan het potentieel informatie geven over de tumoropname en verdeling van de antilichamen in het lichaam. Daarnaast kunnen deze radioactief gelabelde antilichamen gebruikt worden om de tumorstatus van een bepaalde eigenschap te monitoren tijdens behandelingen, waarbij receptoren of liganden als biomarker gebruikt worden. Afhankelijk van de eigenschappen van het radioisotoop dat gelabeld is aan het antilichaam, kan de beeldvorming plaatsvinden met 'single photon emission computed tomography' (SPECT) of 'positron emission tomography' (PET).

ImmunoPET is gedefinieerd als het volgen en kwantificeren van radioactief gelabelde antilichamen met PET in levende organismen. Een sinds enige jaren beschikbaar geschikt radio-isotoop voor PET beeldvorming is zirconium-89 (^{89}Zr). ^{89}Zr is gelabeld aan verschillende antilichamen en preklinisch en klinisch getest. Ook kunnen fluorescent gelabelde antilichamen zichtbaar gemaakt worden met optische beeldvorming. Deze benadering heeft als voordeel dat geen radioactiviteit nodig is. Hiermee wordt lokale tumorbeeldvorming

in de toekomst mogelijk, met behulp van de verschillende doelen in de tumor waartegen geneesmiddelen gericht zijn.

Dit proefschrift richt zich op het ontwikkelen en preklinisch toepassen van nieuwe tracers voor moleculaire beeldvorming met ^{89}Zr gelabelde radiofarmaca voor PET beeldvorming en fluorescent gelabelde antilichamen voor optische beeldvorming.

In hoofdstuk 1 wordt een korte inleiding gegeven op dit proefschrift. De resultaten die in dit proefschrift gepresenteerd worden zijn verkregen met behulp van moleculaire beeldvorming.

Hoofdstuk 2 beschrijft een literatuurstudie over verschillende beeldvormingstechnieken die gebruikt kunnen worden om 'multidrug resistance' zichtbaar te maken. 'Multidrug resistance' is de resistentie van tumorcellen tegen verschillende soorten cytostatica, zoals anthracyclines, taxanen en vinca-alkaloiden. Verschillende mechanismen kunnen bijdragen aan deze resistentie, onder andere de expressie van membraaneffluxpompen voor medicijnen. Om de mechanismen van deze pompen beter te begrijpen zijn verschillende tracers ontwikkeld voor SPECT en PET beeldvorming. De mogelijkheid om via beïnvloeding van deze pompen de resistentie te omzeilen in de oncologie bleek beperkt te zijn. Hierdoor werd het duidelijk dat 'multidrug resistance' anders benaderd moest worden. Mogelijk zou dit kunnen door gebruik te maken van moleculair gerichte antikankermedicijnen. Daarom worden ook in dit hoofdstuk de rol van HER2 en VEGF daarin beschreven evenals de beeldvorming van HER2 en VEGF beschreven met radioactief gelabelde antilichamen.

De ontwikkeling en preklinische studies voor PET beeldvorming van het ^{89}Zr gelabelde HER3 antilichaam GE-huMAb-HER3 is beschreven in hoofdstuk 3. HER3 is onderdeel van de 'human epidermal growth factor receptor' familie. Leden van deze familie spelen een belangrijke rol bij tumorcel overleving, proliferatie, metastasering en angiogenese via verschillende cellulaire paden. HER3 komt tot expressie in verschillende tumortypes en is daarom een interessant doel om therapie tegen te richten. Een voorbeeld van een geneesmiddel dat bind aan HER3 is het gehumaniseerde IgG1 monoclonaal antilichaam GE-huMAb-HER3. Om de HER3 expressie in tumoren, de tumoropname en orgaandistributie van het antilichaam te bepalen hebben we ^{89}Zr-GE-huMAb-HER3 getest in meerdere tumormodellen. In muismodellen van hoofd-halskanker en niet-kleincellig longkanker, gaven zowel de PET scans als de orgaananalyse voor ^{89}Zr-GE-huMAb-HER3 een dosis- en tijdsafhankelijke tumoropname. Specifieke HER3 gedreven opname van ^{89}Zr-GE-huMAb-HER3 werd gevonden in tumormodellen met HER3-expressie. Er kon daardoor worden geconcludeerd dat PET beeldvorming met ^{89}Zr-GE-huMAb-HER3 de verdeling van het geneesmiddel in beeld kan brengen en informatie kan geven over de tumoropname van GE-huMAb-HER3. Op basis van deze preklinische resultaten wordt deze tracer binnenkort toegepast in een klinische studie waarbij de distributie en tumoropname van ^{89}Zr gelabeld GE-huMAb-HER3 bepaald wordt in patiënten met HER3-tumorexpressie.

9

Hoofdstuk 4 beschrijft de ontwikkeling en preklinische validatie van het met ^{89}Zr gelabelde c-Met anticalin PRS-110. Anticalins zijn een nieuwe groep van biopharmaceuticals gebaseerd op humane lipocalins. c-Met is interessant om geneesmiddelen tegen te richten omdat deze receptor een belangrijke rol speelt in de moleculaire eigenschappen van kanker. In dit hoofdstuk is de ontwikkeling en preklinische validatie beschreven van ^{89}Zr-PRS-110 om de c-Met expressie te kunnen afbeelden en de orgaandistributie te kunnen bestuderen van PRS-110 in muizen die een humane tumor dragen. De tracer is getest in verschillende tumormodellen met variatie in c-Met expressie. PRS-110 is ook gelabeld met de fluorescente dye IRDye 800CW om de tracerdistributie in de tumor ook onder de microscoop te kunnen bestuderen. Zowel de PET scans als de orgaananalyse voor ^{89}Zr-PRS-110 lieten een dosis- en tijdsafhankelijke tumoropname zien. Specifieke c-Met gedreven opname van ^{89}Zr-PRS-110 werd gevonden in tumormodellen met c-Met expressie. Tevens bleek uit tumorcelexperimenten en fluorescentie microscopie dat het fluorescent gelabelde PRS-110 door de cel geïnternaliseerd wordt.

Moleculaire beeldvorming kan mogelijk gebruikt worden als vroege voorspeller van de antitumoreffecten van andere geneesmiddelen. In hoofdstuk 5 is het effect van een remmer van het eiwit 'mammalian target of rapamycin' (mTOR) op VEGF-A bepaald in ovariumkanker. mTOR controleert de translatie van verschillende oncogenen, inclusief belangrijke factoren die een rol spelen bij de angiogenese. Het remmen van mTOR met everolimus kan er daardoor toe leiden dat tumorcellen minder VEGF-A produceren. Monitoring van de VEGF-A expressie zou daarom een vroege uitleesmogelijkheid kunnen zijn om te bepalen of de mTOR-remmer werkzaam is. VEGF-A spiegels kunnen uitgelezen worden met een PET scan na injectie van het met ^{89}Zr gelabelde antilichaam bevacizumab, dat bindt aan VEGF-A. Muizen met humane ovariumtumoren werden voor en tijdens behandeling met everolimus gescand na injectie van ^{89}Zr-bevacizumab. Behandeling met everolimus deed de ^{89}Zr-bevacizumab opname 21% afnemen. Celexperimenten en analyses op het tumorweefsel ondersteunden deze bevindingen. Deze resultaten tonen aan dat ^{89}Zr-bevacizumab PET een vermindering in tumor VEGF-A spiegels na behandeling met everolimus kan visualiseren en kwantificeren. In klinische studies zal aangetoond moeten worden of ^{89}Zr-bevacizumab PET van waarde is als vroeg predictieve biomarker voor de antitumoreffectiviteit van mTOR-remmers in kankerpatiënten.

Moleculaire beeldvorming kan mogelijk ook gebruikt worden om het effect van Hsp90-remmers te monitoren. Remmers van Hsp90 verlagen de expressie van vele tumoreiwitten, inclusief IGF-1R en 'hypoxia inducible factor 1α' (HIF-1α) wat leid tot een verlaagde VEGF-A productie door tumorcellen. Triple negatieve borsttumoren wordt biologisch gekenmerkt door de heterogene aanwezigheid van moleculaire eigenschappen. Daarvoor hebben wij in hoofdstuk 6 twee vroege Hsp90-inhibitie effecten in triple negatieve borsttumoren afgebeeld voor en tijdens behandeling met de Hsp90-inhibitor NVP-AUY922, namelijk IGF-1R en VEGF-A. ^{89}Zr was hiervoor gelabeld aan de antilichamen die gericht zijn tegen respectievelijk IGF-IR en VEGF-A. Muizen met humane triple negatieve borsttumoren werden voor en tijdens behandeling met de Hsp90-remmer gescand na injectie van ^{89}Zr-MAB391 gericht tegen IGF-1R of ^{89}Zr-bevacizumab gericht tegen VEGF-A. Hsp90-inhibitie verlaagde de tumoropname van ^{89}Zr-MAB391-PET met 37.3% en van ^{89}Zr-

bevacizumab-PET met 44.4%. Celexperimenten en immunohistochemische analyses op het tumorweefsel ondersteunden deze bevindingen. Deze resultaten tonen aan dat [89]Zr-MAB391 en [89]Zr-bevacizumab PET een vermindering in tumor IGF-1R en VEGF-A spiegels na behandeling met Hsp90-remmer kunnen visualiseren en kwantificeren. Mogelijk kan een dergelijke benadering gebruikt worden om therapeutische effecten van Hsp90-inhibitie in triple negatieve borsttumoren te monitoren en om als vroege voorspeller te gebruiken van antitumoreffecten.

De rol die fluorescente beeldvorming kan spelen voor lokale beeldvorming van tumoren, bijvoorbeeld voor intra-operatieve tumor beeldvorming wordt onderzocht. Deze techniek kan waarschijnlijk verbeterd worden door gebruik te maken van tracers gericht tegen specifieke tumoreigenschappen. Hoofdstuk 7 beschrijft de ontwikkeling en toepassing van fluorescent gelabelde antilichamen in muismodellen waarbij gebruik is gemaakt van een intra-operatieve camera. Hiervoor zijn de antilichamen bevacizumab en trastuzumab gelabeld met de nabij-infrarode fluorescente kleurstof IRDye 800CW. Bevacizumab is gericht tegen VEGF-A en trastuzumab tegen HER2. Tumoropname van de nieuw ontwikkelde fluorescente tracers is getest door ze te vergelijken met dezelfde antilichamen maar dan met [89]Zr gelabeld voor PET beeldvorming. De nieuw ontwikkelde fluorescente antilichamen toonden dezelfde specifieke tumoropnames als de radioactief gelabelde antilichamen. In zowel subcutane humane tumormodellen als in de buikholte verspreidde tumorlaesies in muizen zijn deze fluorescent gelabelde antilichamen getest met behulp van de intra-operatieve camera. Hiermee konden tumoren zichtbaar gemaakt worden en zelfs sub-millimeter laesies aangetoond worden. Analyses op het tumorweefsel ondersteunden deze bevindingen. Uit deze studie blijkt dat fluorescent gelabelde antilichamen, gericht tegen VEGF of HER2, gebruikt kunnen worden voor specifieke en sensitieve detectie van tumorlaesies. Mede op basis van deze resultaten wordt deze techniek momenteel bestudeerd in een studie met borstkankerpatiënten.

Samenvattend beschrijft dit proefschrift de preklinische ontwikkeling en toepassing van nieuw ontwikkelde tracers voor PET beeldvorming en het gebruik van deze tracers om de tumor status te monitoren tijdens behandeling met antikankermedicijnen. Daarnaast zijn antilichamen fluorescent gelabeld, deze kunnen gebruikt worden voor locale detectie van tumorlaesies.

9

DANKWOORD

In de periode dat ik aan dit proefschrift heb mogen werken heb ik veel ervaringen opgedaan in de wetenschappelijke wereld en een mooie tijd beleefd. Deze plezierige en uitdagende promotietijd is vooral te danken aan de mensen om mij heen. Graag wil ik iedereen bedanken die een bijdrage heeft geleverd aan de totstandkoming van dit proefschrift. Een aantal van deze personen wil ik hier graag noemen.

De meeste dank gaat uit naar mijn promotores prof. dr. E.G.E. de Vries en prof. dr. J.G.W. Kosterink, en mij copromotores dr. M.N. Lub-de Hooge en dr. C.P. Schröder.

Beste Liesbeth, ik heb met veel plezier de afgelopen jaren in jouw onderzoekslijn gewerkt. De vrijheid, verantwoordelijkheid en uitdagingen die je mij hebt gegeven in het onderzoek waardeer ik enorm. Ik keek altijd met veel plezier uit naar je commentaar op de manuscripten, het heeft al mooie publicaties opgeleverd. Niet alleen het uitvoeren van onderzoek heb ik geleerd, ook de samenwerking met industriële partners, het schrijven van subsidies en veel van wat er daarnaast nog allemaal bij het doen van onderzoek komt kijken heb ik van je mogen leren. Bedankt voor de kansen die je mij hebt gegeven.

Beste Jos, bedankt voor de mogelijkheden die jij hebt geschept voor mij om dit onderzoek te kunnen uitvoeren. De mogelijkheden van de ziekenhuisapotheek om te participeren in translationeel onderzoek zijn uniek. Het feit dat je altijd over oplossingen nadenkt heeft erg geholpen tijdens mijn onderzoeksperiode. Doordat je zowel mijn promotor als opleider bent zullen we de komende jaren nog veel samenwerken. Ik kijk hier erg naar uit en hoop ook dat we beide interesses kunnen combineren in de toekomst.

Beste Marjolijn, we hebben vaak de wekelijkse gang van zaken in het onderzoek besproken. Ik heb veel van je geleerd wat er allemaal bij komt kijken om preklinische studies te doen, maar ook om deze zo op te zetten zodat we daarna 'snel' de tracers konden transleren naar klinische studies. De fluorescent en radioactief gelabelde antilichamen die in dit proefschrift staan beschreven en nu in klinische studies getest worden, zijn daar goede voorbeelden van. Hopelijk volgen er in de toekomst nog veel meer. Je dacht vaak in mogelijkheden, en je laat je niet zomaar uit het veld slaan, dat heeft mij erg geholpen!

Beste Carolien, je bijdrage aan alle stukken in dit proefschrift heeft geleidt tot mooiere manuscripten. Het onderzoek in 'triple negative breast cancer' modellen heeft de nodige moeite gekost, maar heeft toch een mooi resultaat opgeleverd! Je snelle hulp als er weer wat geregeld moest worden en je bijdrages aan de imaging-meeting zijn erg waardevol geweest. Je bijdrage aan het translationele karakter van dit onderzoek is erg groot, de klinische studies die nu lopen met tracers uit dit proefschrift zijn daar mooie voorbeelden van. Hopelijk volgen er nog meer!

Graag wil ik de leden van de leescommissie, prof. dr. O.C. Boerman, prof. dr. P.H. Elsinga en prof. dr. J.A. Gietema , bedanken voor het beoordelen van mijn manuscript.

Mijn dank gaat uit naar alle coauteurs en andere personen die nauwe betrokken zijn bij mijn onderzoek.

Prof. dr. Rudi Dierckx, bedankt dat ik op jouw afdeling een deel van dit onderzoek heb mogen uitvoeren, dit heeft er mede voor gezorgd dat we de resultaten zoals gepresenteerd in dit proefschrift hebben kunnen behalen. Je interesse in mijn onderzoek heb ik erg gewaardeerd.

Graag wil ik mijn voorgangers in het ^{89}Zr-antilichaam onderzoek dr. Wouter Nagengast, dr. Eli Dijkers en dr. Thijs Oude Munnink bedanken voor de mogelijkheden die er mede dankzij jullie nu zijn. Wouter, mede dankzij jou zijn de studies met fluorescent gelabelde antilichamen een succes. Bedankt voor ondersteuning tijdens het begin van mij onderzoeksperiode en de vele interessante discussies die we de afgelopen jaren hebben gehad. Succes met het opzetten van je eigen onderzoekslijn! Thijs, naast dat we kamergenoten waren en veel plezier hadden naast het onderzoek, ben ik je veel dank verschuldigd voor alle ondersteuning bij mijn onderzoek. Je stond vaak klaar om te helpen en oplossingen te bedenken om de dierstudies optimaal te kunnen uitvoeren. Knap dat je nu je eigen dromen werkelijkheid maakt!

Beste dr. Hetty Timmer-Bosscha en dr. Coby Meijer, bedankt voor alle steun tijdens dit promotietraject! Het is erg fijn dat jullie deur altijd open staat om alles te kunnen bespreken. Hetty jouw hulp en aanwezigheid bij alle imagingprojecten is erg waardevol en heeft ook mooie resultaten opgeleverd die ook in dit proefschrift staan.

Dr. Go van Dam, onze samenwerking gaat steeds meer vruchten afwerpen, een mooi voorbeeld is het project met de fluorescent gelabelde antilichamen. Bedankt dat jij en jouw team ervoor hebben kunnen zorgen dat we de preklinische experimenten op elk moment van de week konden uitvoeren.

De ondersteuning tijdens de vele experimenten van onze analisten, Linda Pot en Silke Vedelaar, is essentieel geweest voor de totstandkoming van dit proefschrift. De enorme hoeveelheden cellen die we nodig hadden om alle experimenten weer net voor een vakantie af te kunnen krijgen en de ondersteuning tijdens alle biodistributie experimenten hebben mij heel erg geholpen. Bedankt dat jullie vaak klaar stonden om te helpen en problemen op te lossen.

Dr. Arne van der Bilt, wat een succes is onze samenwerking geworden met onze publicatie in Clinical Cancer Research. Zeker iets om trots op te zijn. Ik heb me erg vermaakt tijdens de periode dat we hiermee zijn bezig geweest. Succes met het afronden van je opleiding!

De imaging meeting is de plek waar elke donderdag alle voortgang wordt besproken van de vele projecten die er lopen. Graag wil ik dr. Esther van Straten, dr. Annelies Jorritsma-Smit, drs. Sietske Gaykema, drs. Eva ter Weele, drs. Frank-Jan Warnders, Marlous Arjaans, drs. Michel van Kruchten, drs. Titia Lamberts, drs. Martine den Hollander, drs. Frederike Bensch, drs. Martin Pool, drs. Arjan Kol, drs. Karin Tamas en drs. Hilde Nienhuis bedanken voor de steun, bijdragen aan het onderzoek, gezelligheid en interessante discussie. Succes met het vervolg van het onderzoek.

Het begeleiden van studenten kost soms wat tijd maar levert vooral een leuke tijd op en is iets waardoor je meer plezier krijgt in het doen van onderzoek. De hulp van jullie heeft een belangrijke bijdrage gehad bij de totstandkoming van dit proefschrift en voor de mogelijkheden tot vervolgonderzoek. Drs. Michiel Bolkestein, drs. Rolf de Boer, drs. Anno Saris, Elisa Salomon en Goutham Mallavarapu wil ik bedanken hiervoor. In het bijzonder wil ik Remy Verheijen bedanken, jij hebt zeker voor het anticalin manuscript veel werk verzet, ons werkbezoek in München zal ik niet snel vergeten, succes met het afronden van je opleiding!

Alle collega's en oud-collega's van het Multidisciplinair Oncologisch Laboratorium wil ik bedanken voor alle discussies, ondersteuning en leuke momenten tijdens mijn promotietijd. Met name wil ik prof. dr. Steven de Jong, prof dr. Frank Kruyt en dr. Marcel van Vugt bedanken voor alle bijdragen hieraan.

De afdeling Medische Oncologie wil ik bedanken voor de input tijdens de discussies over de imagingdata, met name dr. An Reyners, prof. dr. Geke Hospers, dr. Annemiek Walenkamp en drs. Sjoukje Oosting. Ook het secretariaat (Gretha Beuker, Bianca Smit en Anja Bos) bedankt voor de ondersteuning.

Afdeling Klinische Farmacie en Apotheek bedankt voor de ondersteuning bij de productie van de tracers zoals beschreven in dit proefschrift. Dr. Hendrikus Boersma, dr. Derk Allersma, drs. Marina Maurer, dr. Coba van Zanten, Alma Suljić-Arifagić, drs. Marieke Sturkenboom en Renella Herder, bedankt voor jullie bijdragen. Daarbij wil ik ook zeker het secretariaat bedanken voor alle hulp, Annemiek van Dijk, Wianda Goense en Jessica Tuinstra.

De afdeling Nucleaire Geneeskunde en Moleculaire Beeldvorming bedankt dat ik een deel van mijn onderzoek bij jullie op de afdeling heb kunnen uitvoeren. Alle technische en praktische ondersteuning bij de studies heb ik erg gewaardeerd. Jurgen Sijbesma, bedankt voor de ondersteuning en het inplannen van alle microPET studies. Dr. Adrienne Brouwers en dr. Johan de Jong ook bedankt voor jullie bijdragen.

De nog niet genoemde kamergenoten, drs. Frank Roossink, drs. Urszula Domanska, dr. Birgit Weyhenmeyer en drs. Rong Wang bedankt voor de leuke tijd in onze kamer, F1.11 van het triadegebouw. Ik heb me er altijd erg thuis gevoeld.

De feestcommissie van het lab wil ik bedanken voor het jaar waarin wij alle activiteiten hebben georganiseerd, de labdag is was uiteindelijk een enorm succes.

Familie en vrienden, bedankt voor alle steun en begrip tijdens mijn promotietraject. Jan, Tiny, Regina, Wouter en Frank bedankt dat jullie altijd voor mij klaarstaan en bedankt voor de ondersteuning tijdens dit promotietraject. Ties, Marion en Maarten, bedankt dat jullie mij altijd met open armen hebben ontvangen. Ook wil ik alle vrienden, collega's, jagers, wielrenners en schaatsers bedanken voor alle ontspanning tijdens deze onderzoeksperiode.

Lieve Julia, bedankt voor alle steun, ik ben blij dat je naast mij staat tijdens mijn promotie en ik kijk uit naar onze toekomst samen.